Università degli Studi di Firenze
European laboratory for non-linear spectroscopy (LENS)
Corso di Dottorato in Atomic and Molecular Photonics

# An experimental setup for quantum optomechanics

*Candidate*
Paolo Vezio

*Supervisor*
Prof. Francesco Marin

*PhD Coordinator*
Prof. Francesco S. Cataliotti

ciclo XXXIII, 2017-2020

Università degli Studi di Firenze, European laboratory for non-linear spectroscopy (LENS).

Thesis submitted in partial fulfillment of the requirements for the degree of Doctor of Philosophy in Atomic and Molecular Photonics.

*"If you think you understand quantum mechanics, you don't understand quantum mechanics."*

*Richard Feynman*

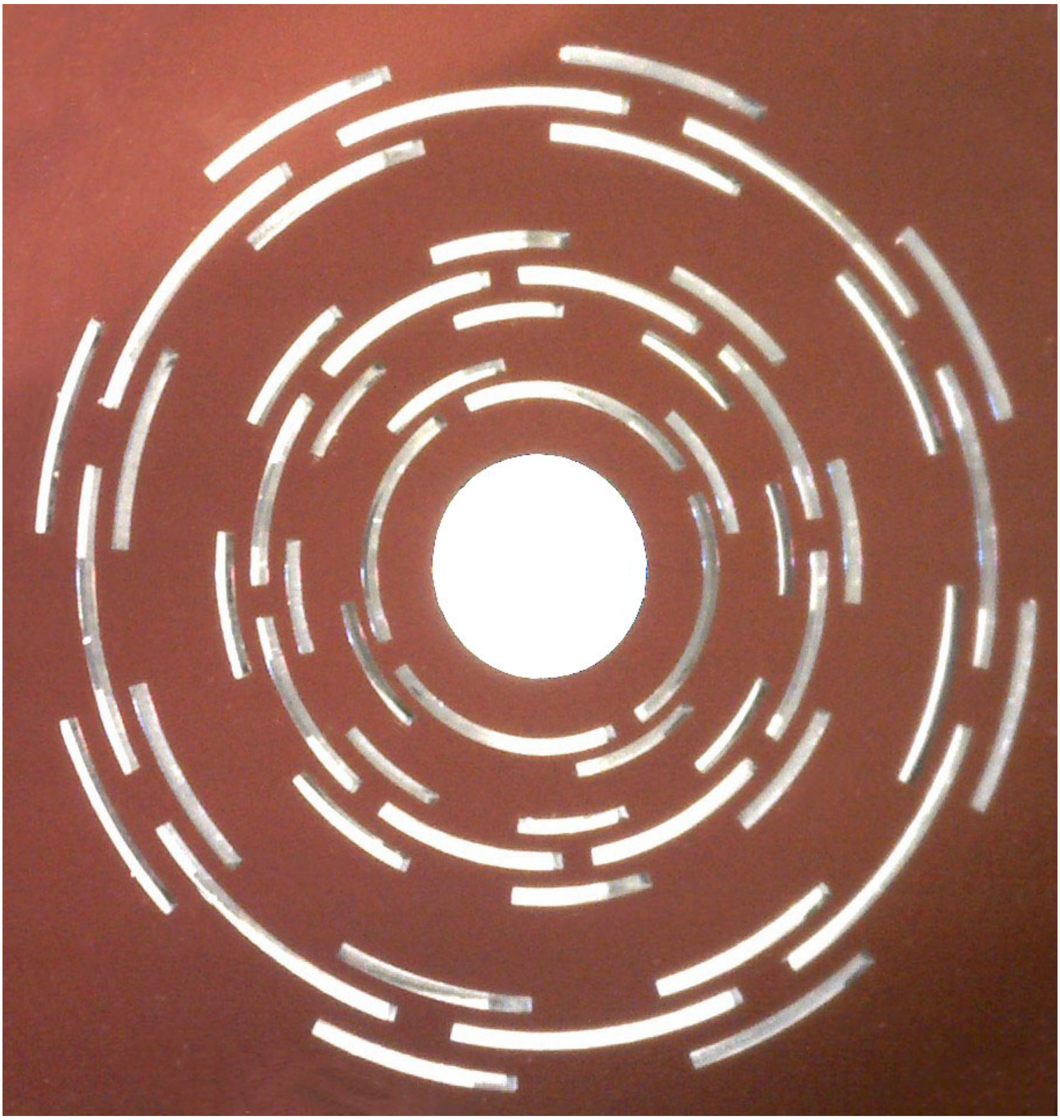

# Abstract

In the last few years cavity optomechanics experiments have achieved the significant progress of the preparation and observation of macroscopic mechanical oscillators in non-classical states. An indicator of the oscillator non-classical proprieties is important also for applications to quantum technologies. In this work, we compare two procedures minimizing the necessity of system calibrations. As first result we compare the homodyne spectra with the measurement of the motional sideband asymmetry in heterodyne spectra. Moreover, we describe and discuss a method to control the probe detuning, that is a crucial parameter for the accuracy of the latter, intrinsically superior procedure. From it we can use the sidebands asymmetry as indicator of the quantumness of the mechanical oscillator, which is originated by the non-commutativity between the oscillator ladder operators. Starting from it the sidebands assume a peculiar shape when a parametric modulation is applied on a oscillator embedded in an optical cavity. A parametric effect is originated by a suitable combination of optical fields. The asymmetry shape is related to the modified system dynamics, while the asymmetric features reveal and quantify the quantum component of the squeezed oscillator motion. The results show that it is possible to use the spectral shape of motional sidebands as a signature of a quantum mechanical squeezed state, without the necessity of absolute calibrations, in particular in the regime where residual fluctuations in the squeezed quadrature are reduced below the zero-point level.

# Contents

# Introduction

The field of optomechanics research studies the interaction of the electromagnetic radiation (photons) with mechanical systems via radiation pressure. The purpose of many optomechanical experiments is to realize a system able to prepare and control a macroscopic oscillator into the quantum state of motion. These massive objects can be used to test fundamental proprieties of the quantum mechanics. That quantum object can be implemented in several applications as well as in quantum sensing and quantum information processing. In the last decade several experiments have been realized to investigate the threshold between classical and quantum visions.

In 1901 a first experiment demonstrated the radiation pressure forces on a mechanical system [51]. Afterwards, in 1909 Einstein studied the statistics of radiation pressure forces onto a movable mirror [27]. In the era of modern physics, in the 1970s, Braginsky studied the mechanical interaction between light and a moving mirror mediated by radiation pressure, particularly for the end-mirror of a cavity. This study was stimulated by the investigation on the fundamental sensitivity limits of the interferometric gravitational wave detectors. Braginsky also showed that radiation pressure can induce damping or anti-damping of the mechanical resonator. He used a microwave cavity to show such effects [14]. During the 1990s further theoretical works increased the interest of the optomechanical field. These works investigate further quantum phenomena, for example: ponderomotive squeezing of light was studied by Fabre *at al.* [29] and Mancini *at al.* [48], the possibility to generate entanglement between mechanical and optical degrees of freedom by Bose *at al.* [12] and Mancini *at al.* [47].

The experimental investigation of these phenomena using macroscopic objects was limited by technological issues. This problem pushed the community to develop optomechanical systems with higher performances that would allow to enter in the quantum regime. This research generated a large variety of systems. Among these, membrane oscillators [76], photonic crystals [26], micropillars [44] and other nano- and micro-systems. In the last few years some quantum phenomena have finally been observed. New devices started the possibility to investigate their non classical proprieties. An example is the asymmetry in the motional sidebands as footprint of the quantum motion of the oscillator [54, 60, 63, 66, 73, 77]. That asymmetry is visible if spurious experimental features are avoided [39, 62, 68]. The explanation of the asymmetry as quantum feature is originated by the noncommutativity between the ladder operators of the mechanical oscillator [8, 41, 80]. The cooling of the mechanical oscillator to its quantum ground state by Teufel *at al.* [75] and Chan *at al.* [19], demonstrated the possibility to prepare a mesoscopic system into a state very close to the quantum state.

The generation of ponderomotive squeezing of light has been demonstrated by Brooks *at al.* [15], Safavi *at al.* [69] and Purdy *at al.* [61]. In these works the squeezing within the interferometric device below the shot noise limit of displacement sensing. The application of these results gives an improvement of gravitational wave detectors [1]. Furthermore, the squeezing of mechanical motion has been demonstrated by Wollman *et al.* [82], Clark *et al.* [22] and Palomaki *et al.* [52].

Recently, the quantum non-demolition (QND) detection of the light intensity is described by Pinard *at al.* [55]. Also the strong cooperativity regime of a microscopic oscillator has been shown by Gröblacher *et al.* in [37]. Feedback control enables the stability of a mechanical system in a desired quantum state. Rossi *et al.* [65] reached the quantum ground state by using a feedback cooling.

All these experiments show the last and remarkable results reached in optomechanics. The purpose of this work is to investigate the quantum proprieties of a macroscopic oscillator, a SiN membrane. In details, the quantumness of the oscillator is identified by observing the asymmetry between the Stokes and anti-Stokes processes. The asymmetry between these two process is peculiar of a quantum system. It allows to study the quantum proprieties of a macroscopic oscillator without necessity of the absolute calibration. To delete all the possible perturbation in the asymmetry measurement, the two sidebands amplitude are corrected by the eventual detuning of the probe beam. Once reached the quantum regime we can drive the mechanical oscillator by parametric modulation, at two times the mechanical frequency ($2\Omega_m$), obtaining simultaneously a compression and amplification of the mechanical motion quadratures.

## Thesis outline

This thesis is structured as follows. In the first Ch. 1 I will give the quantum and classical description of a mechanical oscillator (Sec. 1.1) and the Fabry-Pèrot cavity field (Sec. 1.2). I will also describe the optomechanical coupling between light and mechanical oscillators in the Sec. 1.3. In the same section I obtain the optomechanical equations of motion. I also explain how the difference between the straight motional sidebands induced in the field by the optomechanical interactions, measured in a heterodyne detection, have a particularly behavior in the quantum regime, that it can be used to deduce the oscillator temperature.

In Ch. 2 I will describe the experimental setup in all details. I start with a general description of the apparatus, later I describe in Sec. 2.1 the optomechanical cavity parameters and characteristics. In the same section I describe the theoretical formalism of a circular membrane and the concept of the effective mass. Also, I will describe the cavity finesse concept in a optomechanical cavity. In Sec. 2.2 I will describe the quality factor concept and the procedure to measure it in our optomechanical cavity. In Sec. 2.6 I will describe in general the locking procedure used in our work, as example the Pound-Drever-Hall strategy. Further in Sec. 2.3.1, I will describe the laser source and the possible classical and quantum laser noise. Due to the laser noise we introduce in our setup a filter cavity. The noise structure and the filter cavity implementation is described in Sec. 2.4. In the following section I will describe the detection scheme.

The first experimental Ch. 3 will describe the comparison between the homodyne and heterodyne detection for the measurement of the number occupancy. I will use a method to correct the asymmetry from probe detuning. In this chapter I demonstrate how our optomechanical system is able to confine the oscillator in the quantum regime, with occupation close to 4 phonons.

In the last Ch. 4, I will describe the results obtained by modulating our oscillator at $2\Omega_m$ to generate parametric squeezing on the mechanical motion. The novelty of this work is to observe how the vibrational sidebands are deformed as a consequence of the squeezed and anti-squeezed quadratures.

In details, in the first Sec. 4.1 I will introduce the theoretical concepts. Furthermore I will describe the setup specifications (Sec. 4.2) and in the end, in the last Sec. 4.3, I will describe the most important results obtained in this work.

# Chapter 1

# Cavity Optomechanics

The purpose of this first chapter is to describe the dynamical behavior of a mechanical oscillator coupled by radiation pressure to an optical cavity. I will first introduce in Sec. 1.1 the classical and quantum dynamics of mechanical oscillator and, in Sec. 1.2, of a Fabry-Pérot optical cavity. Then, in the last (Sec. 1.3) will provide a description of the full optomechanical system.

## 1.1 Mechanical Oscillator

### Classical Oscillator

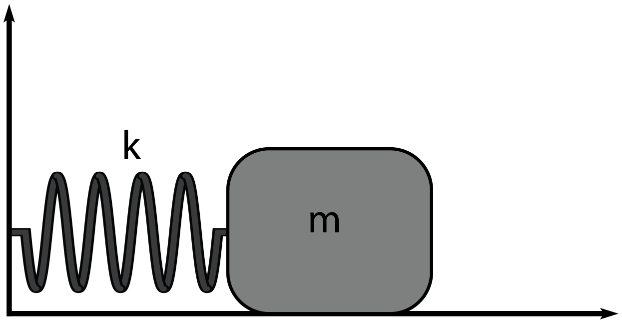

Figure 1.1: Mechanical oscillator described as a block with mass $m$ and spring coefficient $k$.

The dynamics of the membrane can be described, in first approximation, like an ideal harmonic oscillator. Without loss of generality we can schematize the oscillator like a rigid body with a mass $m$ bound to an ideal constrain trough a massless spring of stiffness $k$. The position at a certain time $t$ is described by a variable $x(t)$, satisfying the equation of motion:

$$\ddot{x}(t)m = -kx(t). \tag{1.1}$$

Its general solution is written as $x(t) = x_0 \cos(\Omega_m t + \phi)$ where $\Omega_m = \sqrt{k/m}$ is the oscillation frequency. The arbitrary constants, $x_0$ and $\phi$, are determined by the initial conditions $x(0)$ and $\dot{x}(0)$, and represent respectively the amplitude and phase of the oscillator around its equilibrium position, $x = 0$. The total energy of the system is:

$$E = \frac{p^2}{2\,m} + \frac{k\,x^2}{2}. \tag{1.2}$$

It is positive and vanish for $x = 0$ and $\dot{x} = 0$.

A more realistic model includes the effects of losses and the action of the external forces $F_{ext}(t)$ that drives the system. There exist several dissipation mechanisms: clamping losses, thermoelastic damping, material-induced losses, viscose damping. The first one describes the absorption of the oscillator elastic energy due to clamping [83]. The thermoelastic damping describe the dissipation of elastic energy into heat [84]. It is less relevant at cryogenic temperature. The second last losses are due to to intrinsic defects in the bulk or the surface of the material [45]. The later is due to the collisions between the residual gas particle and the oscillator and it depends strongly on the geometry and shape of the specific normal mode [21]. All these dissipation mechanisms add a contribution at the total quality factor:

$$Q_{tot} = \left( \sum_i \frac{1}{Q_i} \right)^{-1} \tag{1.3}$$

where $i$ is an index identifying the individual loss mechanisms. The oscillator mass is replaced by the effective mass. It depends on the considered mode and how the displacement is measured, as we will see in Sec. 2.1.1. Without loss of generality we can write the motion equation considering only one modal mode:

$$\ddot{x}(t) + \Gamma_m \dot{x}(t) + \Omega_m x(t) = \frac{F_{ext}(t)}{m_{eff}}, \tag{1.4}$$

where $\Gamma_m = \Omega_m/Q$ is the damping rate. Considering the mechanical oscillator in thermal equilibrium with the reservoir at temperature T, due to that the main contribution at external force is described by thermal noise. The thermal force can be described as a Langevin force, $F_{ext}$. It is a stationary Gaussian noise and satisfies following relations as described by the Fluctuation-Dissipation Theorem (FDT) [17,43]:

$$\langle F_{ext}(t)\rangle = 0 \qquad \langle F_{ext}(t)F_{ext}(t')\rangle = 2k_B T m_{eff}\Gamma_m\delta(t-t'). \tag{1.5}$$

Eq. 1.4 can be solved in Fourier space. At this purpose we can define the truncated Fourier transform as

$$x^T(\omega) = \frac{1}{\sqrt{\tau}}\int_{-\tau/2}^{\tau/2} x(t)e^{it\omega}dt \tag{1.6}$$

and obtain the spectral density as $\lim_{\tau\to\infty}\langle|x^T(\omega)|^2\rangle$, where $\langle....\rangle$ indicates the average on different realizations. The Wiener-Khinchin theorem connects $\langle|x^T(\omega)|^2\rangle$ to the Fourier transform of the auto-correlation function, $S_{xx}(\omega)$ called also Power Spectral Density (PSD):

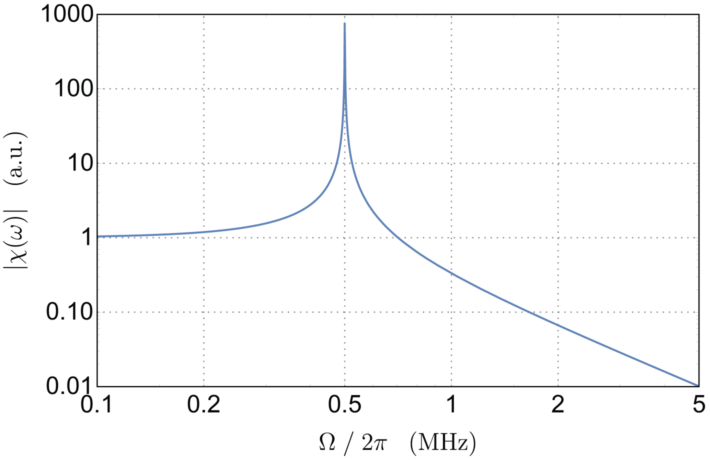

Figure 1.2: Mechanical transfer function, for the mechanical mode at the frequency ~ 500 kHz. The effective mass is of the magnitude of $6.4 \times 10^{-10}$ Kg, with a quality factor close to $10^7$.

$$S_{xx}(\omega) = \int_{-\infty}^{\infty}\langle x(t)x(0)\rangle e^{i\omega t}dt, \tag{1.7}$$

where we assume that $F_{ext}$ is a stationary random process and exploiting the ergodic assumption. Now, we use the standard input-output theory for linear time-invariant systems to evaluate the mechanical susceptibility. Writing Eq. 1.4 in the Fourier space

$$\widetilde{x}(\omega)[(\Omega_m^2-\omega^2)-i\omega\Gamma_m]=\frac{\widetilde{F}_{ext}(\omega)}{m_{eff}}, \tag{1.8}$$

the susceptibility of the damped mechanical oscillator is

$$\chi(\omega)=\frac{\widetilde{x}(\omega)}{\widetilde{F}_{ext}(\omega)}=\frac{1}{m_{eff}((\Omega_m^2-\omega^2)-i\omega\Gamma_m)}. \tag{1.9}$$

That equation gives how the mechanical frequency change under the influence of an external force. The absolute value is:

$$|\chi(\omega)|=\frac{1}{m\sqrt{(\Omega_m^2-\omega^2)^2+(\Gamma\omega)^2}}. \tag{1.10}$$

It describes the actual displacement, its argument specifies the phase lag between the applied force and the oscillator response:

$$arg(\chi(\omega))=arctan\left(\frac{\Omega_m^2-\omega^2}{\Gamma\omega}\right). \tag{1.11}$$

A typical behavior of the transfer function is depicted in the Fig. 1.2. At the resonance the function has a sharp peak, with a half with half maximum (HWHM) is $\Gamma_m$, and at higher frequency the response behavior going as $1/m\omega^2$. The FDT links the dissipation (losses) channel with the generated fluctuation (noise) and applies to any linear system in thermal equilibrium with the bath. The thermal force and position noise are thus related via FDT as:

$$S_{xx}(\omega)=|\chi(\omega)|^2\int_{-\infty}^{\infty}\langle F_{th}(t)F_{th}(0)\rangle e^{i\omega t}dt=|\chi(\omega)|^2S_{ff,th} \tag{1.12}$$

where $S_{ff,th}=2k_BTm_{eff}\Gamma_m$ coming from Eq. 1.5. From Eq. 1.12 it is possible to identify the area under the spectral peak at $\Omega_m$. It gives the variance of the displacement noise:

$$\langle x^2\rangle=\frac{1}{2\pi}\int_{-\infty}^{\infty}S_{xx}(\omega)d\omega. \tag{1.13}$$

Considering a system at low losses, the equipartition theorem gives the displacement variance as $\langle x^2\rangle=k_BT/m_{eff}\Omega_m^2$.

## Quantum oscillator

In the quantum regime the position $x$ and the momentum $p$, are replaced with the observable $\hat{X}$ and $\hat{P}$, where their commutation relation is $[\hat{X},\hat{P}] = i\hbar$. The Hamiltonian is obtained from the total energy substituting the classical momentum and position variable with the corresponding operators.

$$\hat{H}_m = \frac{\hat{P}^2}{2\,m} + \frac{m\Omega_m \hat{X}^2}{2}. \tag{1.14}$$

It is convenient to introduce the dimensionless operators $\hat{x}$ and $\hat{p}$, obtained with the normalizations

$$\hat{x} = \sqrt{\frac{\hbar}{m\Omega_m}}\hat{X}, \qquad \hat{p} = \sqrt{\frac{1}{\hbar m\Omega_m}}\hat{P}, \tag{1.15}$$

satisfying the relation $[\hat{x},\hat{p}] = i$. Now, it is useful introduce two dimensionless operators $\hat{b}$ and $\hat{b}^\dagger$

$$\hat{X} = x_{ZPF}\ \ (\hat{b} + \hat{b}^\dagger), \qquad \hat{P} = -ix_{ZPF}m\Omega_m\ \ (\hat{b} - \hat{b}^\dagger). \tag{1.16}$$

where $x_{ZPF} = \sqrt{\hbar/2m\Omega_m}$ denotes the zero-point fluctuation (ZPF) and we have defined the creation $\hat{b}^\dagger$ and annihilation $\hat{b}$ operators. The commutation relation between the two new operators is $[\hat{b},\hat{b}^\dagger] = 1$. The Hamiltonian of the oscillator can be written as

$$\hat{H}_m = \hbar\Omega_m\left(\hat{b}^\dagger\hat{b} + \frac{1}{2}\right). \tag{1.17}$$

The phonon number operator is $\hat{n} = \hat{b}^\dagger\hat{b}$. From that operator is possible identify its eigenvalue $n$, phonon number, of the eigestate $|n\rangle$:

$$\hat{n}|n\rangle = n|n\rangle \tag{1.18}$$

where $n$ is a natural number. The vacuum state $|0\rangle$ shows the state at zero-phonon, where the energy is $\frac{1}{2}\Omega_m\hbar$. The general Hamiltonian eigenvalues form a discrete ensemble and are given by

$$E_n = \hbar\Omega_m\left(n + \frac{1}{2}\right) \tag{1.19}$$

where $n = 0, 1, 2, 3, \ldots$ . The corresponding eigenstate are:

$$\psi_n(x) = \frac{1}{\sqrt{2^n n!}}\left(\frac{m\Omega_m}{\pi\hbar}\right)^{1/4} e^{-\frac{x^2}{2}} H_n(x) \tag{1.20}$$

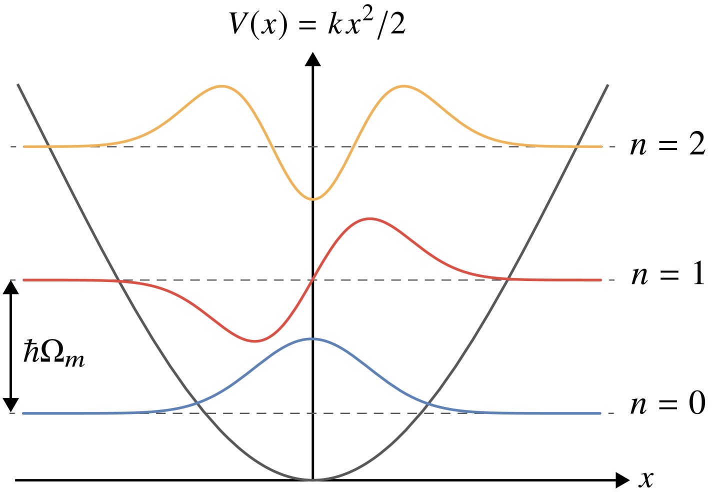

Figure 1.3: First three eigenfunctions for the harmonic oscillator.

where the $H_n(x)$ are the Hermite polynomials. In Fig. 1.3 is shown few different eigenfunctions for the harmonic oscillator. The probability density to find the oscillator between $x$ and $x + dx$ is given by $P_n(x) = |\psi_n(x)|^2$. The mean position $\langle \hat{X} \rangle_n = \int x P_n(x) dx$ and the mean momentum $\langle \hat{P} \rangle_n = -i\hbar \int \psi_n d\psi_n$ vanish, for any given state $n$. The variance of the position $\Delta \hat{X}_n$ and of the momentum $\Delta \hat{P}_n$ operators are

$$\Delta \hat{X}_n = \sqrt{\langle \hat{X}^2 \rangle_n - \langle \hat{X} \rangle_n^2} = x_{ZPF} \sqrt{n + \frac{1}{2}}, \tag{1.21}$$

$$\Delta \hat{P}_n = \sqrt{\langle \hat{P}^2 \rangle_n - \langle \hat{P} \rangle_n^2} = \frac{\hbar}{x_{ZPF}} \sqrt{n + \frac{1}{2}}. \tag{1.22}$$

As a consequence of the commutation relations and the above relations, we obtain the Heisenberg inequality for the two operators

$$\Delta \hat{X}_n \Delta \hat{P}_n \geq \frac{\hbar}{2}. \tag{1.23}$$

The model described until now is a very ideal case. To describe a more realistic model we introduce in the system the mechanical losses. As a first step we remove the hypothesis that consider the system perfectly isolated, and we consider the system coupled with a thermal bath. The total Hamiltonian has three terms: $H_m + H_{env} + H_c$, where $H_m$ is the mechanical Hamiltonian described before, $H_{env}$ describes the external environment energy and the last therm $H_c$ describes the coupling between the two systems. More in detail

$$H_{env} = \sum_i \hbar\Omega_i \left( \hat{d}_i^\dagger \hat{d}_i + \frac{1}{2} \right) \tag{1.24}$$

and

$$H_c = \sum_i \hbar k_i \hat{d}_i \hat{b}^\dagger + h.c.. \tag{1.25}$$

This means that a state of the harmonic oscillator is not an eigenstate of the global system. Furthermore, there are never enough informations on the environment to allow an analytical description of the system and its dynamics. The only possible approach is statistical. We consider the system in the thermal equilibrium. In the statistical ensemble the global state is characterized by the density operator

$$\hat{\rho} = \frac{1}{Z} e^{-\hat{H}_m / k_B T} \tag{1.26}$$

where $Z$ is the partition function

$$Z = \sum_{n=0}^{\infty} e^{-(n+1/2)\hbar\Omega_m / k_B T} = \frac{e^{-\hbar\Omega_m / 2k_B T}}{1 - e^{-\hbar\Omega_m / k_B T}}. \tag{1.27}$$

The oscillator mean energy at the temperature T is given by the equation

$$\langle \hat{H}_m \rangle_T = Tr\left( \hat{H}_m \hat{\rho} \right) = \hbar\Omega_m (n_T + 1/2) \tag{1.28}$$

while $n_T$ is the oscillator mean phonon number

$$n_T = \frac{1}{e^{\hbar\Omega_m / k_B T} - 1}. \tag{1.29}$$

This result gives the phonon occupation for a quantum oscillator, and it is different from the classical description where the mean energy, due to the equipartition theorem is $\langle H_m \rangle = k_B T$. The two descriptions converge when $k_B\, T \gg \hbar\, \Omega_m$.

The effect on the oscillator dynamics due to the reservoir, are well described by in the Quantum Lengevin Equations (QLEs) [30]. The QLEs generalize Eqs. 1.4 and 1.5 to the quantum regime. From here, we will discuss some results of the QLE derivation, following the reference [23], without entering in the details of their derivation. The equations have the familiar form of the classical ones, where we consider a viscous damping force, and a stochastic force, proportional to the velocity. The equations are obtained from the reference [34]

$$\dot{\hat{x}} = \Omega_m \hat{p}, \tag{1.30}$$

$$\dot{\hat{p}} = -\Omega_m \hat{x} - \Gamma_m \hat{p} + \hat{F}, \tag{1.31}$$

$$\langle \hat{F}(t) \rangle = 0, \tag{1.32}$$

$$\langle \hat{F}(t)\hat{F}(t') \rangle = \frac{\Gamma_m}{\Omega_m} \int \frac{d\omega}{2\pi} e^{-i\omega(t-t')} \omega \left[ \coth\left(\frac{\hbar\omega}{2k_b T}\right) + 1 \right]. \tag{1.33}$$

In these equations $\Gamma_m$ is the damping rate, and $\hat{F}$ is a Gaussian quantum stochastic process.

The main conceptual difference between classical and quantum mechanics is non-commutation between the position and momentum operators [23]. The Correlation function of the position can be written as

$$R_{xx}(t) = \langle \hat{x}(0)\hat{x}(0) \rangle \cos(\Omega_m t) + \langle \hat{p}(0)\hat{x}(0) \rangle \sin(\Omega_m t). \tag{1.34}$$

In the classical description the operators are replaced with the observable. The momentum and position observable are not correlated, for that the second term vanishes. In quantum mechanics, the second term due to the commutation relation, $\langle \hat{p}(0)\hat{x}(0) \rangle = -i/2$, is not only different from zero but also complex. The correlation is

$$R_{xx}(t) = \frac{1}{2}[n_T e^{i\Omega_m t} + (n_T + 1)e^{-i\Omega_m t}]. \tag{1.35}$$

The spectral density, with the physical units, is

$$S_{xx}(t) = 2\pi x_{ZPF}^2 [n_T \delta(\omega + \Omega_m) + (n_T + 1)\delta(\omega - \Omega_m)]. \tag{1.36}$$

That expression is not symmetric in frequency, while in the classical description the auto-correlation is real and the spectral density is a symmetric function. The physical explanation of the asymmetry is connected to the occupation number. The positive frequencies of the spectrum are related to the ability of the oscillator to absorb phonons from the bath, where at negative frequencies the oscillator emits phonons toward the bath. In the high temperature limit $n_T \approx n_T + 1$ the classical and quantum prediction are coincident.

## 1.2 Fabry-Pérot Cavity

In this section, I will discuss the classical and quantum description of a Fabry-Pérot resonator. The multiple reflection of the light between two mirrors, produces a stationary wave, if the input light has some particular resonance frequencies. The standing wave patterns produced are called modes. Each stationary solution (field mode) has a stationary wave pattern associated. Different resonator types are distinguished by the focal lengths of two mirrors and by the distance between them. Usual optical cavities are designed to have a high quality factor, and thus low losses and long lifetime of the electric field in the cavity (i.e. small cavity linewidth).

### Classical Description of the Optical cavity

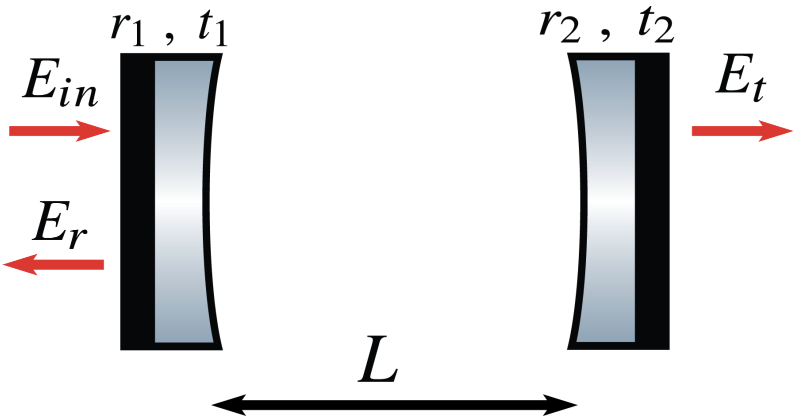

Figure 1.4: Sketch of a Fabry-Pérot cavity with a length $L$. The input and output mirrors have different reflection $r_{1,2}$ and transmission $t_{1,2}$ coefficients.

We will consider a cavity composed by two partially reflective mirrors. The distance between them is $L$. The refraction index inside and outside the cavity is $n = 1$. We define $t_{1,2}$ ($T_{1,2}$) and $r_{1,2}$ ($R_{1,2}$) as the amplitude (power) transmission and reflection coefficient of the mirrors and with $\Sigma_{1,2}$ their losses due to the absorption and diffusion. The conservation of the energy implies that $R_{1,2} + T_{1,2} + \Sigma_{1,2} = 1$. The reflected ($E_r$) and transmitted ($E_t$) fields are [9]:

$$E_r = E_{in}\left[-r_1 + \frac{t_1^2 r_2 e^{i2\phi}}{1-r_1 r_2 e^{i2\phi}}\right], \qquad E_t = E_{in} + \frac{t_1^2 t_2 e^{i\phi}}{1-r_1 r_2 e^{i2\phi}} \tag{1.37}$$

where $E_{in}$ is the amplitude of the input field and $\phi = L\omega/c$ is the phase difference between the wavefront on the mirrors. From Eqs. 1.37 we obtain the transmission $T$ and reflection $R$ cavity coefficients

$$T = \frac{|E_t|^2}{|E_{in}|^2} = \frac{t_1^2 t_2^2}{(1-r_1 r_2)^2}\frac{1}{1+B\sin^2\phi}, \tag{1.38}$$

$$R = \frac{|E_r|^2}{|E_{in}|^2} = \frac{(\zeta/r_2)^2 + B(1-\Sigma_1)sin^2\phi}{1+B\sin^2\phi}, \tag{1.39}$$

where we define $B$ and the coupling coefficient $\zeta$:

$$B = \frac{4r_1 r_2}{(1-r_1 r_2)^2}, \qquad \zeta = r_2\frac{r_1 - r_2(r_1^2+r_2^2)}{1-r_1 r_2}. \tag{1.40}$$

From the Eq. 1.38, we see that resonances are found for $\phi = n\pi$. The linewidth $\kappa_\phi$, is defined by the equation: $4r_1 r_2 \sin^2(\kappa_\phi/2) = (1-r_1 r_2)^2$. The Free Spectral Range ($FSR$) is the distance in frequency between two subsequent resonances, $FSR = c/2Ln$ ($c$ is the velocity of light in vacuum, $n = 1$ in this specific case). We can rewrite the cavity linewidth in the frequency domain as $\kappa_\nu = \kappa/2\pi = \kappa_\phi\frac{FSR}{2\pi}$, and define the cavity finesse is $\mathcal{F} = FSR/\kappa_\nu$. We now pay specific attention to the high finesse cavity. In this case we can assume that $\kappa_\nu \ll FSR$ and the transmission and the losses are much smaller then unity. In this limit, we obtain

$$\mathcal{F} \backsimeq \frac{2\pi}{T_1+T_2+\Sigma_1+\Sigma_2}, \qquad \zeta \backsimeq \frac{T_2-T_1+\Sigma_1+\Sigma_2}{T_2+T_1+\Sigma_1+\Sigma_2} \tag{1.41}$$

and the cavity decay rate becomes $\kappa \backsimeq c(T_1+T_2+\Sigma_1+\Sigma_2)/4L$. The transmission and reflection coefficient can be written as a function of the detuning between the frequency of an input field $\omega_l$ and the cavity resonance $\omega_{cav}$, $\Delta = (\omega_l - \omega_{cav})$. We obtain after some simplification:

$$T \backsimeq \frac{4T_1 T_2}{(T_2+T_1+\Sigma_1+\Sigma_2)^2}\frac{1}{1+4\Delta^2/\kappa^2}, \qquad R \backsimeq \frac{\zeta^2+4\Delta^2/\kappa^2}{1+4\Delta^2/\kappa^2}. \tag{1.42}$$

In the high finesse limit, the field reflection coefficient is

$$H^r(\Delta) = \frac{E_r}{E_{in}} \backsimeq \frac{\zeta - i2\Delta/\kappa}{1-i2\Delta/\kappa}. \tag{1.43}$$

The power in the cavity is described by the equation:

$$P_c = mmP_{in}T_1\left(\frac{\mathcal{F}}{\pi}\right)^2\frac{(\kappa/2)^2}{\Delta^2+(\kappa/2)^2}, \tag{1.44}$$

where we consider a detuned input beam with a power $P_{in}$ and a cavity mode matching $mm$. The transmitted power is $P_{out} = P_cT_2$, where $T_2$ is the transmission coefficient of the cavity output mirror. From the second equation of 1.41, we can identify two regions: from $0 < \zeta \leq 1$ the cavity is undercoupled, for $-1 \leq \zeta < 0$ is overcoupled and for $\zeta = 0$ we have the optimal coupling cavity. The finesse and $FSR$ are related to the concept of the cavity mean photon lifetime. The cavity intensity decrease for each round-trip due to the mirrors transmission and losses:

$$\frac{dI}{dt_{rt}} = -I\frac{T_1+T_2+\Sigma_1+\Sigma_2}{2L/c}. \tag{1.45}$$

In the limit of very short round-trip, the solution of the above equation is $I(t) = I(0)e^{-t/\tau}$. The coefficient $\tau = \frac{1}{2\pi\kappa}$, describes the time at which the intensity decay by a factor of $e$, it can be interpreted as a lifetime of the photon in the cavity. The finesse is proportional to the number of the round-trip before the photon loss.

## Classical dynamical equation

A dynamical equation for the intracavity field can be derived easily, if the input field varies slowly in a scale time of the round-trip, $\tau := 2L/c$, so that $E(t+\tau) \backsimeq E(t)+\tau\dot{E}(t)$. If we consider a high finesse cavity, where the losses are negligible, we can write the intracavity field after a round trip, on the frame rotating at $\omega_l$, as

$$E(t+\tau) = r_1r_2e^{i\omega_l\tau}E(t) + t_1E_{in}(t+\tau). \tag{1.46}$$

Using the above approximation, Eq. 1.46 becomes:

$$\dot{E}(t)\tau = (-r_1r_2 + i\psi)E(t) + t_1E_{in}(t) \tag{1.47}$$

where $\psi$ is the phase detuning from the cavity resonance, given by $\omega_l\tau = n2\pi + \psi$. This parameter can be due either to a mismatch of the cavity length or a mismatch of the light frequency with respect to the resonance condition: $\psi = 2\pi(\frac{\Delta\nu}{FSR} + \frac{\Delta L}{\lambda/2})$. We can rewrite Eq. 1.47 as:

$$\dot{E}(t)\tau = \Big(-\frac{\kappa}{2} + i\Delta\Big)E(t) + \sqrt{\frac{\kappa}{\tau}}E_{in}(t) \tag{1.48}$$

where $\kappa$ is the cavity loss rate. It consists of the sum of three terms $\kappa = \kappa_1 + \kappa_2 + \kappa_\Sigma$, where $\kappa_{1,2} = cT_{1,2}/2L$ are the transmission rates of the mirrors, and $\kappa_\Sigma = c\Sigma/2L$ with $\Sigma = \Sigma_1 + \Sigma_2$ is the total loss rate. The general input field goes through the input mirror. The reflected and transmitted fields are respectively:

$$E^r_{out}(t) = -E_{in}(t) + \sqrt{\kappa_1}E(t), \qquad E^t_{out} = \sqrt{\kappa_2}E(t). \tag{1.49}$$

## Cavity modes

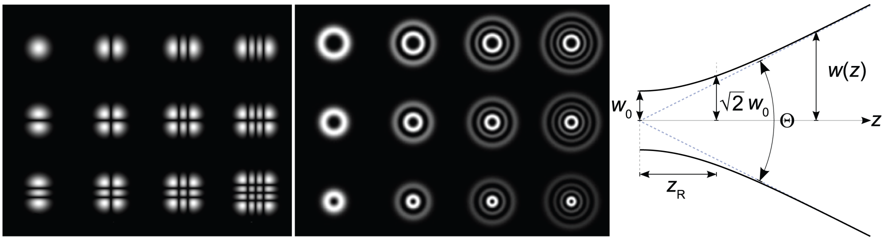

Figure 1.5: In the left part, the Laguerre-Gaussian modes, and in the middle the Hermite-Gaussian modes. On the right, the definition of $R(z)$ and $w(z)$.

Now, we consider the geometrical proprieties of an electromagnetic field inside the cavity, in the paraxial approximation [42,74]. We consider an electric field $E(x, y, z)$ that satisfies the scalar wave equation: $\nabla^2 E + k_0^2 E = 0$, where $z$ is the propagation direction. We write the field as $E = \gamma(x, y, z)e^{-ik_0 z}$, where the complex slowly-varying amplitude $\gamma$ evolves accordingly to

$$\frac{\partial^2\gamma}{\partial x^2} + \frac{\partial^2\gamma}{\partial y^2} - i2k_0\frac{\partial\gamma}{\partial z} = 0 \tag{1.50}$$

where we considered

$$\frac{\partial^2\gamma}{\partial z^2} \ll 2ik_0\frac{\partial\gamma}{\partial z}. \tag{1.51}$$

The solution of 1.50 can be written as

$$\gamma = \psi(x, y) \cdot exp\left[-i\left(p(z) + \frac{k_0}{2q(z)}r^2\right)\right] \tag{1.52}$$

where $r^2 = x^2 + y^2$, $p(z)$ and $q(z)$ are complex functions. $p(z)$ describes the variation of the phase along $z$ and the beam divergence. $q(z)$ parameter describes the variation in beam intensity with the distance $r$ and the curvature of the phase front. We introduce two real parameters $R(z)$ and $w(z)$ related to $q(z)$ by:

$$\frac{1}{q(z)} = \frac{1}{R(z)} - i\frac{\lambda}{\pi w(z)^2}, \tag{1.53}$$

where $R(z)$ is the radius of curvature of the wavefront and $w(z)$ is the decay length of the amplitude with the distance from the axis. $w(z)$ is called beam spot size. These functions are obtained substituting in 1.50 the solution $\gamma$ with constant $\psi(x, y)$

$$w^2(z) = w_0^2\left[1 + \left(\frac{\lambda z}{\pi w_0^2}\right)^2\right], \qquad R(z) = z\left[1 + \left(\frac{\pi w_0^2}{\lambda z}\right)^2\right] \tag{1.54}$$

where $w_0$ is the minimum of $w$ and is called beam waist. From the above solution we obtain $p(z)$ function:

$$ip(z) = \ln\frac{w(z)}{w_0} - i\phi(z) \tag{1.55}$$

where $\phi(z) = arctg\left(\frac{\pi w_0^2}{\lambda z}\right)$ is the phase contribution. The total field is:

$$E = E_0\frac{w_0}{w(z)}e^{-\frac{r^2}{w^2(z)}}e^{-i\left(kz+\frac{r^2 k}{2R(z)}-\phi(z)\right)} \tag{1.56}$$

where $E_0$ is the amplitude of the field, and $k$ is the wave vector. We can consider now the higher order solutions of Eq. 1.50. If we consider the Cartesian symmetries $(x, y, z)$, the solution is:

$$\psi(x, y) = H_m(\sqrt{2}x/w)H_n(\sqrt{2}y/w) \tag{1.57}$$

where $H_m$ is the $m - th$ order Hermite polynomial while $m$ and $n$ are the (transverse) mode numbers. The intensity profiles for this solution are shown in the left panel of the Fig. 1.5. On the other hand in cylindrical coordinates $(r, \phi, z)$ we get

$$\psi(r, \phi) = (\sqrt{2}r/w)^l L_p^l(2(r/w)^2)e^{l\phi} \tag{1.58}$$

where $L_p^l$ is the Laguerre polynomial while $p$ and $l$ are the radial and angular mode number. The modes intensity are shown in the center panel of the Fig. 1.5.

## Quantum description

We start from the quantum Hamiltonian of a single cavity mode (see for example [79]):

$$\hat{H} = \hbar\omega_{cav}\left(\hat{a}^\dagger\hat{a} + \frac{1}{2}\right) \tag{1.59}$$

where $\hat{a}^\dagger$ and $\hat{a}$ are creation and annihilation operators, that satisfy the Boson commutation relation: $[\hat{a}, \hat{a}] = [\hat{a}^\dagger, \hat{a}^\dagger] = 0$ and $[\hat{a}, \hat{a}^\dagger] = 1$. Similarly to the quantum harmonic oscillator is possible to define a photon number occupation $\hat{n}_p = \hat{a}^\dagger\hat{a}$. The mean number of photon in the cavity is given by the average of the photon number operator: $\bar{n}_p = \langle\hat{n}_p\rangle$. The Hamiltonian eigenvalues are

$$E_{n_p} = \hbar\omega_{cav}\left(n_p + \frac{1}{2}\right) \tag{1.60}$$

where $n_p$ is a natural number. The corresponding eigenstates are the Fock state $|\hat{n}_p\rangle$. They form a complete set of orthogonal states

$$\langle n_p|n_p'\rangle = \delta_{n_p,n_p'}, \tag{1.61}$$

$$\sum_{n_p=0}^{\infty} |\hat{n}_p\rangle\langle\hat{n}_p| = 1, \tag{1.62}$$

where $\delta_{n_p,n_p'}$ is the Kronecker delta. The Fock states can be used to construct all the other types of the field state, such as the coherent one.

## Coherent state

The cavity light field used in this work is described by a coherent state. To have a clear description of it, we start from the eigenvalue equation of the annihilation operator

$$\hat{a}|\alpha\rangle = \alpha|\alpha\rangle \tag{1.63}$$

where the eigenvalue $\alpha$ is a complex number and complex eigestate $|\alpha\rangle$. The coherent state eigenstate is a linear combination of Fock states

$$|\alpha\rangle = \sum_{n=0}^{\infty} c_n|n\rangle \tag{1.64}$$

where $c_n$ are complex coefficients. From the expansion 1.64 and considering unit norm $|\langle\alpha|\alpha\rangle|^2 = 1$, we can obtain the representation of a coherent state in the Fock basis

$$|\alpha\rangle = e^{-|\alpha|^2} \sum_{n=0}^{\infty} \frac{\alpha^n}{\sqrt{n!}} |n\rangle. \tag{1.65}$$

The expectation value of the photon number operator, on the coherent state $|\alpha\rangle$, gives the average number of photons

$$\bar{n}_p = \langle\alpha|\hat{n}_p|\alpha\rangle = |\alpha|^2. \tag{1.66}$$

We can observe how the complex amplitude of the field $\alpha$ relates to the mean photon number. The fluctuations of the photon number are calculated following the equation of the standard deviation on $n_p$ ($\Delta n_p = \sqrt{Var(n_p)}$):

$$\Delta n_p = \sqrt{\langle \hat{n}_p^2 - \langle\hat{n}_p\rangle^2\rangle} = \sqrt{\bar{n}_p}. \tag{1.67}$$

The probability to detect $n$ photons in a coherent state $|\alpha\rangle$ is given by the following Possonion distribution equation:

$$P(n) = |\langle n|\alpha\rangle|^2 = e^{-\bar{n}_p} \frac{\bar{n}_p^n}{n!} \tag{1.68}$$

where we used Eqs. 1.65 and 1.66. It governs the quantum fluctuations of the laser light (shot noise). The relative quantum fluctuations are decreasing with $\bar{n}_p$.

$$\frac{\Delta n_p}{\bar{n}_p} = \frac{1}{\sqrt{\bar{n}_p}}. \tag{1.69}$$

The variance of the coherent state become smaller with a higher photon number, i.e. approaching the classical limit.

In the optomechanical experiment, the quantum shot noise has two fold effect of generating noise in the detection and inducing stochastic fluctuations in the oscillator motion through its coupling with the cavity field. For these two reason, it shows the experiment limits in the detection and in the optomechanical cooling. The quantum noise is visible only if the classical noise source are almost canceled, otherwise the classical noise define an upper limit in the apparatus.

## Langevin equations

In this subsection I will describe the quantum dynamical equation for the intracavity field in a Fabry-Pérot cavity. The Hamiltonian 1.59 in the Heisenberg representation gives the equation of motion for a ideal case. To have a realistic description of the system dynamics it is necessary to include in the model fluctuation-dissipation processes, for example quantum fluctuation coupled to the cavity mode through the input mirror $\hat{a}_{in}$ or vacuum input noise describing all other decay channels $\hat{f}_{in}$. In order to find the dynamical equations, where the cavity amplitude decay rate is $\kappa = \kappa_1 + \kappa_i$, which $\kappa_1 = T_1 FSR$ and $\kappa_i = \Sigma FSR$, they are the power transmission coefficient into losses, where $\Sigma = \Sigma_1 + \Sigma_2 + T_2$. We consider that the input field is the coherent state in the frame rotating with the frequency $\omega_l$, $\hat{a}^{old} = e^{i\omega_l t}\hat{a}^{new}$, more details are described in the App. A. The linearized equation ($\hat{a} = \alpha + \delta\hat{a}$) for the intracavity field is [6]

$$\delta\dot{\hat{a}} = -\left(\frac{\kappa}{2} - i\Delta\right)\delta\hat{a} + \sqrt{\kappa_1}\bar{\alpha}_{in} + \sqrt{\kappa_1}\delta\hat{a}_{in} + \sqrt{\kappa_i}\hat{f}_{in} \tag{1.70}$$

where the expectation values are:

$$\langle\delta\hat{a}_{in}(t)\delta\hat{a}_{in}(t')\rangle = \langle\delta\hat{a}^{\dagger}_{in}(t)\delta\hat{a}^{\dagger}_{in}(t')\rangle = \langle\delta\hat{a}^{\dagger}_{in}(t)\delta\hat{a}_{in}(t')\rangle = 0, \tag{1.71}$$

$$\langle\delta\hat{a}_{in}(t)\delta\hat{a}^{\dagger}_{in}(t')\rangle = \delta(t - t'). \tag{1.72}$$

The $\bar{\alpha}_{in} = \sqrt{P_{in}}/\hbar\omega_l$ denotes the mean value of the input field where $P_{in}$ is the injected power. With $\delta\hat{a}_{in}$ we indicate the quantum fluctuations coupled to the cavity mode through the input mirror and $\hat{f}_{in}$ is the vacuum input noise that considers all decay channels. It should be noticed that the intracavity and input fields have different normalization, coefficients: $\langle\hat{a}^{\dagger}_{in}\hat{a}_{in}\rangle = P_{in}/\hbar\omega_l$ and $\langle\hat{a}^{\dagger}\hat{a}\rangle = n_{cav}$, where $n_{cav}$ is number of photons in the cavity. From these results, the intracavity power is given by $P_{cav} = \hbar\omega_l n_{cav}/\tau$. Eq. 1.70 can be written in Fourier space as,

$$\delta\hat{a}(\omega) = \chi_{opt}(\omega)\left[\sqrt{\kappa_1}\bar{\alpha}_{in} + \sqrt{\kappa_1}\delta\hat{a}_{in}(\omega) + \sqrt{\kappa_i}\hat{f}_{in}(\omega)\right] \tag{1.73}$$

where the cavity susceptibility is:

$$\chi_{opt}(\omega) = \frac{1}{\kappa/2 - i(\omega + \Delta)}. \tag{1.74}$$

The square form of this equation will be used to correct any asymmetry due to the cavity filtering in the Ch. 3.

## 1.3 Optomechanical coupling

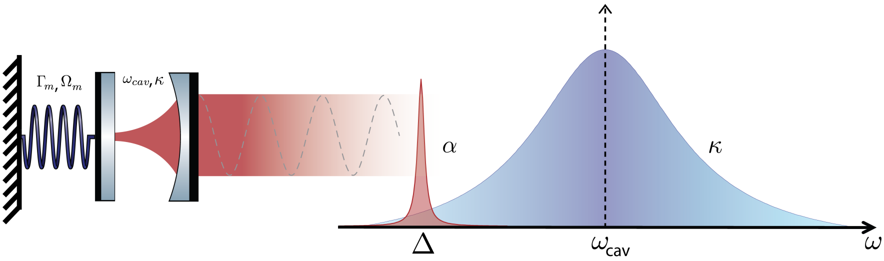

Figure 1.6: Left side: sketch of the optomechanical cavity. Right side: the blue area shows the cavity field and the red one shows the injected field detuned by $\Delta$.

In this new section, I provide a quantum mechanical description of the optomechanical interaction. I consider at this propose a Fabry-Pérot cavity, where one of the two mirrors can oscillate as in Fig. 1.6. Under the action of the radiation pressure force the length of the cavity changes from $L$ to $L + x$. This leads to a different resonance condition of the cavity, and thus to a variation in the intracavity power. The detuning depends on the length variations, $\Delta_c = \Delta_0 + \frac{\omega_l}{L} x$. We assume that the mechanical oscillator motion is slow, compared to the round trip time of the photon in the cavity. Thanks to this approximation, we consider only one optical mode. The Hamiltonian operator is [4–6, 28]:

$$\hat{H} = \hbar\omega_{cav}(x)\left(\hat{a}^\dagger\hat{a} + \frac{1}{2}\right) + \hbar\Omega_m\left(\hat{b}^\dagger\hat{b} + \frac{1}{2}\right). \tag{1.75}$$

Where $\hat{b}$ is phonon annihilation operator and $\hat{b}^\dagger$ is phonon creation operator. Since we assumed a small displacement compared to the cavity length, we expand the cavity resonance frequency:

$$\omega_{cav}(x) \approx \omega_{cav} + \hat{x}\frac{\partial\omega_{cav}(\hat{x})}{\partial x} + \dots \tag{1.76}$$

In the general case, we consider only the linear term. For a cavity as in Fig. 1.6 the derivative of the resonance frequency is $-\omega_{cav}/L$, due to the fact that we are defining $x > 0$ for an increment of the cavity length that leads to a decrease in $\omega_{cav}$. In this approximation the Hamiltonian is rewritten as

$$\hat{H} = \hbar\omega_{cav}\left(\hat{a}^\dagger\hat{a} + \frac{1}{2}\right) + \hbar\Omega_m\left(\hat{b}^\dagger\hat{b} + \frac{1}{2}\right) - \hbar g_0 \hat{a}^\dagger\hat{a}(\hat{b} + \hat{b}^\dagger) \tag{1.77}$$

where $g_0 = Gx_{ZPF}$ is the vacuum optomechanical coupling strength, expressed in frequency. Units $G = \frac{\partial\omega_{cav}(x)}{\partial x}$ is derivative of the resonance frequency, $x_{ZPF} = \sqrt{\frac{\hbar}{2m_{eff}\Omega_m}}$ is the zero-point fluctuation amplitude of the mechanical oscillator, $m_{eff}$ is the effective mass of the modes, and the displacement operator $\hat{x} = x_{ZPF}(\hat{b} + \hat{b}^\dagger)$. In the new Hamiltonian the last term describes the interaction between the optical cavity field and the mechanical oscillator. The radiation pressure force is given by $\hat{F} = -d\hat{H}_{int}/d\hat{x}$, where the interaction Hamiltonian is

$$\hat{H}_{int} = -\hbar g_0 \hat{a}^\dagger\hat{a}(\hat{b} + \hat{b}^\dagger). \tag{1.78}$$

Now, it is convenient to move in a rotating system at the laser frequency $\omega_l$, using the unitary transformation operator $\hat{U} = \exp(i\omega_l\hat{a}^\dagger\hat{a}t)$ (see App. A). The new Hamiltonian is

$$\hat{H} = -\hbar\Delta\hat{a}^\dagger\hat{a} + \hbar\Omega_m\hat{b}^\dagger\hat{b} - \hbar g_0\hat{a}^\dagger\hat{a}(\hat{b} + \hat{b}^\dagger) \tag{1.79}$$

where $\Delta = \omega_l - \omega_{cav}$. In this description we have not yet considered other terms, as the: drive, fluctuation terms, decay factor. As a further step, we introduce the "linearized" description of cavity optomechanics. We split the cavity field into an average coherent amplitude $\langle\hat{a}\rangle = \alpha$ and a fluctuation term: $\hat{a} = \alpha + \delta\hat{a}$. The interaction part of the Hamiltonian is:

$$\hat{H}_{int} = -\hbar g_0(\alpha + \delta\hat{a})^\dagger(\alpha + \delta\hat{a})(\hat{b} + \hat{b}^\dagger). \tag{1.80}$$

It can be split into three terms. The first one is $-\hbar g_0|\alpha|^2(\hat{b}+\hat{b}^\dagger)$ and contains the average of the radiation pressure $\bar{F} = \hbar G|\alpha|^2$. It shifts the origin by $\delta\bar{x} = \bar{F}/m_{eff}\omega_m$. This shift can be accounted for by using a modified detuning $\Delta_{mod} = \Delta + G\bar{x}$. The second term is linear in $|\alpha|$: $-\hbar g_0(\alpha^*\delta\hat{a} + \alpha\delta\hat{a}^\dagger)(\hat{b}+\hat{b}^\dagger)$. The third term $-\hbar g_0\delta\hat{a}^\dagger\delta\hat{a}(\hat{b} + \hat{b}^\dagger)$ is of higher-order in $\delta\hat{a}$. From the mean cavity photons $n_{cav}$, we can define $g = g_0\sqrt{n_{cav}}$ called "the optomechanical coupling strength". The linearized Hamiltonian is:

$$\hat{H}_{lin} = -\hbar\Delta\delta\hat{a}^\dagger\delta\hat{a} + \hbar\Omega_m\hat{b}^\dagger\hat{b} - \hbar g(\delta\hat{a} + \delta\hat{a}^\dagger)(\hat{b} + \hat{b}^\dagger). \tag{1.81}$$

Considering the system in resolved-sidebands regime ($\kappa \ll \Omega_m$), there are three peculiar choices for the detuning of the laser drive with respect to the

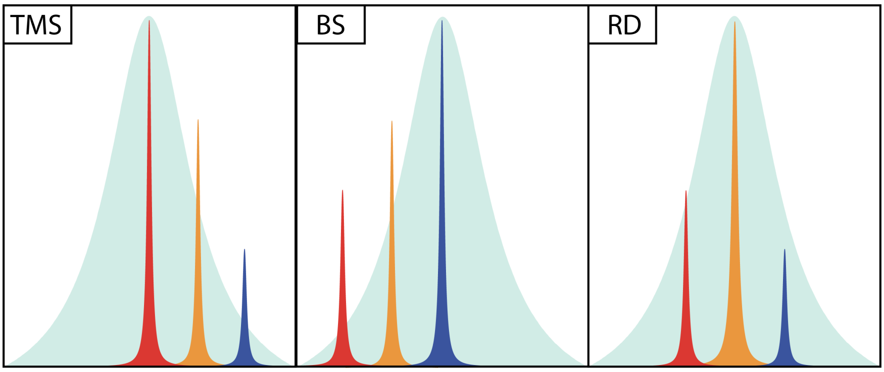

Figure 1.7: Left panel: cavity drive blue detuned at $\Delta = \Omega_m$. Center panel: cavity drive red detuned at $\Delta = -\Omega_m$. Right panel: cavity drive in resonance at $\Delta = 0$. The light green areas show the cavity transfer function, dark yellow peaks show the cavity drive beam, red and blue peaks, respectively Stokes and anti-Stokes sidebands.

cavity resonance, each configuration corresponding to different regime.

$\mathbf{Two-mode\ \ squeezing}$: blue-detuned at $\Delta = \Omega_m$
The first considered case is the blue-detuning by a mechanical frequency $\Delta = \Omega_m$, see left panel in Fig. 1.7. The effective Hamiltonian is reduced from Eq. 1.81 as

$$\hat{H}_{TMS} = -\hbar g(\delta\hat{a}^\dagger\hat{b}^\dagger + \delta\hat{a}\hat{b}). \tag{1.82}$$

This configurations is called two-mode squeezing (TMS). Here the two resonant interactions being the simultaneous creation of a photon and phonon pair. It can create highly correlated and entangled photon-phonon pairs, analog to the down-conversion. In this configuration the phonons creation increase the effective temperature of the oscillator and can yield to instabilities in the system.

$\mathbf{beam-splitter}$: red-detuned at $\Delta = -\Omega_m$
An other possible configuration is at red-detuning by a mechanical frequency $\Delta = -\Omega_m$, see central panel in Fig. 1.7. The effective Hamiltonian in this configuration can be written as

$$\hat{H}_{BS} = -\hbar g(\delta\hat{a}\ \hat{b}^\dagger + \delta\hat{a}^\dagger\ \hat{b}). \tag{1.83}$$

This configuration is called beam-splitter (BS) interaction and can be used to exchange the energy between the optical bath to the mechanics. The two interaction terms are non-resonant. The BS configuration describes the creation of a resonant photon at the cost of a mechanical phonon. In our work a red-detuned drive is used to cool down the mechanical oscillator, in the quantum regime, by sideband cooling [50, 71].

**Resonant Drive**
The last possible configuration is a resonant drive $\Delta = 0$, see right panel in Fig. 1.7. In this configuration both interactions contribute equally as in Eq. 1.81, and the oscillator position ($\hat{b}^\dagger + \hat{b} \propto \hat{x}$) can induce a phase shift on the light field. This phase shift in combination with a phase measurement is used to detect the oscillator position with high sensitivity, as in gravitational wave detectors. Furthermore, this condition can be used to generate ponderomotive squeezing [56] or perform quantum non-demolition measurements (QND).

### 1.3.1 Quantum Langevin Equations

Now we write the optomechanical equation of motion to have a clear description of the system dynamics. The mechanical motion induces a shift in the optical frequency [6]. This changes the light intensity, and the radiation pressure force acting on the motion. The cavity decay rate $\kappa$ introduces a delay between the motion and resulting changes of the force. The analytical treatment of the phenomena is given by the input-output formalism. Equations have the form of quantum linearized Langevin equations, driven by thermal noise, in the frame rotating at the frequency $\omega_l$:

$$\delta\dot{\hat{a}} = \left(i\Delta - \frac{\kappa}{2}\right)\delta\hat{a} + ig_0\alpha\delta\hat{a} + \sqrt{\kappa}\delta\hat{a}_{in}, \tag{1.84}$$

$$\dot{\hat{b}} = \left(-i\Omega_m^0 - \frac{\Gamma_m}{2}\right)\hat{b} + ig_0(\alpha^*\delta\hat{a} + \alpha\delta\hat{a}^\dagger) + \sqrt{\Gamma_m}\hat{b}_{th}, \tag{1.85}$$

where $\Omega_m^0$ is the mechanical resonance frequency, and $\Omega_m$ is the mechanical frequency modified by the optomechanical effects, as I will later describe. The noise correlation associated to the input fluctuations are given by:

$$\langle\hat{a}_{in}(t)\hat{a}_{in}^\dagger(t)\rangle = \delta(t - t'), \tag{1.86}$$

$$\langle \hat{a}_{in}^{\dagger}(t)\hat{a}_{in}(t)\rangle = 0, \tag{1.87}$$

$$\langle \hat{b}_{th}(t)\hat{b}_{th}^{\dagger}(t)\rangle = (\bar{n}_{th}+1)\delta(t-t'), \tag{1.88}$$

$$\langle \hat{b}_{th}^{\dagger}(t)\hat{b}_{th}(t)\rangle = \bar{n}_{th}\delta(t-t'). \tag{1.89}$$

The linearized evolution equations for the intracavity field operator $\delta\hat{a}$ and the mechanical bosonic operator $\hat{b}$ in the Fourier space are

$$\delta\widetilde{a}(\omega)\Bigg( -i\omega - i\Delta + \frac{\kappa}{2}\Bigg) = ig_0\alpha\Bigg(\widetilde{b}(\omega)+\widetilde{b}^{\dagger}(\omega)\Bigg) + \sqrt{\kappa}\,\delta\widetilde{a}_{in}(\omega), \tag{1.90}$$

$$\delta\widetilde{a}^{\dagger}(\omega)\Bigg( -i\omega + i\Delta + \frac{\kappa}{2}\Bigg) = -ig_0\alpha^{*}\Bigg(\widetilde{b}(\omega)+\widetilde{b}^{\dagger}(\omega)\Bigg) + \sqrt{\kappa}\,\delta\widetilde{a}_{in}^{\dagger}(\omega), \tag{1.91}$$

$$\widetilde{b}(\omega)\Bigg( -i\omega + i\Omega_m^0 + \frac{\Gamma_m}{2}\Bigg) = ig_0\Bigg(\alpha\delta\widetilde{a}^{\dagger}(\omega)+\alpha^{*}\delta\widetilde{a}(\omega)\Bigg) + \sqrt{\Gamma_m}\,\widetilde{b}_{th}(\omega), \tag{1.92}$$

$$\widetilde{b}^{\dagger}(\omega)\Bigg( -i\omega - i\Omega_m^0 + \frac{\Gamma_m}{2}\Bigg) = -ig_0\Bigg(\alpha\delta\widetilde{a}^{\dagger}(\omega)+\alpha^{*}\delta\widetilde{a}(\omega)\Bigg) + \sqrt{\Gamma_m}\,\widetilde{b}_{th}^{\dagger}(\omega), \tag{1.93}$$

where the Fourier transform for a generic operator, $\hat{f}(t)$, and the respective hermitian conjugate is defined as

$$\mathcal{F}[\hat{f}(t)] = \int_{-\infty}^{\infty} \hat{f}(t)e^{i\omega t}dt \; = \; \widetilde{f}(\omega) \tag{1.94}$$

and

$$\mathcal{F}[\hat{f}^{\dagger}(t)] = \int_{-\infty}^{\infty} \hat{f}^{\dagger}(t)e^{i\omega t}dt \; = \; \widetilde{f}^{\dagger}(\omega) = \; (\widetilde{f}(-\omega))^{\dagger}. \tag{1.95}$$

In order to have a clear description of the bosonic creation and annihilation operator, Eq. 1.90 and 1.91 are substituted in Eq. 1.92 and 1.93. The result for the annihilation operator is

$$\begin{aligned}&\widetilde{b}(\omega)\Bigg( -i\omega + i\Omega_m^0 + \frac{\Gamma_m}{2}\Bigg) = \\ &= g_0^2|\alpha|^2\Bigg[\frac{1}{-i\omega - i\Delta + \frac{\kappa}{2}} - \frac{1}{-i\omega + i\Delta + \frac{\kappa}{2}}\Bigg]\Bigg(\widetilde{b}(\omega)+\widetilde{b}^{\dagger}(\omega)\Bigg) + \widetilde{b}_{in}(\omega)\end{aligned} \tag{1.96}$$

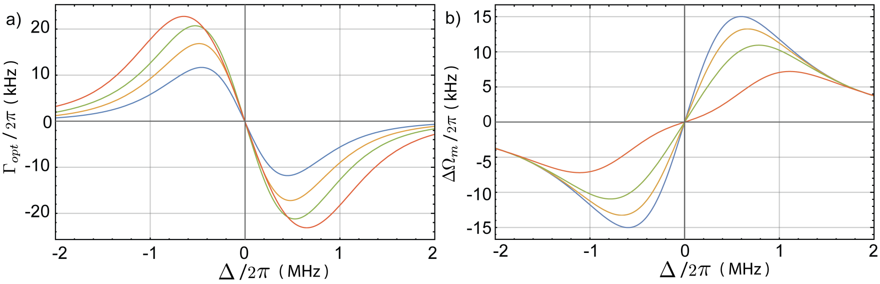

Figure 1.8: a) $\Gamma_{opt}$ trends for different mechanical modes as a function of the detuning $\Delta$. b) frequency shift, $\Delta\Omega_m = \Omega_m - \Omega_m^0$, for different mechanical modes as a function of the detuning $\Delta$. The solid lines show the optomechanical effects for many membrane modes: Blue solid line, mechanical mode $(0,1)$ at 230 kHz. Yellow solid line, mechanical mode $(1,1)$ at 370 kHz. Green solid line, mechanical mode $(0,2)$ at 530 kHz. Red solid line, mechanical mode $(0,3)$ at 830 kHz.

where the last term contains the information of the input contributions, and it is given by:

$$\widetilde{b}_{in}(\omega) = i g_0 \sqrt{\kappa}\left[\frac{\alpha\delta\widetilde{a}_{in}^{\dagger}(\omega)}{-i\omega + i\Delta + \frac{\kappa}{2}} + \frac{\alpha^{*}\delta\widetilde{a}_{in}(\omega)}{-i\omega - i\Delta + \frac{\kappa}{2}}\right] + \sqrt{\Gamma_m}\,\widetilde{b}_{th}. \tag{1.97}$$

From this equation is possible to identify how the optomechanical interaction modify the mechanical resonance frequency and the damping. The interaction adds to the oscillator an additional spring (optical spring), shifting the mechanical frequency resonance as:

$$\Omega_m = \Omega_m^0 + g_0^2|\alpha|^2 \;\; Im\left[\frac{1}{-i\omega - i\Delta + \kappa/2} - \frac{1}{-i\omega + i\Delta + \kappa/2}\right] \tag{1.98}$$

and providing the optical damping

$$\Gamma_{opt} = g_0^2|\alpha|^2 \;\; Re\left[\frac{1}{-i\omega - i\Delta + \kappa/2} - \frac{1}{-i\omega + i\Delta + \kappa/2}\right]. \tag{1.99}$$

We can define effective mechanical damping as $\Gamma_{eff} = \Gamma_{opt} + \Gamma_m$, and the mechanical effective susceptibility

$$\chi_{eff}(\omega) = \frac{\Omega_m^0}{\Omega_m^2 - \omega^2 - i\omega\Gamma_{eff}}. \tag{1.100}$$

The optomechanical modification of the frequency and the damping, as a function of the detuning, are shown in the Figs. 1.8, in the right and left panel, respectively. For a fixed detuning, the ratio between frequency shift and optical damping rate depends on the ratio $\Omega_m/\kappa$: in the resolved side-band regime ($\Omega_m \gg \kappa$) the back-action effect is more evident on the optical damping rate with negligible frequency shift, and vice versa in the bad cavity regime ($\Omega_m \ll \kappa$). The oscillator effective temperature of the overall bath (thermal bath and optical one) is

$$T_{eff} = T\frac{\Gamma_m}{\Gamma_{eff}}. \tag{1.101}$$

From these equations and in close to resonance $\omega \approx \Omega_m$, the Langeven equations of the creation and annihilation mechanical bosonic operator can be written in the following way:

$$\widetilde{b}^\dagger(\omega)\bigg(-i\omega - i\Omega_m + \frac{\Gamma_{eff}}{2}\bigg) = \widetilde{b}^\dagger_{in}(\omega), \tag{1.102}$$

$$\widetilde{b}(\omega)\bigg(-i\omega + i\Omega_m + \frac{\Gamma_{eff}}{2}\bigg) = \widetilde{b}_{in}(\omega). \tag{1.103}$$

In the equation for the bosonic annihilation operator, the contribution of the bosonic creation operator is neglected because it is far from the its resonance, i.e. $\widetilde{b}^\dagger$ is resonant at $-\Omega_m$. This concept is true also for the equation of the creation operator, where the $\widetilde{b}$ is centered in $-\Omega_m$, but resonant at $\Omega_m$, and therefore negligible.

To get a clearer description of the model, we move to a rotating frame around the mechanical frequency $\Omega_m$ (see App. A), the bosonic creation and annihilation operator are given by:

$$\hat{b}_R(t) := \hat{b}(t)e^{i\Omega_m t}, \qquad \hat{b}^\dagger_R(t) := \hat{b}^\dagger(t)e^{-i\Omega_m t}. \tag{1.104}$$

We define a shifted frequency $\omega - \Omega_m = \Omega$. The Fourier Transform of annihilation and creation operator in the rotating frame are thus:

$$\widetilde{b}_R(\omega) = \widetilde{b}(\omega + \Omega_m), \qquad \widetilde{b}^\dagger_R(\omega) = \widetilde{b}^\dagger(\omega - \Omega_m). \tag{1.105}$$

Eq. 1.103 and its Hermitian conjugate can be written in the form of the system of coupled linear equations

$$\begin{pmatrix} -i\Omega + \frac{\Gamma_{eff}}{2} & 0 \\ 0 & -i\Omega + \frac{\Gamma_{eff}}{2} \end{pmatrix} \begin{pmatrix} \widetilde{b}_R \\ \widetilde{b}^\dagger_R \end{pmatrix} = \begin{pmatrix} \widetilde{b}_{in} \\ \widetilde{b}^\dagger_{in} \end{pmatrix} \tag{1.106}$$

The two bosonic operators are:

$$\widetilde{b}_R(\Omega) = \tfrac{1}{-i\Omega+\Gamma_{eff}/2}\left[ig_0\sqrt{\kappa}\left(\tfrac{\delta\widetilde{a}_{in}(\Omega_m)\alpha^*}{-i\Omega_m-i\Delta+\kappa/2}+\tfrac{\delta\widetilde{a}^\dagger_{in}(\Omega_m)\alpha}{-i\Omega_m+i\Delta+\kappa/2}\right)+\sqrt{\Gamma_m}\ \widetilde{b}_{th}(\Omega_m)\right] \tag{1.107}$$

and

$$\widetilde{b}^\dagger_R(\Omega) = \tfrac{1}{-i\Omega+\Gamma_{eff}/2}\left[-ig_0\sqrt{\kappa}\left(\tfrac{\delta\widetilde{a}_{in}(-\Omega_m)\alpha^*}{i\Omega_m+i\Delta+\kappa/2}+\tfrac{\delta\widetilde{a}^\dagger_{in}(-\Omega_m)\alpha}{i\Omega_m-i\Delta+\kappa/2}\right)+\sqrt{\Gamma_m}\ \widetilde{b}^\dagger_{th}(-\Omega_m)\right] \tag{1.108}$$

where the input noise operators are calculated in quasi resonance approximation $\Omega \approx \Omega_m$. The spectrum of the bosonic annihilation operator is:

$$S_{\widetilde{b}_R\widetilde{b}_R} = \frac{1}{2\pi}\left\langle \widetilde{b}^\dagger_R(-\Omega)\widetilde{b}_R(\Omega)\right\rangle. \tag{1.109}$$

The spectrum of the bosonic creation operator is:

$$S_{\widetilde{b}^\dagger_R\widetilde{b}^\dagger_R} = \frac{1}{2\pi}\left\langle \widetilde{b}_R(-\Omega)\widetilde{b}^\dagger_R(\Omega)\right\rangle. \tag{1.110}$$

We use the obtained equations of $\widetilde{b}_R(\Omega)$ and $\widetilde{b}^\dagger_R(\Omega)$ (respectively Eq. 1.107 and 1.108) and the commutation relations written before (Eqs. 1.86 -1.89) to obtain a clear description of the spectra. The contribution of the annihilation operator gives

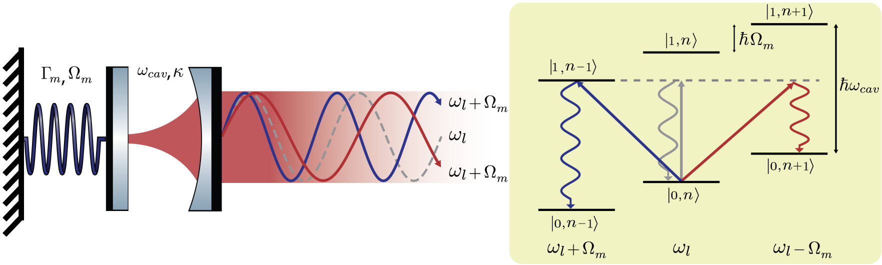

Figure 1.9: Left panel: the optomechanical cavity transmitted beam (resonate with the cavity $\omega_{cav} = \omega_l$) with the two sidebands modulation. Right panel: scattering picture, showing the Stokes ($\omega_l - \Omega_m$) and anti-Stokes ($\omega_l + \Omega_m$) process in the optomechanical cavity.

$$S_{\widetilde{b}_R\widetilde{b}_R}(\Omega) = \frac{\Gamma_m\bar{n}_{th}+\Gamma_{opt}\bar{n}_{BA}}{\Omega^2+\Gamma^2_{eff}/4} = \frac{\Gamma_{eff}}{\Omega^2+\Gamma^2_{eff}/4}\bar{n}, \tag{1.111}$$

while the creation operator spectrum is

$$S_{\tilde{b}_R^\dagger \tilde{b}_R^\dagger}(\Omega) = \frac{\Gamma_m(\bar{n}_{th}+1)+\Gamma_{opt}(\bar{n}_{BA}+1)}{\Omega^2+\Gamma_{eff}^2/4} = \frac{\Gamma_{eff}}{\Omega^2+\Gamma_{eff}^2/4}(\bar{n}+1). \quad (1.112)$$

Where the occupation number due to the back-action is:

$$\bar{n}_{BA} := \frac{\mathcal{A}^+}{\mathcal{A}^- - \mathcal{A}^+}, \quad (1.113)$$

$$1+\bar{n}_{BA} = \frac{\mathcal{A}^-}{\mathcal{A}^- - \mathcal{A}^+}, \quad (1.114)$$

where $\mathcal{A}^+$ is the rate of the upward transition (Stokes process) and $\mathcal{A}^-$ is the rate of the downward transition (anti-Stokes process). They are defined in the follow way:

$$\mathcal{A}^+ := \frac{\kappa\, g_0^2\, |\alpha|^2}{(\Delta-\Omega_m)^2+\kappa^2/4}, \quad (1.115)$$

$$\mathcal{A}^- := \frac{\kappa\, g_0^2\, |\alpha|^2}{(\Delta+\Omega_m)^2+\kappa^2/4}. \quad (1.116)$$

The oscillator effective phonon number is the linear sum of the optical and thermal occupation, it is expressed in the following equation:

$$\bar{n} = \frac{\Gamma_m\, \bar{n}_{th} + \Gamma_{opt}\, \bar{n}_{BA}}{\Gamma_{eff}}. \quad (1.117)$$

In our work we describe an optomechanical system in weakly coupling regime $\Gamma_{eff} \ll \Omega_m$, and them the observable variable exhibit Lorentzian spectra with linewidth $\Gamma_{eff}$. Their variance can be evaluated by integrating over the respective spectral peaks. The spectral variance is define as $\sigma_f = \int_{-\infty}^{\infty} S_{ff}(\Omega)\frac{d\Omega}{2\pi}$. It is used to identify the occupancy of the two sidebands, the anti-Stokes $S_{\tilde{b}_R\tilde{b}_R}(\Omega)$ and the Stokes $S_{\tilde{b}_R^\dagger\tilde{b}_R^\dagger}(\Omega)$:

$$\sigma_{\tilde{b}_R} = \frac{\Gamma_m}{\Gamma_{eff}}\bar{n}_{th} + \frac{\Gamma_{opt}}{\Gamma_{eff}}\bar{n}_{BA} = \bar{n}, \quad (1.118)$$

$$\sigma_{\tilde{b}_R^\dagger} = \frac{\Gamma_m}{\Gamma_{eff}}(\bar{n}_{th}+1) + \frac{\Gamma_{opt}}{\Gamma_{eff}}(\bar{n}_{BA}+1) = \bar{n}+1, \quad (1.119)$$

where it is used:

$$\int_{-\infty}^{\infty} \frac{1}{(\Omega^2+\Gamma_{eff}^2/4)}\frac{d\Omega}{2\pi} = \frac{1}{\Gamma_{eff}}. \quad (1.120)$$

Using these equations we can connect the Stokes and the anti-Stokes areas with the phonon occupancy. We will use this concept to measure the phonon occupation for the mechanical modes by the asymmetry between the two sidebands. In the next chapters I will describe the experimental apparatus, and the experimental results.

# Chapter 2

# Experimental Setup

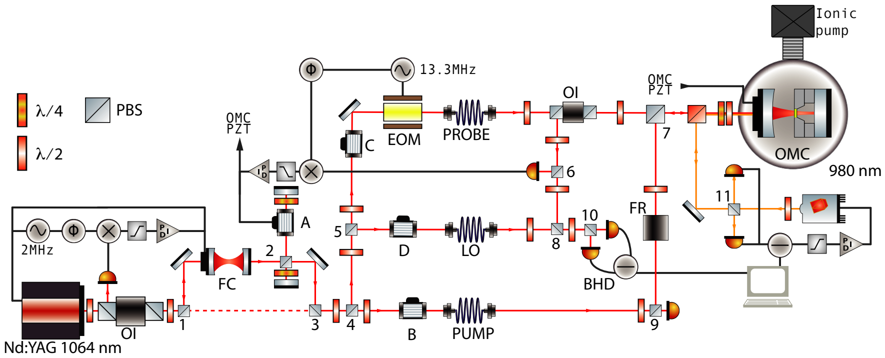

Figure 2.1: General experimental setup.

In this chapter I will describe the apparatus used in the experiment. In Fig. 2.1 I sketch the apparatus used in order to prepare the laser beams and show how they are used in the experiment. The light source is the Mephisto cw Nd:YAG laser operating at $\lambda = 1064$ nm manufactured by InnoLight GmbH (now Coherent Inc. [38]), with a maximum output power of 500 mW.

After a 40 dB optical isolator, we set a polarizing beam splitter (PBS-1) and a half wave plate. With it, we can decide to deviate the beam into a filter cavity or keep it unfiltered. In the first case, the light transmitted from the filter cavity returns into the beam path through a third PBS-3.

Before that the beam is sent through a second PBS-2 in an Acusto-Optic Modulator (AOM), identified with the letter ”A”. The AOM-A is used in the lock scheme of the Optomechanical Cavity (OMC), to correct the fast fluctuations of the cavity error signal. The AOM-A gain is 5.8 MHz/V. The total lock gain is $2 \times 5.8$ MHz/V because the AOM is used in a double pass configuration. More details about the filter cavity will be presented later.

With two PBS, number 4 and 5, and two half wave plates, the beam is divided into three different beams called: Pump, Probe and Local oscillator (LO). The Probe is mainly used to lock the laser frequency to the OMC, and it is also used in the detection as a probe resonant with the cavity. On its path, a resonant electro-optic modulator (EOM) provides phase modulation at 13.3 MHz, with a depth of about 1 rad used for the Pound-Drever-Hall (PDH) detection scheme. The Probe beam radiation is frequency shifted by a AOM-C. The LO is taken from the reflection of the PBS-5 and used as reference in the detection. With an AOM-D, placed on this path, we can control the frequency shift of the LO beam from the cavity resonance, $\Delta_{LO}$. The homodyne detection is performed when the LO beam is resonant, $\Delta_{LO} = 0$. Vice versa heterodyne detection is performed when $\Delta_{LO} \neq 0$. That AOM is used to perform a phase lock in the homodyne and heterodyne at low detection frequency. The Pump beam is used to inject a relatively high power into the OMC. The main purpose of this beam is to cold down the mechanical oscillator. The Pump beam passes trough an AOM-B, it is used to control the frequency shift between the Probe and Pump beam $\Delta_{cool}$, to obtain the best cooling effect on the mechanical oscillator. All the AOMs used in this work are phase locked.

The three beams (Pump, Local oscillator and Probe) are sent to a second optical bench with single-mode, polarization maintaining fibers. The output of the Pump beam fiber is sent on a PBS-9 after a $\lambda/2$, used to select the optical power. The reflected beam is sent to the optomechanical cavity, and the transmitted Pump beam is detected with a photodiode to monitoring the power fluctuation and measure the intensity of the modulation tones on the Pump beam (parametric squeezing scheme). We typically use a fast photodiode with a bandwidth of 200 MHz.

The Probe beam after an optic isolator, is overlapped on a PBS-7 to the Pump beam, with orthogonal polarization. The overlapped beams are mode matched to the OMC. The reflected Probe beam (deviated by the input polarizer on the optical isolator) is detected by the photodiode used to obtain the PDH signal. We will describe it in the Sec. 2.6. The frequency shift generated by the AOMs eliminates any spurious interference and reduces the cross-talk between Pump and Probe. Before the photodiode used for the OMC lock, a half wave plate and a PBS-6 are able to take most of the reflected Probe power and direct it as signal in the heterodyne/homodyne detection. This fraction af the Probe is overlapped with the local oscillator (properly detuned), on the PBS-8. After the PBS-8, the electric fields are rotated by 45° by a half wave plate and then the overlapped beams are divided in two equal component by PBS-10. The two beams are sent on two identical photodiodes to have a Balanced Detection.

Before the OMC, a Dicroic mirror high pass (the wavelength of 1064 nm is transmitted and the laser at 980 nm is reflected) is used to inject in the cavity a second laser with a wavelength close to 980 nm. This beam is used to perform the $Q$-factor measurement. More details about its experimental apparatus are given in Sec. 2.2.

A computer scope is used to acquire the signal from the PDH and the homodyne and heterodyne detection. The signals are digitalised and the scope calculates the signal spectra and takes the average over the several acquisitions. To have a better signal to noise ratio, we acquired different time traces for each apparatus configuration. In the following sections I will describe in details the different components in our apparatus. In the first sub-section the optomechanical system will be described, afterwards I will illustrate the quality factor apparatus and measurement protocol, then I will illustrate the locking scheme and I will describe the reasons why we implemented a filter cavity and its characteristics, in the last section I will describe the homodyne and heterodyne detection scheme.

## 2.1 Optomechanical cavity

The optomechanical cavity is composed by a membrane placed in the middle of a high finesse Fabry-Pérot cavity. The sketch of the optomechanical cavity is shown in the Fig. 2.2. The cavity is composed by two mirrors. The input mirror has a curvature radius $R = 50$ mm, and the output mirror is flat. The input mirror is glued to a high voltage piezoelectric translator PZT through an invar spacer. The invar is a particular metal alloy having a similar low thermal expansion coefficient, $1.7 \times 10^{-6}$ K$^{-1}$, of silica and silicon $\sim 0.57 \times 10^{-6}$ K$^{-1}$. Indeed, by using this metal alloy in the cavity

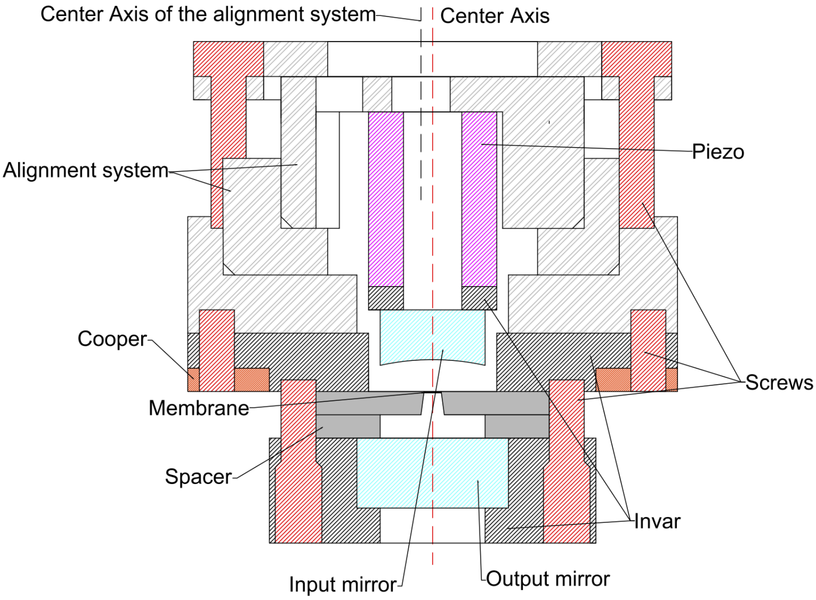

Figure 2.2: Sketch of the optomechanical cavity

components (Fig. 2.2), it is possible to decrease any thermal stress from the mounts on the mirrors and the oscillator. The PZT is used to sweep the cavity length and is used as a slow control in the cavity lock. Between the mirrors, the cavity has a silicon spacer and the silicon plate containing the membrane, both of them $\sim 1$ mm thick. The length of the cavity is 4.377 mm and the free spectral range ($FSR$) is 34.25 GHz. The input mirror transmission is $T_1 = 315$ ppm while the back mirror has high reflectivity, $T_2 = 10$ ppm, both at $\lambda = 1064$ nm. In the beginning of experiment, however, the cavity finesse was 16500 maybe due to a not perfect mirror cleaning. The nominal finesse at zero losses of the empty cavity (without the oscillator), as described in Eq. 1.41 is $\mathcal{F} = 19333$. The cavity finesse with the mechanical oscillator in the middle is a different object, as we will discuss more in details in a following section. In this cavity configuration, the membrane is situated close to the cavity center. The cavity is designed in order to obtain one rigid block, since at cryogenic temperature the cavity does not have the tilt or move. The optomechanical cavity is mounted in a cryostat, evacuated to a pressure below $10^{-5}$ mbar. Via a helium flux we can reach a bath temperature close to 7 K.

The optomechanical cavity has an alignment system. It is composed by two off-axis cylinders, both used to align the cavity with circular movements, given an overall translation of the optical axis. This allows placing the cavity axis in the membrane center. The assembled cavity is fixed on a support and then to a cooled copper plate in the cryostat, thermally connected to the cold finger by means of soft copper foils. The copper plate is mechanically fixed, using thermally isolated legs (fabricated from torlon), to a huge inox mass, connected to the cryostat bottom flange using C-shaped springs. This suspension system reduces the vibrations propagated from the cryostat to the optical cavity. Inside the cryostat, we have three thermal sensors used to monitor the temperature of the cold-finger, the sample and the thermal shield.

During the work of this thesis we changed the cavity PZT from one at high voltage to one at low voltage, with the purpose to decrease the noise introduced by the high voltage amplifier. For this reason in the work described in Ch. 4 the cavity length is different, due to the different PZT length. The length is 3.919 mm and the $FSR$ is 38.25 GHz. All the other cavity parameters are identical to the previous configuration. The low voltage PZT parameters are described in the follow table.

| | |
|---|---|
| model | PI/P-080.341 |
| operating voltage | $-20 \div 100$ V |
| displacement range | $100 \pm 20\%$ nm |
| capacity | 17 $\mu$F |

This second configuration will be used in the parametric squeezing work described in Ch. 4, while the first cavity configuration is used in the calibration work described in Ch. 3.

## Mode matching

When the OMC is put in the cryotat, it is aligned with the optical path. The cavity mode matching identifies the light power in each cavity mode. We align the cavity on the $\mathrm{TEM}_{00}$ mode, for which the mode matching coefficient is described by the follow equation:

$$MM_{0,0} = \sum_{m=0}^{\infty}\sum_{n=0}^{\infty}\frac{V_{0,0}}{V_{m,n}} \tag{2.1}$$

where $V_{m,n}$ are the measured voltage on the PDH detector for each cavity mode $(m, n)$. Experimentally, we just consider the visible modes. For this measurement we tune the cavity length by the PZT glued on the input mirror. The PZT allows to observe a cavity free spectra range, indeed we can measure all the residual cavity modes $(m, n)$. A typically value of $MM_{0,0}$ is $> 95\%$. The mode matching is important for two reasons. Any light not coupled into the fundamental mode of the cavity does not interact with the membrane. The non-resonant modes are reflected back to the PDH detector, causing a decrease in the signal to noise ratio of the locking detector and therefore also effecting the feedback, the stability of the optomechanical system and decreasing the signal in the homodyne and heterodyne detection. All the procedures of mode matching optimization are repeated after the cooling down and before the measurements.

### Cavity length and Free spectral range

The cavities length used in this work is around 4 mm, in both the considered configurations. In order to know the cavity finesse and losses, it is very important to have a good estimation of the cavity length and the free spectral range ($FSR$). Due to the short cavity length, all the possible deformation due to the contraction during the cooling, or the fabrication uncertainty give an important contribution on evaluation of the $FSR$. The $FSR$ is measured using a laser with a tuning range large enough, without mode jumps. That laser setup is shown in the Sec. 2.2. We tune the laser between two different cavity resonances, in each point we measure the laser frequencies, and from the difference we detect the cavity $FSR$. The results of this measure technique, implemented for the two configurations, are shown in the introduction of this section.

## 2.1.1 Circular membrane

In this optomechanical work, we use a circular drum as mechanical oscillator, placed in the center of a Fabry Pérot cavity. We consider a tensioned circular membrane [24]. The vibration modes of the membrane, are given by the solutions of the two-dimensional wave equation, with Dirichlet boundary conditions which represent the constraint of the frame. It can be shows that any arbitrary vibration of the membrane can be decomposes into an infinite series of the membrane's normal modes. We now describe the analytic solution of this problem. We consider an open disk $\Theta$ of radius $a$. Wa call $u(x, y, t)$ the vertical displacement of the membrane, where $(x, y) \in \Theta$. We denote with $\delta\Theta$ the variation of the shape $\Theta$. In cylindrical coordinates $(r, \theta, z)$ the wave equation is:

$$\frac{\partial^2 u}{\partial t^2} = c^2 \left( \frac{\partial^2 u}{\partial r^2} + \frac{1}{r}\frac{\partial u}{\partial r} + \frac{1}{r^2}\frac{\partial^2 u}{\partial \theta^2} \right) \qquad 0 \leq r < a; \qquad 0 \leq \theta \leq 2\pi \tag{2.2}$$

where $u = 0$ for $r = a$. $c$ is a positive constant, giving the speed at which

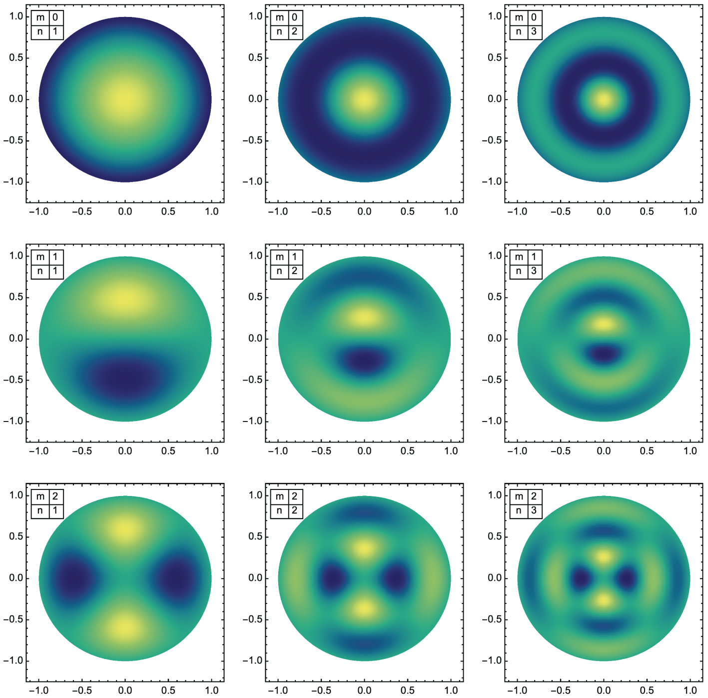

Figure 2.3: Modes of the membrane vibration, labeled with the number $m$ and $n$.

transverse vibration waves propagate in the membrane:

$$c = \sqrt{\frac{N_{rr}}{\rho h}} \tag{2.3}$$

where $N_{rr}$ is the radial membrane stress at the membrane boundary ($r = a$), $h$ is the membrane thickness, and $\rho$ is the density of the membrane. In the general case, we assume a solution in separated variables

$$u(r, \theta, t) = R(r)\Theta(\theta)T(t). \tag{2.4}$$

We replace this into the wave equation, the result is:

$$\frac{T''(t)}{c^2T(t)} = \frac{R''(r)}{R(r)} + \frac{R'(r)}{rR(r)} + \frac{\Theta''(\theta)}{r^2\Theta(\theta)} = K \tag{2.5}$$

where $K$ is a constant. The equation for $T(t)$ has different solutions, for $K > 0$ an exponential grow or decay solution, for $K = 0$ the solutions are linear, and they are periodic for $K < 0$. In order to find the solution of the vibrating membrane we consider $K < 0$, then $K = -\lambda^2$ with $\lambda > 0$. The solution for $T$ is the combination of sine and cosine functions,

$$T(t) = Acos(c\lambda t) + Bsin(c\lambda t). \tag{2.6}$$

From the other equation:

$$\frac{R''(r)}{R(r)} + \frac{R'(r)}{rR(r)} + \frac{\Theta''(\theta)}{r^2\Theta(\theta)} = -\lambda^2. \tag{2.7}$$

Separating the variables and after multiplying both sides by $r^2$:

$$\lambda^2 r^2 + \frac{r^2R''(r)}{R(r)} + \frac{R'(r)r}{R(r)} = L \tag{2.8}$$

and

$$-\frac{\Theta''(\theta)}{\Theta(\theta)} = L \tag{2.9}$$

where $L$ is the same constant. Since $\Theta(\theta)$ is periodic, with period $2\pi$, the solutions is:

$$\Theta(\theta) = Ccos(m\theta) + Dsin(m\theta), \tag{2.10}$$

where $m = 0, 1, ...$ and $C$ and $D$ are constants. This also implies $L = m^2$. The solution for $R(r)$ equation is a linear combination of Bessel functions $J_m$ and $Y_m$.

$$R(r) = c_1J_m(r\lambda) + c_2Y_m(r\lambda). \tag{2.11}$$

The Bessel function $Y_m$ is unbounded for $r \to 0$, resulting in an unphysical solution for the vibrating membrane, so the constant $c_2$ must be null. We assume that $c_1 = 1$. From the boundary condition $u = 0$ with $r = a$, we obtain

$$R(a) = J_m(a\lambda) = 0. \tag{2.12}$$

The Bessel function $J_m$ has an infinite number of positive roots, $0 < \alpha_{m1} < \alpha_{m2} < ...$ . Therefore we get that $\lambda_a = \alpha_{m,n}$, for $n = 1, 2, ...$, so the solution can be written as $J_m(\alpha_{m,n}\frac{r}{a})$. The total solutions for the vibration of the membrane are:

$$u_{mn}(r, \theta, t) = (A\cos(c\lambda t) + B\sin(c\lambda t))J_m\left(\alpha_{m,n}\frac{r}{a}\right)(C\cos(m\theta) + D\sin(m\theta)), \tag{2.13}$$

for $m = 0, 1, ...$ and $n = 1, ...$ .

## Effective Mass

This section has the purpose to describe the concept of mechanical mode effective mass. In the general case, we consider a system with a density $\rho(\vec{x})$. The displacement of the infinitesimal volume $d\vec{x}$ on the position $\vec{x}$ in vibrational mode is:

$$\vec{u}(\vec{x}, t) = \vec{u}(\vec{x})e^{i(\omega t + \phi(\vec{x}))} \tag{2.14}$$

The physical mass of the system is equal to:

$$M = \int_V \rho(\vec{x})d\vec{x} \tag{2.15}$$

where $V$ is the total volume. We can define the measurement of affective position as:

$$D := \int_V g(\vec{u})\vec{u}d\vec{x} \tag{2.16}$$

where $g(\vec{x})$ an arbitrary detection function. The energy of an element, $d\vec{x}$, of the system is equal to:

$$\frac{1}{2}\rho\; d\vec{x}\,\omega^2\; \vec{u}^2(\vec{x}, t) + \frac{1}{2}\dot{\vec{u}}(\vec{x}, t)^2\; \rho d\vec{x} = \rho\; d\vec{x}\omega^2\; \vec{u}(\vec{x})^2 \tag{2.17}$$

where $\dot{\vec{u}} = \omega\vec{u}e^{i\omega t}$ and $\rho d\vec{x}$ is the mass of the volume element of the system. We require that the description of the vibration system as a simple harmonic oscillator with the displacement $\vec{x}$, conserve the total energy. Therefore we can write:

$$\omega^2 \int_V \rho(\vec{x})\vec{u}^2(\vec{x})d\vec{x} = M_{eff} D^2 \omega^2. \tag{2.18}$$

Where $M_{eff}$ is the effective mass. We obtain the effective mass in the general case as:

$$M_{eff} = \frac{\int_V \rho(\vec{x})u^2(\vec{x})d\vec{x}}{\left[\int_V \vec{u}(\vec{x})g(\vec{x})d\vec{x}\right]^2}. \tag{2.19}$$

As it can be seen from this equation, the exact matching between the probing beam and the mechanical mode shape will lead to $D = 1$, yielding the minimum effective mass of the $(m, n)$ mode. Any mode mismatch will lead to $D < 1$ and therefore the respective mode will appear to be heavier ($M_{eff} > M$). In the extreme case of zero overlap $D \to 0$, the respective mode effective mass diverges. This actually means that the optomechanical coupling is weak, as the light is not sensitive to the motion of the oscillator.

In this general description we will restrict to the case of the circular membrane. We consider a scalar displacement in the orthogonal direction to the membrane plane. In this case we describe the position with polar coordinates $(\vec{r}, z, \theta)$. From the previous description of the mechanical modes of the membrane, as see that they are described with Bessel functions. We indicate the modal frequencies as $\nu_{m,n} = \nu_0 \alpha_{m,n}$, where $\nu_0 = \frac{1}{2\pi}\sqrt{\frac{N_{rr}}{\rho}\frac{1}{a}}$. In our case $\rho$ is 3200 kg/m$^3$, $T$ is equal to $\sim$ 0.8 GPa and $a = 0.82$ mm is the radius of the membrane. With these values, we calculate $\nu_0 = 96.6$ kHz. The Bessel polynomials, describe the movements of the membrane from the unperturbed position:

$$u(r, \theta) = J_m\left(\alpha_{m,n}\frac{r}{a}\right)(\cos(m\theta) + \sin(m\theta)). \tag{2.20}$$

The effective mass in cylindrical coordinates is:

$$M_{eff} = \frac{h\rho \iint u^2 d\theta dr}{\left[\iint u \cdot G(r, \theta) d\theta dr\right]^2} \tag{2.21}$$

where $G$ is a Gaussian function normalized to one describing the reading function.

$$G(r, \theta) = \frac{2}{\pi w} e^{-2\frac{|\vec{r}-\vec{\delta}|^2}{w^2}}, \tag{2.22}$$

where we indicate with $w$ the waist of the beam, $\vec{\delta}$ is the distance from the center of the membrane to the center of the beam, $h$ is the constant

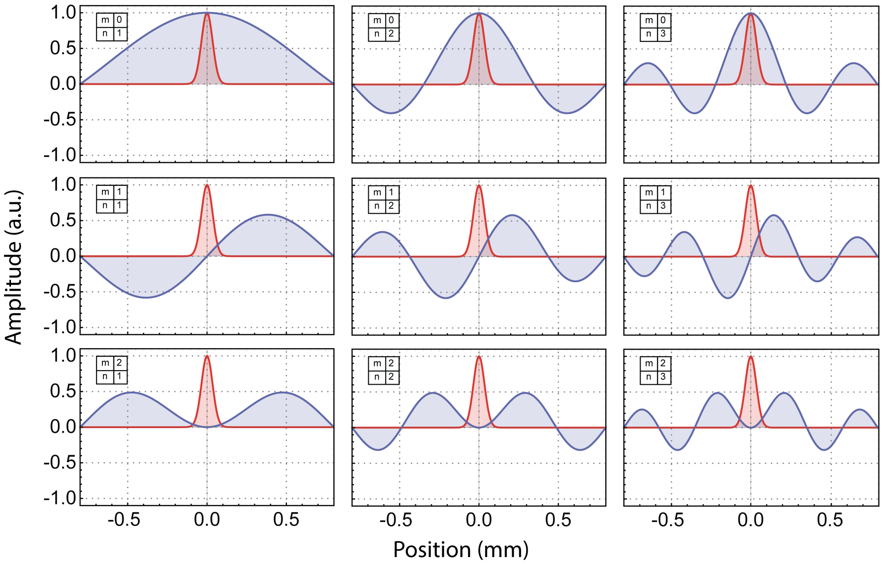

Figure 2.4: Mechanical mode shape functions (blue) and optical read-out (red) to display the concept of overlap functions and effective mass of a mechanical mode. We look at cuts along the y-Axis of the membrane. The waist radius of the TEM$_{00}$ (optical read-out function) is $\sim 70\ \mu$m, centered on the membrane $\vec{\delta} = 0$. In each subplot is shown a different modal mode, labeled by (m,n), for a circular SiN membrane with a diameter of 1.6 mm. All the waves are normalized with respect to their respective maximum.

thickness of the membrane. It is possible to identify the total mass of the system $M = \pi a^2 h\rho$. The ratio between the effective mass and the physical one is:

$$\frac{M_{eff}}{M} = \frac{\frac{1}{\pi a^2}\int_0^{2\pi}\int_0^a r J_m^2(\alpha_{m,n}\frac{r}{a})\cos^2(m\theta)d\theta dr}{\left[\frac{2}{\pi w^2}\int_0^{2\pi}\int_0^a r J_m(\alpha_{m,n}\frac{r}{a})\cos(m\theta)e^{-\frac{2}{w^2}(r^2+\delta^2-2r\delta\cos(\theta))}d\theta dr\right]^2}. \tag{2.23}$$

Now we normalize the $r$, $\Delta$ and $w$ at the radius of the membrane $a$. We can use an integral result of the Bessel function:

$$\int_0^1 x J_m^2(\alpha_{m,n}x)dx = \frac{1}{2}J_{m-1}^2(\alpha_{m,n}) \tag{2.24}$$

where $x = r/a$. From now we consider $r$, $\delta$ and $w$ as normalized to the membrane radius $a$. We now calculate the mass for two different situations, $m = 0$ and $m \neq 0$. In the first case we just have the rotational symmetrical modes. In this case the effective mass for the modes is:

$$\frac{M_{eff}}{M} = \frac{J_1^2(\alpha_{0,n})}{\left[\frac{4}{\pi w^2}\int_0^1 I_0(\frac{4x\delta}{w^2})J_0(\alpha_{0,n}x)e^{-\frac{2(x^2+\delta^2)}{w^2}}xdx\right]^2} \tag{2.25}$$

where $I_0$ is due to the integration over the variable $\theta$. For $m \neq 0$, the numerator of the Eq. 2.23 is $\frac{1}{2}J_{m-1}^2(\alpha_{m,n})$. In the denominator the integration on the variable $\theta$ is not obvious. At the purpose of simplify the solution, we introduce the approximation, $\frac{\delta}{m} \gg w$. It means that the mode shape varies slowly over the beam waist. In this case we can move out of the integral the cos function:

| $(m,n)$ | $\delta$ | $M_{eff}/M$ | $g_0$ (Hz) |
|---|---|---|---|
| $(0,1)$ | 0.34 | 0.39 | 34 |
| $(0,2)$ | 0.34 | 1.4 | 11 |
| $(1,1)$ | 0.34 | 0.60 | 20 |
| $(0,1)$ | 0.1 | 0.28 | 37 |
| $(0,2)$ | 0.1 | 0.14 | 35 |
| $(1,1)$ | 0.1 | 3.95 | 7 |

Table 2.1: In this table are shown the theoretical values of the effective mass normalized at the physical mass of the mechanical oscillator and the relative vacuum optomechanical coupling $g_0$ for three mechanical modes taken in consideration in this work. The two parameters are calculated for the two configuration of the cavity spot, $\delta = 0.34$ and $\delta = 0.1$.

$$\frac{M_{eff}}{M} \simeq \frac{\frac{1}{2}J_{m-1}^2(\alpha_{m,n})}{\left[\frac{4}{\pi w^2}\int_0^1 xI_0(\frac{4x\delta}{w^2})J_0(\alpha_{m,n}x)e^{-\frac{2(x^2+\delta^2)}{w^2}}dx\right]^2}. \tag{2.26}$$

It is clear that the effective mass depends of the measurement position.

The Eq. 2.16 gives a zero overlap and therefore infinite effective mass for the mechanical mode of $m > 0$, $\forall n$ and for a $\vec{\delta} = 0$ see Fig. 2.4. In the experiment, however, the alignment of the optical beam with respect to the membrane is not perfect, such that there is a residual overlap even for $m > 0$ mode. The vacuum optomechanical coupling $g_0 = Gx_{ZPF}$, where in $x_{ZPF}$

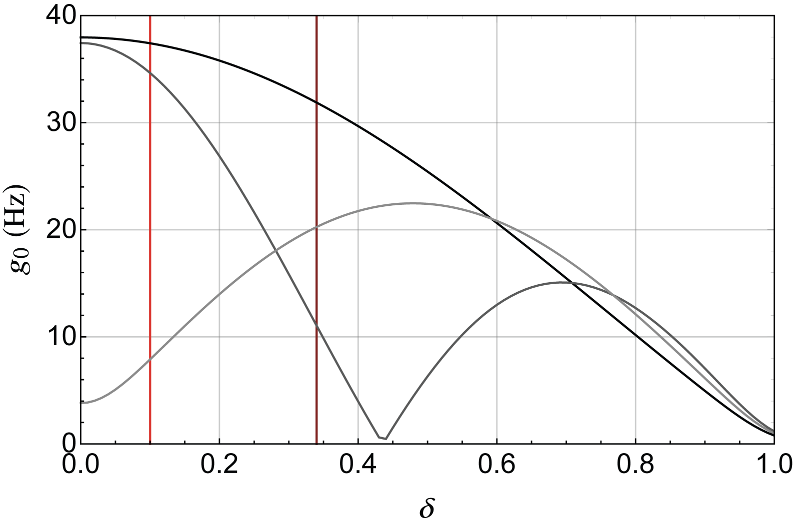

Figure 2.5: Trend of $g_0$ as a function of the position shift $\delta$ for different mechanical modes, the black line the mode $(0,1)$, the dark grey line the mode $(0,2)$ and gray line the mode $(1,1)$, where with the vertical lines, red and dark red, are shown the two different positions of the cavity beam.

appears the dependence from the effective mass, depends on the overlap between the cavity mode and the membrane ones. Due to that, $g_0$ is rightly dependent of the cavity beam position. For this reason, in the Tab. 2.1, we show some value of the effective mass $M_{eff}$ and the optomechanical vacuum coupling $g_0$ obtained for the two different cavity configurations and for three considered modal mode: $(0,1)$, $(1,1)$ and $(0,2)$. Indeed, in the Fig. 2.5 is shown a full description of the $g_0$, for the three some modes, as a function of the normalized beam position $\vec{\delta}$. We evidence, by two vertical lines (dark red and red), the two positions for the cavity beam on the membrane.

As we said, we studied the system for two different positions of the cavity spot on the membrane. In the first configuration we focus the work on one of the quasi degenerate mechanical mechanical mode $(1,1)$ at 370 kHz, and considering only the one more coupled with the cavity beam. This configuration will be used in the work described in the Ch. 3. The overlap function $D$, described in the Eq. 2.16, has a value close to 54% for one of the quasi degenera mode and almost zero for the other. That value is calculated considering a shift close to 0.28 mm (we will discuss later that measurement method) that corresponds to $\delta = 0.34$. The value of effective mass, normalized to the physical mass, and the $g_0$ for the interested mechanical modes are shown in the Tab. 2.1. Before the parametric squeezing work, the spot on the membrane was realigned, obtained a better centering (shift from the center less of 0.1 of the membrane radius). Here, one of the best coupled mode is the $(0, 2)$ at 530 kHz, the overlap is close of 90%. For that position the theoretical value of the vacuum optomechanical coupling and normalized effective mass are shown in the Tab. 2.1. In the next subsections we will report the membrane physical parameters and how the oscillator influences the cavity proprieties.

## Membrane specs

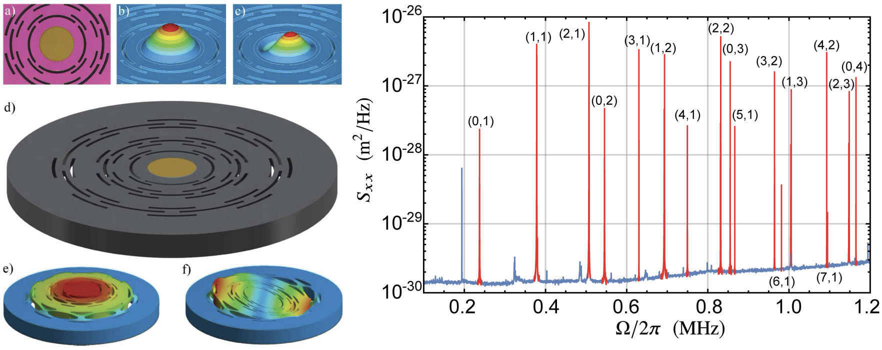

Figure 2.6: Left panel: a) Optical microscope picture of the circular membrane, with diameter 1.64 mm and thickness 100 nm. b) and c) first modal shapes involving the membrane, resonating at about 230 and 366 kHz, respectively, similar to the constrained membrane's normal mode $(m, n) = (0, 1)$ and $(m, n) = (1, 1)$. d) CAD image of the device. e) and f) modal shapes of the lowest frequency resonances of the device, respectively, at 32 and 47 kHz, where the planar displacement of the membrane frame can be seen. The pictures are taken from [10]. Right panel: A typical displacement spectrum of the membrane at room temperature. All the mechanical modes are marked in red.

The optomechanical cavity is based on a silicon nitride ($SiN_x$), circular membrane oscillator, supported by a silicon (Si) frame. It is made by a col-

| | |
|---|---|
| Diameter, $l_x = l_y$ (mm) | 1.64 |
| thickness, $l_z$ (nm) | $97.27 \pm 0.01$ |
| mass, $M$ (kg) | $6.57 \times 10^{-10}$ |
| Index of refraction, $n$ | $2.0210 \pm 0.0005$ at 1064 nm |
| Absorption coefficient, $n_i$ | $(2.00 \pm 0.08) \times 10^{-6}$ at 1064 nm |
| Young's modulus, $E$ (GPa) | $200 - 400$ |
| Poisson ratio | 0.27 |
| Tensile stress (GPa) | 0.8 |
| Density, $\rho(\mathrm{kg/m^3})$ | 3200 |
| Thermal expansion coefficient, $\alpha$ ($10^{-6}$ m/K) | 2.3 |
| Heat capacity per unit volume, $C_v$ ($\mathrm{J/m^3K}$) | 710 |
| Coeff. of thermal diffusion, $D_T$ ($10^{-3}$ $\mathrm{Wm^2/J}$) | 9.29 |

Table 2.2: Material properties of SiN. Values extracted from [10, 11, 72]

laboration between the University of Trento and the Technology University of Delf. The optomechanical membranes fabrication is based on Deep Reactive Ion Etching (DRIE). This technique enables the fabrication of a complex structure around the membrane, used to isolate the membrane from its support. This allows to maintain a high mechanical Q-factor ($10^7$) for all the membrane mechanical modes. The details of its fabrication are described in the work [72].

The membrane used in this experiment has a mass of $6.57 \times 10^{-10}$ kg, and a diameter of 1.64 mm. The thickness is $\sim$ 100 nm and the $Q$-factor is $10^7$. The membrane stress is $\sim$ 0.8 GPa. The resonance frequency of the membrane fundamental mechanical mode is 240 kHz. The membrane is incorporated in a 1 mm thick silicon plate. All the membrane parameters are shown in the Tab. 2.2. In the right panel of Fig. 2.6 is shown a typical displacement spectrum at room temperature, where the mechanical modes are marked in red. The displacement spectrum is acquired by the homodyne balanced detection at room temperature (RT) without any optical cooling effect. The spectrum is calibrated in terms of $\mathrm{m^2/Hz}$.

### Membrane Reflectivity and Transmissivity

In the optomechanical cavity in configuration "membrane-in-the-middle" the cavity finesse is linked to the position of the membrane. To get a more general

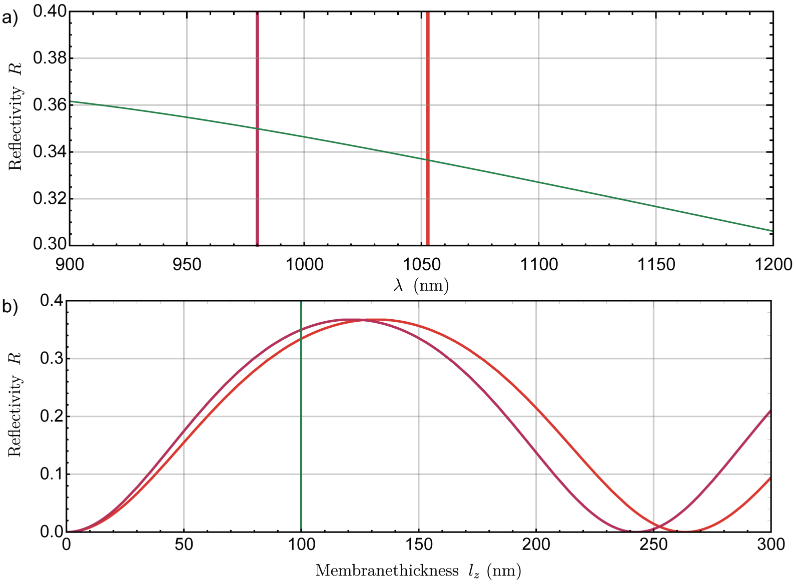

Figure 2.7: a): The SiN membrane reflectivity as a function of the $\lambda$, calculated for a membrane thickness of 100 nm (Green line). Dark red line at 980 nm and red line at 1064 nm indicates the interestingly wavelengths. b): The power reflectivity as a function of the membrane thickness, field at 980 nm (dark red line) and field at 1064 nm (red line). Green line, membrane thickness of 100 nm.

description, we can start by describing the membrane reflection and transmission coefficients. At this propose we use the transfer matrix approach for a 2D thin film ($l_x, l_y \gg \lambda,\ l_z \ll \lambda$). With this method we can link the transmitted electromagnetic field amplitudes $E(l_z)$ and $H(l_z)$, to the fields at the boundary of the membrane $E(0)$ and $H(0)$ with the the wavelength dependent refractive index $n(\lambda)$:

$$\begin{pmatrix} E(l_z) \\ H(l_z) \end{pmatrix} = \begin{pmatrix} \cos\beta & \sin\beta/k \\ -k\sin\beta & \cos\beta \end{pmatrix} \begin{pmatrix} E(0) \\ H(0) \end{pmatrix} \tag{2.27}$$

where $\beta = kl_z$ it defines the phase shift generated by the SiN film, $k = 2\pi n/\lambda$ is the laser light wave vector. The reflective index of our membrane is shown in the Tab. 2.2. The transfer matrix approach can be used to calculate the field amplitude reflected off and transmitted through the membrane.

The transmission and reflection coefficients are, respectively, $t = E_t/E_i$ and $r = E_r/E_i$ [72]:

$$r = \frac{(1-n^2)\sin\beta}{2in\cos\beta + (n^2+1)\sin\beta}, \tag{2.28}$$

$$t = \frac{2n}{2in\cos\beta + (n^2+1)\sin\beta}. \tag{2.29}$$

If we consider a system in absence of absorption, the coefficients for the power reflection and transmission are, respectively, $R = |r|^2$ and $T = |t|^2$, where $R+T = 1$. The membrane used has a thickens of 100 nm, the reflected power, for the 1064 nm wavelength, is $\sim 33\%$. In Fig. 2.7 we display the membrane reflectivity as a function of the wavelength $\lambda$, and the membrane thickness $l_z$. We show the trends for the two laser used in our work at 1064 nm and $\sim$ 980 nm, where the difference in reflectivity are negligible. Due to the low reflectivity the membrane can not be used as end cavity mirror, therefore the membrane is placed in a high finesse Fabry-Pérot cavity, without spoiling the finesse thanks to the low absorption rates. In the real case the membrane absorbs part of the light field, its refractive index is $n = n_r + in_i$ [72]. It has an imaginary part that keeps into account the amount of attenuation while travelling through the medium. The SiN membrane absorption is very small, $\sim 2 \times 10^{-6}$ at 1064 nm.

## The membrane-in-the-middle cavity

As a further step, we will describe the optomechanical system, membrane-in-the-middle. We consider a Fabry-Pérot cavity with an input coupler having $|r_1|^2 + |t_1|^2 = 1$ and $\sigma_1 = 0$, and an output coupler with $|r_2|^2 + |t_2|^2 = 1$, $\sigma_2 = 0$, where the $\sigma_{1,2}$ are the mirror losses. The two couplers are separated by a distance $L$. Considering the membrane placed approximately in the cavity center. The classical fields, inside and outside the cavity, is described by using the transfer matrix method, for that the linear system that describes the optomechanical cavity is:

$$\begin{pmatrix} a_t \\ 0 \end{pmatrix} = M_{tot} \begin{pmatrix} a_{in} \\ a_r \end{pmatrix} \tag{2.30}$$

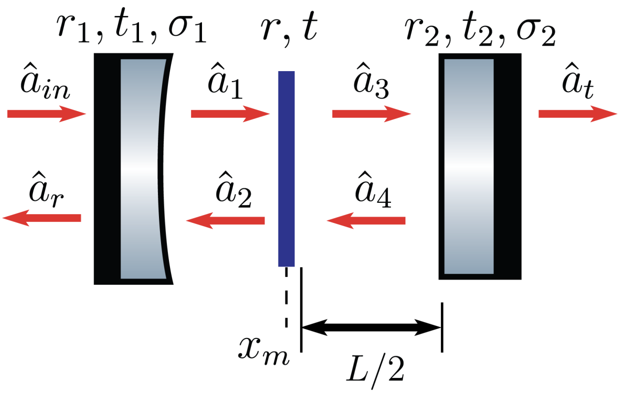

Figure 2.8: Scheme of the membrane-in-the-middle cavity. With red lines are shown all the coupled fields and with the blue one is shown the membrane, placed approximately in the middle of the cavity. In our setup, due to the high reflectivity of the back mirror, $a_t \approx 0$.

where the total matrix is obtained by considering five elements:

$$M_{tot} = \begin{pmatrix} \frac{r_2^2}{t_2} + t_2 & -\frac{r_2}{t_2} \\ -\frac{r_2}{t_2} & \frac{1}{t_2} \end{pmatrix} \begin{pmatrix} e^{2\pi i(l_2 - x_m)} & 0 \\ 0 & e^{-2\pi i(l_2 - x_m)} \end{pmatrix}$$
$$\begin{pmatrix} \frac{r^2}{t} + t & -\frac{r}{t} \\ -\frac{r}{t} & \frac{1}{t} \end{pmatrix} \begin{pmatrix} e^{2\pi i(l_1 + x_m)} & 0 \\ 0 & e^{-2\pi i(l_1 + x_m)} \end{pmatrix} \begin{pmatrix} \frac{r_1^2}{t_1} + t_1 & -\frac{r_1}{t_1} \\ -\frac{r_1}{t_1} & \frac{1}{t_1} \end{pmatrix} \tag{2.31}$$

The first and last transfer matrices show the contribution of the cavity mirrors. The second and fourth matrices describe how field pass trough an empty medium with different lengths, normalized by $\lambda$, respectively $l_2 - x_m$ and $l_1 + x_m$. $l_1$ is the left sub-cavity length and $l_2 = l - l_1$ is the right sub-cavity length, where $l$ is the cavity length normalize at the laser wavelength $l = L/\lambda$ (in the usual configuration we have $l_2 = l_1 = l/2$). The relative accumulated phases are $i2\pi l_1$ and $i2\pi l_2$. The center matrix shows the membrane placed at $l_1 + x_m$ from the input cavity mirror. The membrane have the reflection and transmission coefficients respectively $r$ and $t$. $a_r$ and $a_t$ are respectively the reflected and transmitted field, the total cavity coefficients can be obtained by the equations:

$$r_{tot} = -\frac{M_{21}}{M_{22}}, \qquad t_{tot} = M_{11} - \frac{M_{21}}{M_{22}} M_{12}. \tag{2.32}$$

Considering now a cavity in asymmetric configuration, where the transmission of output mirror is much smaller than the input one ($|t_1|^2 = 315$ ppm , $|t_2|^2 = 10$ ppm), we will discuss only the results applied to our setup. We do not consider a possible membrane angle with respect to the cavity axis. The resonance frequency is given by the laser wavelength, $\lambda$, the membrane position $x_m$ and its reflectivity, $r$. The phase of $r$ gives an offset to the resonance. On the other hand, the cavity finesse can change with the membrane position. Here, we can define the finesse as the total one of the cavity. To have a description of the finesse and optomechanical coupling as a function of the membrane position, we performed a numerical estimation of the frequency and linewidth of the transmission resonance. The model results are shown in the Fig. 2.9a) and 2.9b). Fig. 2.9a) shows the finesse trend as a function of the membrane position normalized to the laser wavelength. The maximum cavity finesse is when the membrane is close to the cavity node, i.e. $\lambda/2$. In an asymmetric configuration, the finesse of the optomechanical cavity can be higher than the empty one. Considering a symmetric system where a cavity Fabry-Pérot is composed by two identical mirrors, the finesse can reach at the maximum a value of the empty cavity one. This is the biggest difference compared with an asymmetric cavity, an example is shown in the work [40]. The finesse dependence on the position of membrane is the

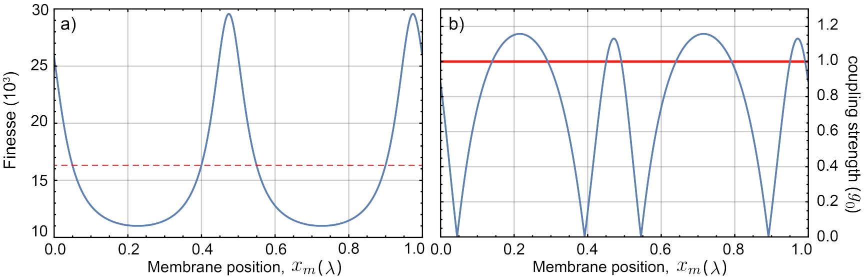

Figure 2.9: a): Cavity finesse as a function of the membrane position normalized to $\lambda$. Red dashed line shows the theoretical finesse of the empty cavity. b): Simulation of the vacuum optomechanical coupling in our configuration. It is maximum for the cavity node and anti-node, where the finesse is maximum and minimum respectively. For the membrane in the middle setup the vacuum optomechanical coupling can be reach the $g_0 = \omega_{cav}/L$, red solid line.

explanation of the change in finesse when cooling the system to cryogenic regime. In our experiment, the finesse at room temperature is close to 16500 but at cryogenic temperature the finesse reaches 20000 or more.

The results of the numerical solution for the optomechanical gain is shown in the Fig. 2.9b), (normalized to $g_0 = \omega_{cav}/L$ i.e. to the equivalent end-mirror coupling strength) where the maximum couplings are in the cavity node and anti-node, respectively, where the finesse has a maximum and the minimum.

In conclusion, even if the oscillator has a moderate reflectivity, the optomechanical coupling strength of the membrane, placed in the center of a cavity, can reach values similar to the standard end mirror configuration or better.

## Finesse measurement

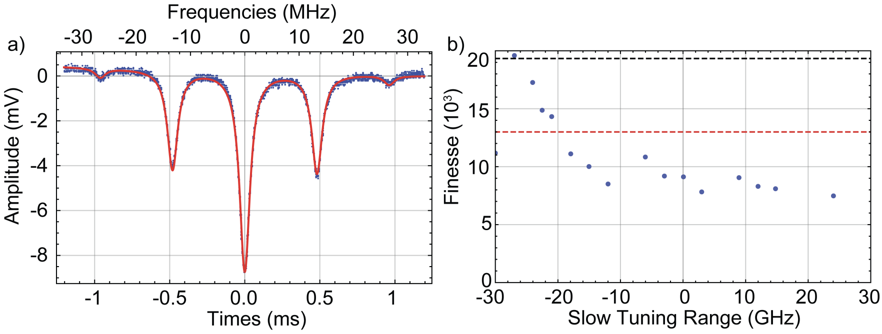

Figure 2.10: a) Example of the finesse measurement, where the red solid line shows the fit function at five Lorentzian shapes, the blue dots are the experimental data. Horizontal upside label shows the converted scale in frequency. b) Example of the finesse measurement for different position of the laser tuning range. It is make on all the possible range from −10 V to 10 V where its gain is −3 GHz/V. The dashed red line shows the measured finesse value at room temperature. The black dash line shows the maximum value of the finesse for our empty cavity.

As previously explained, an important cavity parameter is the finesse. For its measurement we use the modulation at 13.3 MHz on the probe beam, used to generate the PDH error signal. We use one photodiode of the balance detection, to observe the reflected cavity beam with the two modulation sidebands. The known frequency distance between the carrier and two sidebands is used to calibrate the time axis into a frequency. An example of it is shown in the Fig. 2.10a). From the fit (red line in the figure) we measure the linewidth of the carrier peak $\kappa_t$ and the distance in time between the carrier and the sidebands $\delta_t$. The ratio between distance in frequency and time gives the conversion coefficient 13.3 MHz $/\delta_t$. This conversion coefficient is used to calibrate the linewidth in frequency ($\kappa = \kappa_t \times 13.3$ MHz $/\delta_t$), and from an independent measurement of the cavity $FSR$, that is previously described, we derive the cavity finesse $\mathcal{F} = \frac{FSR}{\kappa}$. At cryogenic temperature, before any other measurement, the system is characterized by measuring the finesse as a function of the laser frequencies at the purpose to find the best coupling point. An example of the full frequency range is shown in the Fig. 2.10b). For the measurement we choose the best finesse point where also the optomechanical coupling is maximum. As it is possible to observe in that figure, at cryogenic temperature the finesse grows up compared with the best finesse value reached at room temperature. It is probably generated by small tilt of the membrane thermal stress. Due to the thermal stress the positions of the cavity node and anti-node change, giving a better coupling between the cavity mode and the mechanical one. We work on the laser frequency where the finesse is maximum that correspond to the higher optomechanical coupling.

### 2.1.2 Cavity spot position on the membrane

In this subsection we describe the possible cavity deformations during the cooling cycle. During the temperature decrease, we have kept the alignment between the injected laser and the cavity. The most important thermal contractions effects occur above 70 K since, below this temperature the expansion coefficient drops to low values. The cavity movements are due to the displacement of the cryostat itself. They can be easily followed by using the alignment mirrors. It is important to verify that the cavity itself does not deformed too much since such deformation can be hardly compensated. In particular it is crucial to verify that the position of the cavity axis with respect to the membrane does not change. In order to see if the beam spot on the membrane moves or not, we have acquired several photos at different values of temperature. We have used an editing program to compare such images. In particular in Fig. 2.11 we show the comparison between two

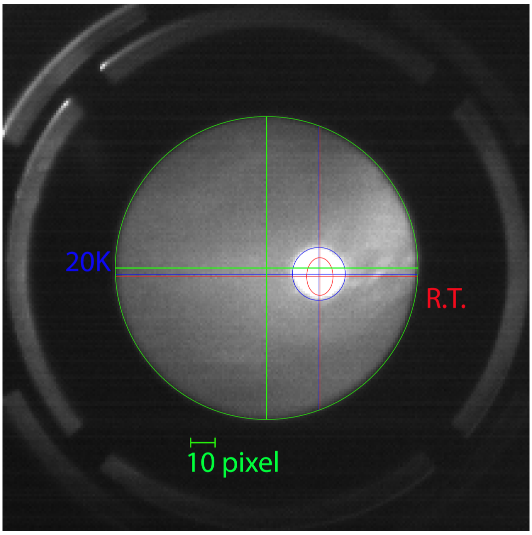

Figure 2.11: Photo of the membrane inside optical cavity taken at 20 K. The blue lines identify the waist center in the photo at 20 K. The red ellipse and the red lines give the position of the waist center, in the photo taken at room temperature. The green lines and the green border identify the center of the membrane. This picture is taken with the horizontal and vertical axis flipped.

images at room temperature and at 20 K. At the purpose to identify the position of the spots, we have chosen as reference, the center of the membrane in both images, and we have measured the spot positions. All positions are taken in number of pixels and converted into real displacement using the known membrane diameter of 1.64 mm. The diameter in number of pixels is 125. We derive that one pixel on the image corresponds to 13.1 $\mu$m. The shift between the spots at two temperatures is just 2 pixels i.e. 26 $\mu$m. The waist of the cavity is 70 $\mu$m, this means that we do not observe a significant shift. This is an important result, showing that the cavity with this membrane remains well aligned. We can state that our optomechanical cavity works properly at cryogenic temperature. Thanks to this measurement procedure, we obtain the distance between center of the membrane and cavity spot. In the first used configuration, the displacement of cavity spot from the membrane center is 0.28 mm, in the vertical axis. We will use this distance to calculate the effective mass of the mechanical modes, whose values are reported on Tab. 2.1. Using the some procedure we measured the spot position for the second configuration, where we identify a displacement from the center close to $\delta = 0.1$ a long the vertical membrane axis. In this configuration the symmetric modes are much more coupled than the other ones, indeed for this configuration the best coupled mode is the $(0, 2)$ (excluding the fundamental one $(0, 1)$) no more the $(1, 1)$.

## 2.2 Quality factor

The quality factor $Q$ is a very useful parameter to characterize and compare losses of resonators. Today exist many way to define that parameter, all become very similar in the limit of higher $Q$. For example in the frequency domain, the quality factor can be defined by

$$Q = \frac{\Omega_m}{\Gamma_m} = \frac{|\chi(\Omega_m)|}{|\chi(0)|} \tag{2.33}$$

where $\Omega_m$ being the resonance frequency, $\Gamma_m$ is the full width at half maximum of the resonance and $\chi$ is the transfer function, Eq. 1.9. The ratio shows how much energy the oscillator can stored in the resonance. In our oscillator, SiN membrane, the quality factor is very high, implying a sub Hz $\Gamma_m$. In the time domain the quality factor can be defined as [70]

$$Q = 2\pi \frac{E}{\Delta E}. \tag{2.34}$$

Here, $E$ is the energy stored in the oscillator, $\Delta E$ is the energy loss per cycle. The loss mechanisms contributions, in reality, have different sources. The overall $Q$ is the inverse sum of $Q$ factors attributed to each loss channel, why the loss channels are inversely proportional to the quality factor, as the loss added in Eq. 1.4.

$$\frac{1}{Q} = \frac{1}{Q_{vis}} + \frac{1}{Q_{str}} + \frac{1}{Q_{clamping}} \tag{2.35}$$

where the losses due to the viscous mechanism gives $Q_{vis} = \Omega_m/\Gamma_{gas}$, and the structural damping gives $Q_{str} = 1/\phi$. The last considered damping is generated by the clamping. In it, other losses due to the the membrane assembly into the optomechanical cavity are considered. Before describing how the quality factors of mechanical modes were measured, we describe in detail some contributions to the quality factor, such as thermal and structural contributions.

### 2.2.1 Q-factor damping

**Recoil damping**

As describe in the work [10], the strongest contribution to the dissipation is what is called recoil damping (structural damping, $Q_{str}^{-1}$). It is due to the combination between vibrations of the membrane and that of the support. The effective quality factor, in this framework, of a resonant membrane supported by a wafer is

$$\frac{1}{Q} = \frac{1}{Q_m} + \frac{1}{Q_w}\frac{M_m}{M_w}\frac{\Omega_w^2\Omega_m^2}{(\Omega_w^2 - \Omega_m^2)^2} \tag{2.36}$$

where $Q_m$, $M_m$, $\Omega_m$ are the intrinsic quality factor, mass and resonant angular frequency of the membrane, $Q_w$, $M_w$, $\Omega_w$ are the identical parameters for the support wafer. The strongest reduction of the quality factor, according to the equation, is when the wafer frequency is equal to the mechanical one, $\Omega_m = \Omega_w$.

For this reason the membrane used in this work is designed to reduced the contribution of the recoil damping, and obtain an higher level of homogeneity of the $Q$-factor. The design and realization processes are described in the works [10, 72]. The oscillator is designed with specific on-chip structure working as a loss shield for the membrane. The lowest resonance frequency has the highest quality factor and reaches the limit set by the intrinsic dissipation. A cylinder of diameter 2.4 mm and thickness 1 mm supports the membrane. It is supported in four points by a structure made of alternating flexural from torsional springs with a thickness of 280 $\mu$m (see Fig. 2.6). The purpose is to isolate the internal resonator of the cylinder and the rest of the structure. To decrease the coupling of the membrane with the wafer, the cylinder structure is repeated two more times. The fabrication of this membrane is showed in the work [72]. The $Q$-factor reaches a value of $\sim 10^7$ for many mechanical mode. In the following section, we will describe the technique implemented to measure the membrane quality factor after it is mounted into the optomechanical cavity.

**Low temperature effects**

### Gas Damping

An important result is the increase of the quality factor at cryogenic temperature, where several effects take place at the same time, involving gas damping and internal friction of the membrane. The low temperature of 7 K gives an additional isolation. One dissipation channel is the gas damping at a given pressure of the vacuum chamber. It is due to the momentum transfer to air molecules. This process add a loss channel as a function of the pressure. The quality factor due to the air molecules is described by the equation [7, 32]:

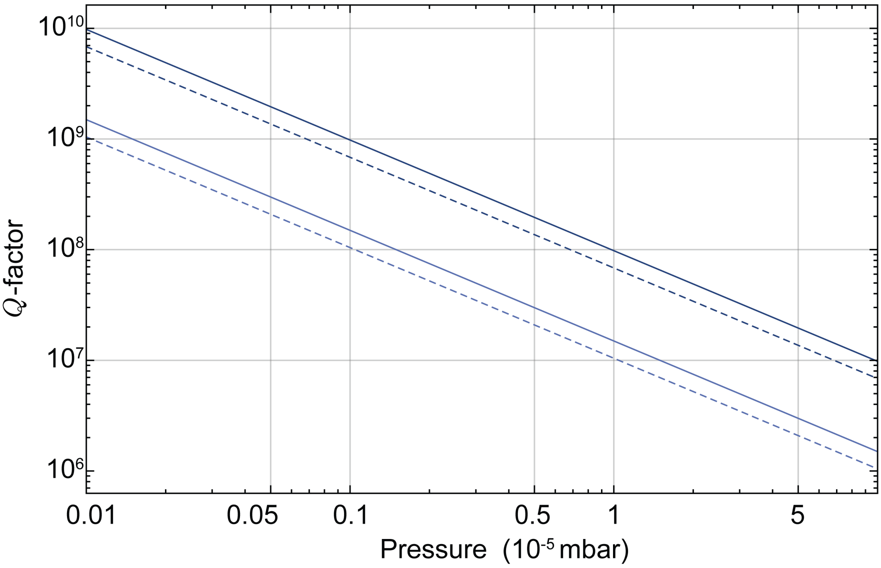

Figure 2.12: Quality factor due to gas damping as a function of the pressure for two temperature RT and CT, shown respectively with dark blue and blue lines. The $Q_{air}$ is shown for two mechanical modes $(0, 2)$ at $\sim 530$ kHz (solid lines) and $(1, 1)$ at $\sim 370$ kHz (dashed lines).

$$Q_{air} = (\pi/2)^{3/2} \frac{\sqrt{R_0 T/M_m}}{p} l_z \rho f_m \tag{2.37}$$

where $R_0 = 8.31$ J/molK is the gas constant, $\rho = 3200$ kg/m$^3$ and $l_z = 100$ nm are the membrane density and thickness, $M_m = 29$ g/mol is the molar mass of the surrounding air, $T$ and $p$ are, respectively, the temperature and pressure of the environment. The behavior described by Eq. 2.37, is shown in Fig. 2.12, where $Q_{air}$ is plotted for two different temperatures, room temperature (RT) and cryogenic temperature (CT), 7 K, shown respectively with dark blue and blue lines. The pressure of the vacuum chamber is close to $10^{-5}$ mbar, kept by pumping with an ionic pump. At the cryogenic temperature the pressure arrives at $10^{-7}$ mbar due to additional cryogenic pumping. The cryogenic pumping has a fundamental role in the increasing quality factor at the maximum value.

**Thermoelastic**

Another important contribution at low temperature is due to the thermoelastic losses. In this channel the losses are considered to stretching or compression of the resonators material. This effect increases or decreases the local temperature of the material. The temperature gradient is linked to energy dissipation when the oscillator is heating and vice versa [35]. Using the fluctuation-dissipation theorem [16,17], we can link the thermal fluctuations to the a displacement noise. The equation for the loss angle is [18,36]

$$\phi_{thelastic} = \frac{E\alpha^2 T}{C_v} \frac{\Omega_m \tau_d}{1 + \Omega_m^2 \tau_d^2} \tag{2.38}$$

where $E$ is the Young's modulus, $\alpha$ the thermal expansion coefficient, $C_v$ is the heat capacity per unit volume. $\tau_d$ is the geometry and material time constant. For the membrane the equation for $\tau_d$ is $\tau_d = l_z^2/\pi^2 i D_T$, where $D_T$ is the thermal diffusivity, and $l_z$ is the membrane thickness. For our SiN membrane the geometric and material parameters are shown in the Tab. 2.2, considering the mechanical mode $\Omega_m/2\pi = 530$ kHz. At room temperature (300 K), we have a value of $\phi_{thelastic} \approx 2.4 \times 10^{-7}$, implying $Q \approx 4.2 \times 10^6$. This value is only a guide value, indeed several parameters can change or are not exactly known. At 7 K, the quality factor due to the thermoelastic channel is $\sim 2 \times 10^8$, therefore this effect gives another explanation of the quality factor increasing at cryogenic temperature.

Considering all these contributions we can explain how the $Q$-factor increases at cryogenic temperature, but the membrane quality factor has an upper limit due to the recoil damping, $10^7$.

### 2.2.2 Q-factor measurement protocol

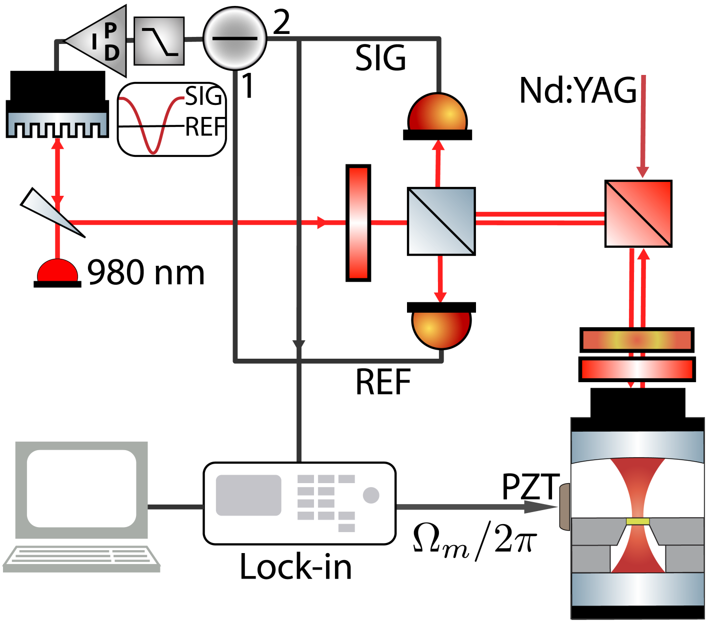

Figure 2.13: Set-up used for the Q-factor measurement.

The experimental apparatus used for the quality factor measurement is shown in Fig. 2.13. To implement this measurement are used a laser at 980 nm. The input and output OMC mirrors are design to obtain a high cavity finesse for the Nd:YAG laser at 1064 nm, where the minimum transmissions are respectively 315 ppm and 10 ppm. The mirrors transmission for the laser at 980 nm is much higher, but otherwise the cavity remains in configuration well coupled, since the mirror losses remain identical for the two lasers. The finesse in the 980 nm configurations is $< 200$, while it is $\sim 20000$ with the 1064 nm laser at zero losses. The purpose of working at low finesse is to decrease the optomechanical effects and to study the free mechanical behavior of our oscillator. The concerned laser is a diode laser, where the single mode is selected by a gratting, and a PZT glued on it allows to control the laser cavity length. It is used in the servo loop implemented in the cavity lock. The 980 nm laser is sent on the optical path by a dichroic mirror (high pass, 1064 nm is transmitted and 980 nm is reflected at 45°).

Before the dichroic mirror a PBS and a $\lambda/2$ allow to split the beam in two, the reflected one is sent on a photodiode to generate a "Reference" in the lock scheme ($\sim$ 2 mW), the transmitted one is sent trough a $\lambda/4$ and after of a dichroic mirror to the cavity. The reflected beam from the cavity comes back on the second photodiode used like "Signal" in the lock scheme. The two photodiode signals are subtracted and sent into a servo loop circuit to lock the cavity. The cavity lock reference level is selected by the power of the Reference beam. In this configuration the cavity lock occurs in two frequency positions, obtained by switching the two input signals in the difference box. This is done to verify the presence of the optomechanical effects on the quality factor measurement. The lock correction signal is sent into the grating PZT, to keep the cavity locked in resonance. The Signal beam is sent also to a Lock-in amplifier for the decay detection. The oscillator excitation at the natural mechanical frequency $f_m$ is realized by a PZT glued on the cavity basement. The excitation signal is generates directly from a Zurich lock-in amplifier, used as a function generator. The signal is demodulated at a frequency $f_{dem}$ close to the resonance one, $\delta f = f_m - f_{dem}$. The optomechanical residual effects are given by the difference of $\delta f$ between the two lock configurations, $f_{dem}$ is kept fix. The difference in $f_m$ can be explained by small difference in detuning between the two cavity locks, therefore the oscillator spring is modified by the optomechanical effects, Eq. 1.99. All the residual optomechanical effects can compromise the goodness of the quality factor measurements.

The measurement protocol consists in applying an external force to excite the oscillator. For this reason we drive the external PZT with a sinusoidal wave-function at the natural mechanical frequency $f_m$. To measure the decay we quickly move the external force out of resonance (it is shifted by 10 kHz), the resonator whole motion is described by the following equation:

$$x(t) = x_0 \ \cos(2\pi \ \delta f \ t) \ e^{-t/\tau} \tag{2.39}$$

where $x_0$ is the amplitude of the mechanical mode just before the modulation is switched off. The decay time, $\tau$ is linked to the quality factor: $Q = \pi f_m \tau$. An example is showed in Fig. 2.14. At the propose to characterize the membrane modes, we measured the quality factor for each cavity configuration, where we used the same membrane. The quality factor was also studied at room temperature (RT) and at cryogenic temperature (CT) close to 7 K. The measurement in the two cavity configurations are displayed in Fig. 2.15. In panel a) are report the quality factor relatively to the first studied system

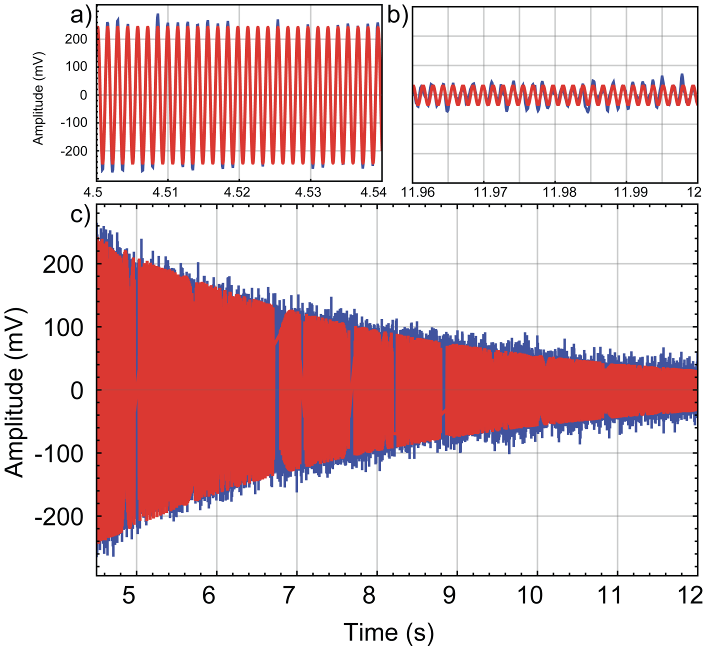

Figure 2.14: Example of a decay trace of the mechanical mode at 530 kHz. The fit gives a decay time of 3.8 s and a quality factor close to $6.4 \times 10^6$. Panels a) and b) show respectively the first and last 40 ms of the time trace. In panel c) is shown the full decay. The blue and the red lines show respectively the measured data and the fit using the function 2.39.

where the cavity spot was membrane off-centered by $\sim 0.28$ mm. In panel b) the data show the results in the second configuration where the cavity beam is more centered. In both cases the blue dots, with the relative error bars, show the $Q$-factor at 7 K, the red dots show the measurement at RT. The error bars give the standard deviation calculated on eight measurements for each mechanical mode. More in detail, for each cavity lock setup we acquired four decays, in total eight measurements for each mechanical mode. The final quality factor is obtained by averaging the inverse of two quality factors measured for the two cavity lock configurations:

$$\frac{1}{\bar{Q}} = 2\left(\frac{1}{\bar{Q}_1} + \frac{1}{\bar{Q}_2}\right) \tag{2.40}$$

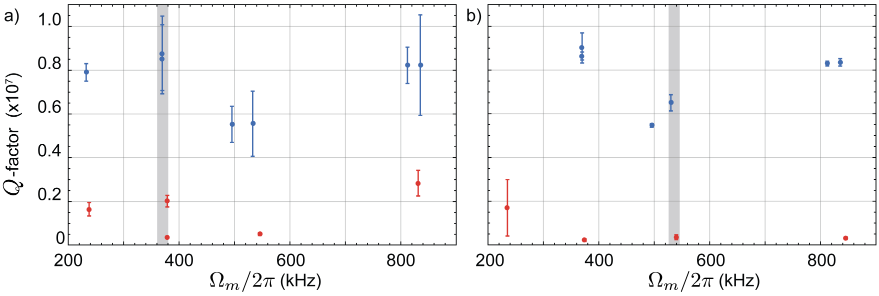

Figure 2.15: Quality factor measured in the two cavity configuration. In the left panel the cavity waist is 0.28 mm far from the membrane center, and in the right panel, second configuration, it is well centered. In the two figures blue data are relative to the measurement at 7 K, while the red ones show the measurement at RT. In both cases the error bars show the standard deviation calculated on 8 measurement. In panel a) the work is focused on the mechanical mode at 370 kHz with a quality factor $\sim 8.5 \times 10^6$. For panel b) we consider for the squeezing work the mechanical mode at 530 kHz where the Q-factor is $6.4 \times 10^6$.

and the error is obtained by error propagation. A good explanation of the $Q$-factor difference is given by the different pressure, gas damping and thermoelastic effects in the two temperature configurations.

## Residual optomechanical effects

We can follow the described procedure only if we do not have any optomechanical effect on the measurement. At the propose of verifying it we observe the fluctuation of the mechanical width $\Delta\Gamma_m$ and the shift of the mechanical frequencies $\Delta\Omega_m$ due to the optomechanical effect. In each lock, we measure the mechanical widths, $\Gamma_m = 1/\tau$, and we compare their values with the mean width on all the data, $\bar{\Gamma}_m$ obtaining two values for each lock: $\Delta\Gamma_{1,2} = \Gamma_m^{1,2} - \bar{\Gamma}_m$. These values are normalized to the mechanical frequency. The results are shown in Fig. 2.16a). In Fig. 2.16b) we show the measurement of the frequency shifts between the two different cavity locks $\Delta\Omega_m = \Omega_m^{1,2} - \bar{\Omega}_m$. In both configurations the values are compatible widthin the error bars, therefore the optomechanical effects are considered negligible in the $Q$-factor measurements.

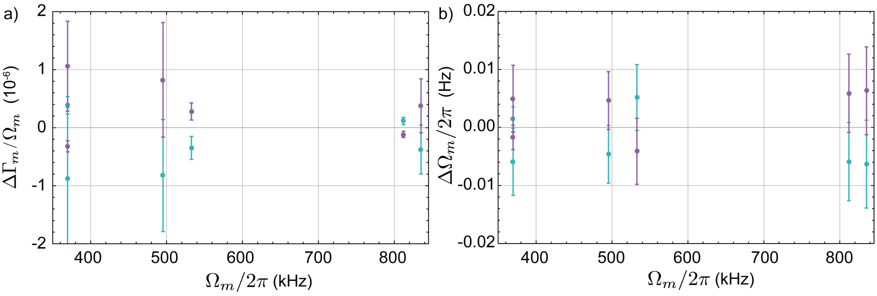

Figure 2.16: In the figures the purple dots and relative bars show the data acquired in the direct lock configuration, and the cyan ones there in the inverse lock scheme. The error bars reflect the standard deviation on four implement measurements. The figures show a typical trend of the two parameters during the quality factor measurement.

For each studied cavity setup we choose a different mechanical mode. To choose the mechanical mode, we consider many parameters as effective mass/-vacuum optomechanical coupling (Tab. 2.1), the quality factor, and the electrical/mechanical noise around the membrane modes in the spectra. Due to the latter effect, we exclude for all our study the fundamental mechanical mode $(0, 1)$ at 230 kHz, because at cryogenic temperature several peaks appear around it. In the first configuration, $\delta = 0.34$, we consider one of the quasi-degenerate modes $(1, 1)$, having a good quality factor, $\sim 8.5 \times 10^6$, and low effective mass, $0.6 \times M$. However, when the $\delta = 0.1$ the consider mode is the $(0, 2)$ at 530 kHz, whose quality factor and effective mass are respectively, $Q = 6.4 \times 10^6$ and $M_{eff} = 0.14 \times M$.

## 2.3 Laser Source

The main laser source is a single-frequency continuous-wave (CW) solid-state laser from Coherent Inc. [38]. The specific model (Mephisto, data-sheet at [38]) is a Nd:YAG laser with a pump diode that emits roughly 0.5 W at 1064 nm. The laser is in semi-monolithic configuration/non-planar. The control is effectuated though a piezo electric transducer (PZT) (named " fast control") that operates directly on the crystal of the laser. This operation generates

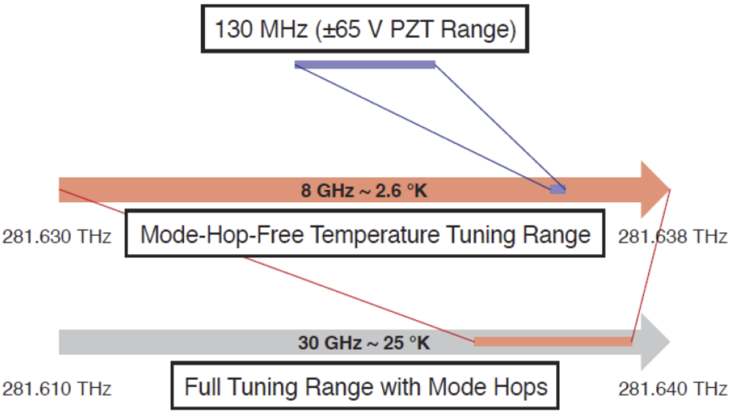

Figure 2.17: Scheme of the frequency control of the Mephisto laser, the figure is taken from [38].

a change on the emission frequency. The response of the modulation is 1.1 MHz/V and it has a response quite flat until 30 kHz (bandwidth of the piezo actuator is about 100 kHz). After that, the piezoelectric resonances of the crystal begin. The maximum tuning range is ±65 MHz, which is sufficient for our purpose. Furthermore the laser has a control of the temperature of the laser cavity. It is a slow control of the frequency (called "slow control") with a time constant few second of a response of $-3$ GHz/°C. The temperature can be varied by an external voltage, at the rate of 1 °C/V. As it is showed in Fig. 2.18, the slow control has linear zone, spaced out by mode hops, with an overall tuning possibility of 40 GHz. In Fig. 2.18 are shown the measured laser mode hops. In the vertical axis we report the measured frequency, and in the horizontal axis the effective laser crystal temperature, measured directly from the laser controller. The spectral linewidth is around $\approx$ 1 kHz integrated over 100 ms and the output mode is a single $\mathrm{TEM}_{00}$ mode. We remark that, the laser monolithic design makes the laser highly frequency stable, for that the relative fluctuations of the resonators length are very small ($\Delta l/l$). It is converted in relatively frequency fluctuation $\Delta f$ at the frequency $f$ as $\Delta f = f \times \Delta l/l$. The Relatively intensity noise (RIN) is specified as $< -140$ dB/Hz at $f > 10$ kHz. The laser has a broader

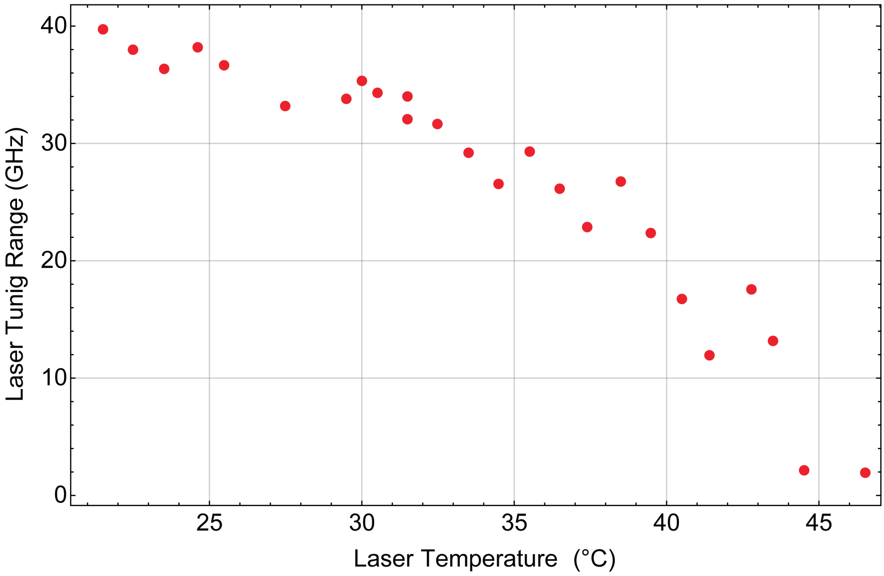

Figure 2.18: Laser Tuning range, by mean of the temperature control.

peak around 800 kHz, due to the laser relaxation oscillations. This peak is completely damped by an active intensity noise stabilization, the so called noise eater.

## 2.3.1 Laser noise

### Quantum Noise

Due to the quantum nature of light, even an ideal laser system is subject to laser noise, i.e., the quantum fluctuations of the photon number, Eq. 1.69. The resulting quantum noise power spectral density for a laser beam with power $P = \hbar\omega_l\, n$ and a measured on a bandwidth of 1 Hz, is $S_{qq} = \frac{hcP}{\lambda}$. It is the called photon shot noise.

As we describe in the Sec. 1.2, there are two main manifestations of the quantum shot noise that we will consider in a typical optomechanical experiment. The first is the so called quantum back-action noise, due to the fluctuating number of photons reflected off and therefore coupled to the mechanical oscillator. This causes a random motion of the oscillator. The second is the read-out noise, it is generated from the fluctuating number of photons at the detection apparatus. The effect of the photon fluctuation will yield fluctuations of the generated photocurrent of the detector. The shot noise has two important properties, first it is frequency independent, second that fluctuations of the power are proportional to the square root of the power, while the fluctuations of classical noise are proportional to the power. The ratio between the quantum and classical noise is proportional to $1/\sqrt{P}$. It increases at low laser power. The real challenge lies in being shot noise limited at large powers that are needed to boost the optomechanical coupling strength $g = g_0\sqrt{n_{cav}}$. Quantum noise, however, is only observed once the laser beam is sufficiently cleaned from classical noise sources.

## Classical Noise

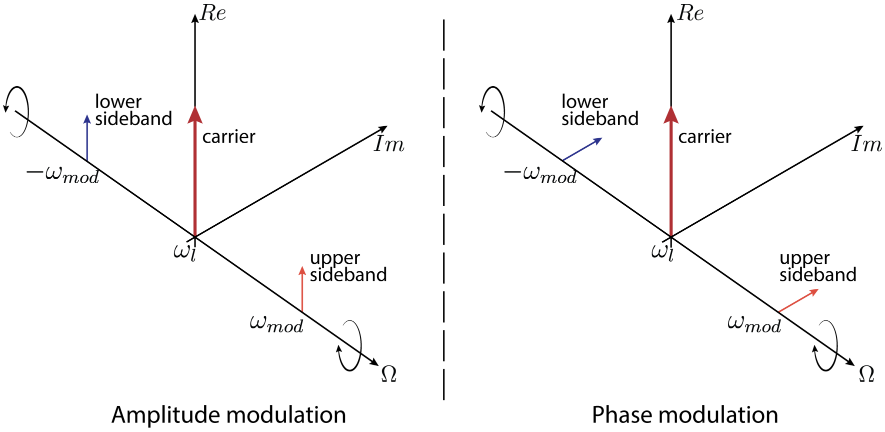

Figure 2.19: Correlated sideband pictures at $\omega_{mod}$ of the amplitude and phase modulation, picture is derived from [78].

All the lasers, in reality, are imperfect and perturbation due to fluctuations of pump power, vibrations of the laser resonator, PZT crystal resonance or thermal effects, might induce additional noise onto the laser field. The classical noise will be distinguish in amplitude (intensity) and phase (frequency) noise.

The amplitude and phase noise can be modeled by a modulation at a fixed frequency $\omega_{mod}$ with an amplitude (am) and phase (pm), modulation depths

$n_{am}$, $n_{pm} \ll 1$ [78]. The equations for the laser field would be written then:

$$a_{am}e^{i\omega_l t} = a_0\ [1 + n_{am}cos(\omega_{mod}t)]e^{i\omega_l t}, \tag{2.41}$$

$$a_{pm}e^{i\omega_l t} = a_0\ e^{i(\omega_l t + n_{pm}cos(\omega_{mod}t))}. \tag{2.42}$$

The equations can be extended using the Bessel functions and the limit of small modulation depths become:

$$a_{am}e^{i\omega_l t} = a_0 \left( e^{i\omega_l t} + \frac{n_{am}}{2}e^{i(\omega_l + \omega_{mod})t} + \frac{n_{am}}{2}e^{i(\omega_l - \omega_{mod})t} \right), \tag{2.43}$$

$$a_{pm}e^{i\omega_l t} \approx a_0 \left( e^{i\omega_l t} + \frac{i\ n_{am}}{2}e^{i(\omega_l + \omega_{mod})t} + \frac{i\ n_{am}}{2}e^{i(\omega_l - \omega_{mod})t} \right). \tag{2.44}$$

From that the laser amplitude noise is modeled as two correlated sidebands rotating in phase with the carrier light at $\pm\omega_{mod}$ modulation. The laser phase noise is described as the amplitude noise, but the noise sidebands are in quadrature with the carrier, at $\pm\omega_{mod}$. In Fig. 2.19a) the sidebands rotate in opposite direction, all contributions along the imaginary axis (phase) cancel out, while along the real axis the two contributions are added to the carrier amplitude. This produces, what is called amplitude modulation. Meanwhile, in Fig. 2.19b) the vectorial addition cancels out all the contribution along the real axis (amplitude), effectively yielding a phase modulation of the carrier along the imaginary axis, phase modulation.

At the end of this section we discuss how the noise sources influence the experimental efforts. The phase noise can be seen as frequency noise, since the frequency is the difference of phase over time, $f(t) = (2\pi)^{-1}\ d\phi/dt$. When the laser is locked to the resonance of the cavity, frequency noise should ideally not drive the mechanics. However, we are not exactly on cavity resonance (lock point drift, or detuned beam used for the cooling), the frequency noise will be converted to amplitude noise and affect the oscillator motion. This conversion is illustrated in Fig. 2.20 [6]. To solve this problem we implement in our setup a filter cavity to decrease the frequency noise produced by the laser itself.

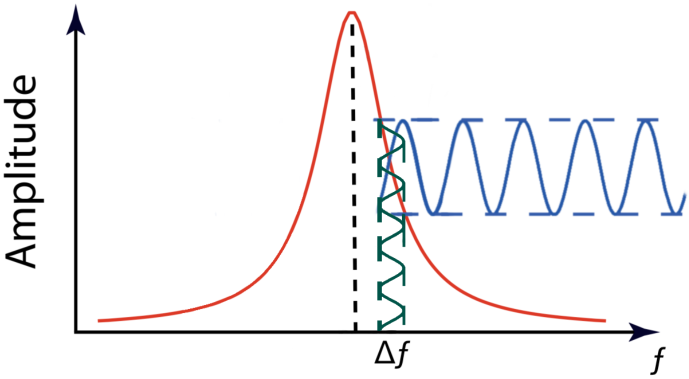

Figure 2.20: Sketch of how the frequency noise in the cavity is converted in amplitude noise in a resonator. This phenomenon may give rise to heating of mechanical modes.

## 2.4 Filter Cavity

For the experiment we need to decrease the classical noise between 200 kHz to $\sim 1$ MHz, where we have the frequency of the interested membrane mechanical modes. The classical noise introduced in the optomechanical cavity by the laser gives an upper limit in the oscillator cooling. At this purpose, we have designed a filter cavity (FC) with a bandwidth below 100 kHz. The FC can be used as a spatial and temporal mode filter. In our work the transmitted beam consists of a single Gaussian mode $\mathrm{TEM}_{00}$. The cavity linewidth, $\kappa_{FC}$, acts almost like an optical low pass for frequencies below it. Indeed the noise frequency at frequencies higher than $\kappa_{FC}$ is reduced according to the transfer cavity function, that is given by

$$\chi_{FC}(\omega) = \left( \frac{1}{1 + i\frac{\omega}{\kappa_{FC}}} \right). \tag{2.45}$$

The cavity linewidth $\kappa_{FC}$ defines the corner frequency of the filter cavity, where the value of the transfer function is $|\chi_{FC}(\kappa_{FC})|^2 = 1/2 = -3$ dB.

The cavity was designed keeping into account the transfer function plots show in the Fig. 2.21. We design it to obtain a strong suppression of the classical noise, requiring the smaller possible cavity linewidth. The cavity linewidth is $\approx 30$ kHz, and the noise reduction is better than $-10$ dB above 500 kHz.

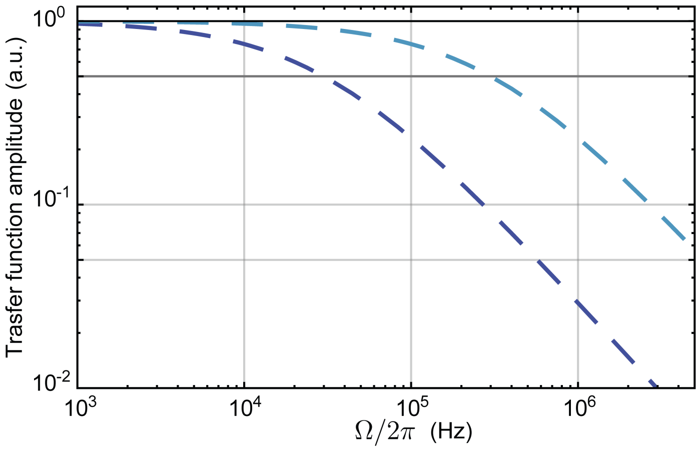

Figure 2.21: Filter cavity transfer functions, calculated as a single low pass filter. Blue dashed line shown a configuration with cavity linewidth equal to $\sim$ 30 kHz (higher finesse). Light blue dashed line show the transfer function for a linewidth of 300 kHz (low finesse). The our setup the higher finesse configuration will be used. The gray line show the corner frequency for the two different cavity configurations. At the interested frequency the cavity reduction is close to $10^{-1}$ i.e. $-10$ dB.

## Frequency Noise Source

Before the filter cavity implementation, we studied the source of the frequency noise in our apparatus. We will start by describing the different methods used to investigate that noise. The spectrum field reflected from the cavity, when the sensitivity is sufficient, is dominated by fluctuations in detuning between the cavity and the incident laser radiation (cavity phase noise). These fluctuations can be determined by fluctuations of the cavity length or fluctuations of the laser frequency or both. Such noise is visible in the homodyne detection, a typical spectrum is shown in Fig. 2.22. To try to understand which of the two contributions is dominating, we have realized a different, longer cavity having roughly the same linewidth of the optomechanical cavity to maintain more or less equal the lock gain.

The new cavity has length equal to 54 mm and has two mirrors with radius 50 mm. The input mirror has a transmission of about 1% and the back mirror is highly reflective, the corresponding finesse is about 600, the free

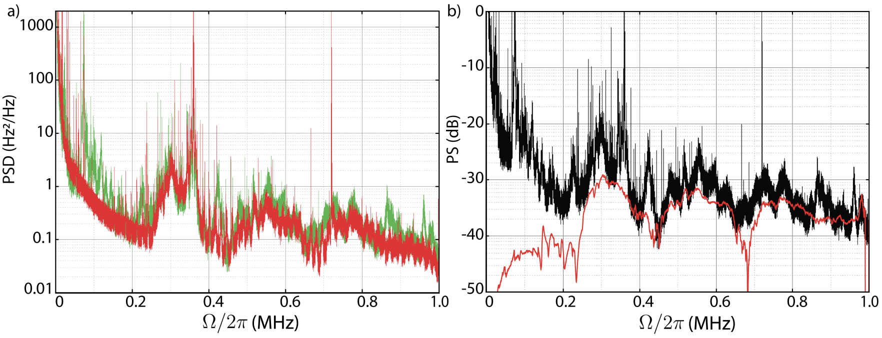

Figure 2.22: Panel a): Comparison between homodyne spectra of the optomechanical cavity (green line) and the of test cavity (red line). Panel b): Comparison between the cavity phase spectrum and the response function of fast control of the laser.

spectral range is 3 GHz. The cavity linewidth is $\sim 5$ MHz. The calculated waist is $w = 0.92$ mm and the Rayleigh distance is $z_R = 24.9$ mm. Using these parameters and the measured position and size of the waist beam exiting from the fiber (0.237 mm), we have derived the position and the focal length of the lenses necessary for the mode matching. After aligning the cavity and optimizing mode matching, we have locked the laser to the cavity (with the laser fast frequency shift) with the usual PDH detection. We have then acquired the spectra using the homodyne detection. The obtained cavity phase noise spectrum, can be compared with that of the optomechanical cavity by calibration of both spectra, either in terms of cavity displacement or in terms of laser frequency noise. In the former case the two spectra become different by several orders of magnitude, on the other hand, in terms of frequency noise, as shown in Fig. 2.22a), they are nearly coincident. The shape of the structure in the spectra are indeed very close, and also quantitatively we arrive to the same level. This is a clear indication that the phase noise in both cavities is dominated by the laser frequency noise.

The further test can also give an indication on the source of the frequency noise. It is performed by sending a modulation signal when the laser is locked to the optomechanical cavity, and detecting the resulting modulations in the detuning using a phase sensitive detection of the PDH signal, with a lock-in amplifier. In this way we actually measure the response function

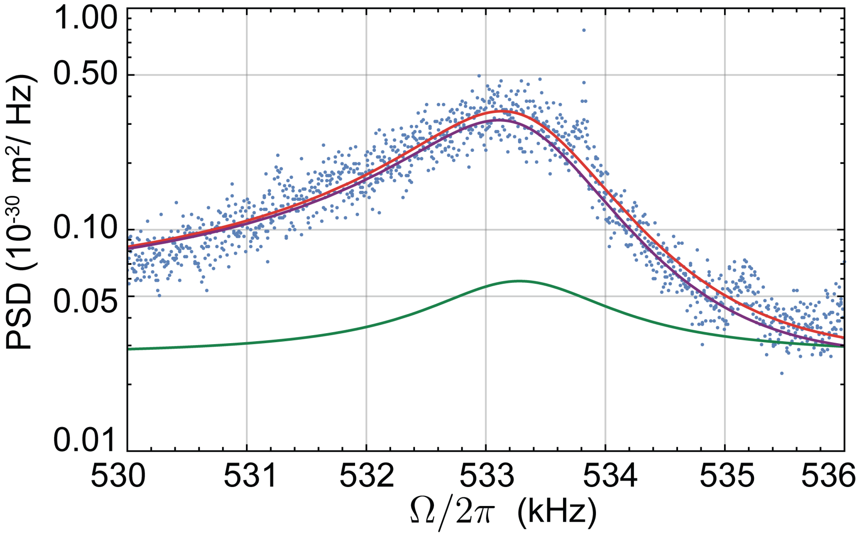

Figure 2.23: Example of spectrum, calibrated in $\mathrm{m}^2/\mathrm{Hz}$, acquired at 13 K around the mechanical mode $(0, 2)$. In the figure is shown the Fano profile due to the interaction of the mode shape and the background generated by the frequency noise. The Dark Green and the Purple line shows, respectively, the thermal and frequency noise contribution. The Red line shows the total fit and the Blue dots show the experimental data.

of the fast laser control. It is shown in Fig. 2.22b). The square of such response function has structures that closely resemble that of the cavity phase noise. This is an indication that the cavity phase noise is generated by multiple PZT resonances of the laser cavity. As shown in Fig. 2.22a) the frequency noise limits our sensitivity to the cavity length displacement (due to mechanical mechanical modes of the membrane), at the level between $10^{-33}$ and $10^{-35}$ $\mathrm{m}^2/\mathrm{Hz}$, while to observe quantum mechanical effects we require better sensitivity. Also, the laser frequency noise gives a limit in the laser cooling, in fact the frequency noise converted into amplitude noise in the cavity heats the oscillator, giving a limit in the optical cooling.

A typical spectrum with the unfiltered light at CT is shown in the Fig. 2.23. The mode $(0, 2)$ has an occupancy close to 4000, where in the some configuration of temperature (13 K) and optical cooling ($\Gamma_{eff} = 1.6$ kHz), but with the filtered light, the occupancy is close to $\sim 20$ phonons, according to the model. The data are fitted with a Fano and Lorentzian resonance. As it is clear in the figure, the Fano profile is dominant on the Lorentzian one. It is therefore clear that frequency noise defines a lower limit on occupancy. For all these reasons, we decided to build a filter cavity to decrease the laser frequency noise.

## Realization of the Filter cavity

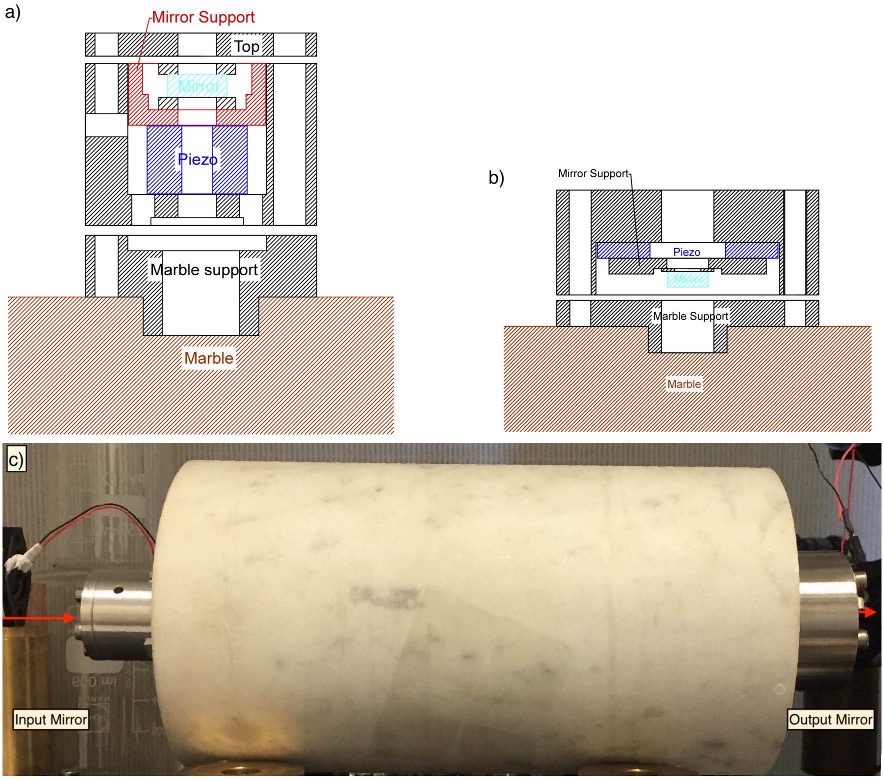

Figure 2.24: Panel a) and b): Section of the support used for the input-mirror and output-mirror respectively. Figure c): Photo of the filter cavity.

In this, and following, subsection I will describe all the filter cavity design, parameters and how it is implemented in our setup. The filter cavity has two identical mirrors with radius of 200 mm. The transmission coefficient of the mirrors is 130 ppm. The length of the cavity is 229 mm, given a free spectra range of 655 MHz, the linewidth of 30 kHz with a finesse equal to 21000. The cavity waist is $w = 0.184$ mm. The cavity spacer is a 11 cm diameter marble cylinder that allows good mechanical and thermal proprieties (thermal expansion coefficient $\sim 9.8 \times 10^{-6}$ m/°C). Both mirrors are connected to the marble spacer with appropriate mechanic supports, Fig. 2.24a) and 2.24b). The supports are designed to place, in contact with the mirror, a PZT used to tune and lock the cavity. The input mirror is in contact with a stack PZT allowing to tune by a complete $FSR$ using low voltage diver, and the output mirror is glued on a PZT plate, allowing a fast response on small range. The stack PZT allows to tune the cavity to the laser frequency and it acts on the low frequency range of the servo loop. The fast PZT is used to increase the lock bandwidth, if it is necessary in the lock. The mechanical mirror supports are used to align the cavity optical axis, since the parallelism between the surfaces of the marble cylinder is not good enough. We designed for both PZTs specific supports giving the possibility to tilt the mirrors, Fig. 2.24a) and 2.24b). With the screws of mechanical support, we can regulate the correct position and angle of the mirrors by compressing or relaxing o-rings placed between the marble spacer and mirror support. This alignment procedure has been realized in laminar flow hood. Successively we have placed the cavity on a vacuum chamber to keep the mirrors clean and to isolate the cavity from external effects. We, also, use a suspensions system, inside the chamber, to reduce the acoustic noise coming from the optic table. The chamber has a diameter of 40 cm and the height of the optical axis is 30.7 cm. A turbo pump keeps the system in vacuum at a pressured $10^{-5}$ mbar. In Fig. 2.24a) and 2.24b), are shown the sketches of the support system used for the input and output mirrors, respectively. The parameters of the stack PZT, used for the input mirror, are the following:

| | |
|---|---|
| model | PI/P-080.311 |
| operating voltage | $-20 \div 100$ V |
| displacement range | $5.5 \pm 20\%$ $\mu$m |
| capacity | 820 nF |

In our setup the filter lock is made by the fast laser control and the cavity slow PZT.

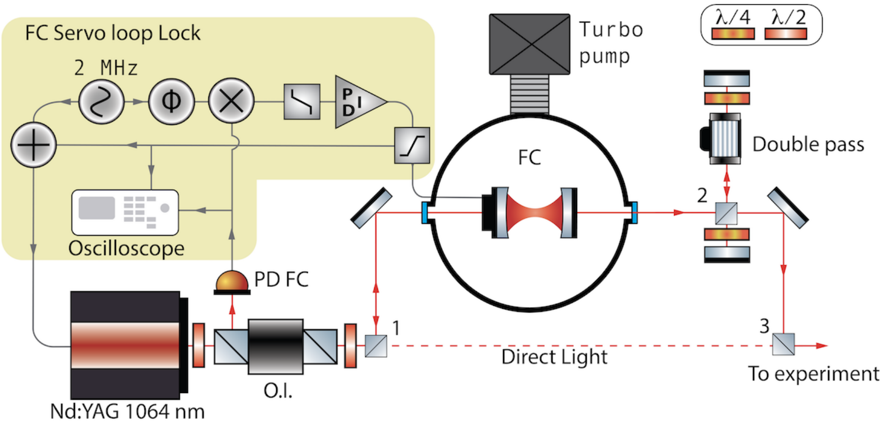

Figure 2.25: Experimental setup including the filter cavity and the servo loop scheme used for the cavity lock.

## Setup

Here we describe the optical setup used to exploit the filter cavity and the servo loop system used for the cavity lock. To introduce the filter cavity inside the apparatus, we have modified the original setup. In order to divert the beam toward the new path, we have used a polarizing beam splitter (PBS-1) situated after the optical isolator. We can regulate, with a half wave plate, the power transmitted and reflected by PBS-1, has shown in Fig. 2.25, allowing us to work with or without the filter light. The light reflected by the filter cavity is deviated by the input polarizer of the optical isolator and detected by the photodiode (PD FC). The transmitted light, is sent to PBS-2, where the beam, s-polarized, is reflected and sent to an AOM (used for in the double pass configuration for the lock scheme of the OMC). Finally the filter beam is converged on the optical path with a third PBS-3. The laser fast actuator is modulated at 2 MHz at the purpose to generate a phase modulation necessary for the PDH technique. The signal of the PD FC is mixed with a reference signal at 2 MHz with a proper phase to obtain the usual PDH shape. The reference and modulation signal are locked in phase. The demodulated signal is sent to a PID control used for the filter cavity lock. The PID output is sent to the cavity PZT for the slow lock corrections, and to the fast laser actuator for the fast corrections, where the cross over is accurately considered to watch the two actuators. The usual

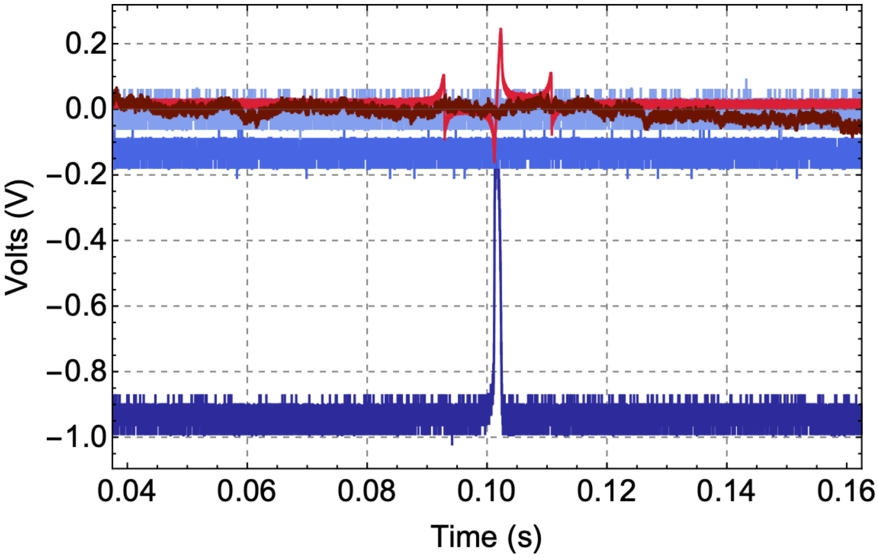

Figure 2.26: Filter cavity resonance peak shape dark blue. The blue signal shows the cavity lock at resonance and the heavenly is the photodiode dark signal. The red shape shows the PDH signal and the dark red the correction signal sent to the cavity actuators.

power injected in the filter cavity is close to 120 mW, the transmitted light is close to $\sim 70\%$ ($\sim 80$ mW), with a cavity matching $> 95\%$, (see Eq. 1.44), enough for our experiment. The usual PDH signal used has a peak-to-peak close to 400 mV$_{pp}$, an example is shown in Fig. 2.26. The PDH peak-to-peak, can be controlled (at fixed optical power) by the signal modulation depth mixed with the photodiode voltage output.

## Filtered Light

In Fig. 2.27 we report the spectra of the field reflected by the optomechanical cavity using both filtered and un-filtered light, taking care to send the same laser power to the homodyne detection. The spectrum of the filtered light (green spectrum) does not show any more the structure, due to the frequency noise. From the comparison of the spectra, we can conclude that the filter cavity is efficient in reducing the frequency noise. At low frequency due to the filter behavior, the filtered light spectrum is higher than the un-filtered one,

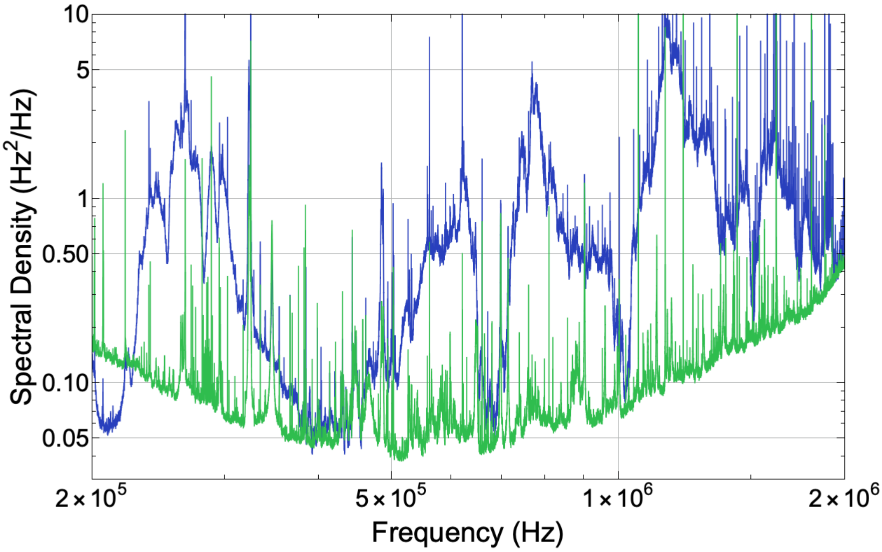

Figure 2.27: Spectra of the light reflected by the OM cavity taken using the PDH detection. Spectra are calibrated in terms of frequency displacement (Hz$^2$/Hz). Blue: direct light, green: filtered light. The structures due to the frequency noise are cutted by the filter cavity.

but this spectral area is out than the interested one. Between 200 kHz to 1 MHz, the spectrum level is below $10^{-1}$ Hz$^2$/Hz. It is possible to identify the minimum occupation with this frequency noise contribution. The equation is [6, 64]:

$$\bar{n}_{min} = \sqrt{\frac{\bar{n}_{th}\Gamma_m}{g_0^2} S_{\omega\omega}(\Omega_m)}. \tag{2.46}$$

The experimental parameters that will be used in this work are: temperature close to 7 K, vacuum optomechanical coupling $g_0/2\pi = 30$ Hz and $\Gamma_m/2\pi = 0.08$ Hz for the mechanical mode at 530 kHz with a quality factor close to $6.4 \times 10^6$. With these parameters the minimum occupation number is close to 2 phonons. In our experiment the residual frequency noise is not the main limit to bring the mechanical oscillator in the quantum regime. All the future optomechanical experiment will perform using the filter light.

### AOM phase noise characterization

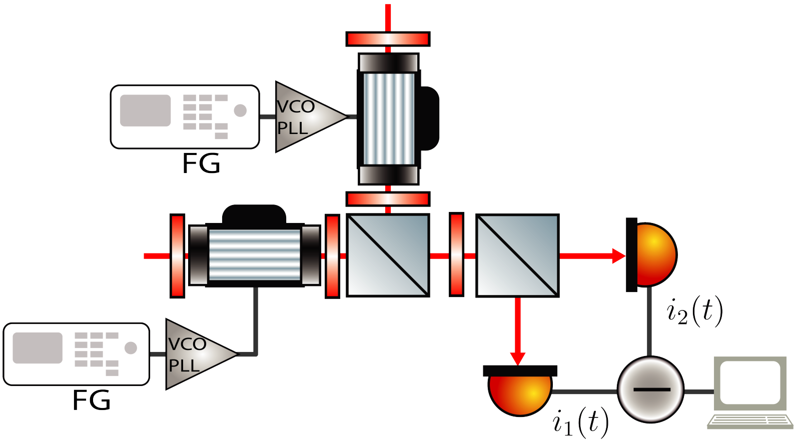

Figure 2.28: Apparatus used in the AOM's noise measurement, the two AOMs are driven by two different PLL and function generators.

Another possible noise source in our apparatus are the AOMs placed on the optical path, for the frequency control. The real noise source is the function generator used to drive the AOMs, therefore we examine all possible configurations, one pair at a time. To investigate that noise we observe the difference between two beams at the some optical power. The beams are driven with two identical AOM but two different function generators (FGs), locked in phase, and two different frequency multiplier (by a factor 40). The setup sketch is shown in Fig. 2.28.

This noise measurement is performed considering two fields described as $E_{1,2} = E_0 e^{i\phi_{1,2}(t)}$, where $E_0$ describes the field amplitude and $\phi_{1,2}(t)$ is the field phase. The detected signal goes as

$$\sim 2Re\{E_1^* E_2\} = 2|E_0|^2 \cos\left(\phi_1(t) - \phi_2(t)\right). \tag{2.47}$$

Now, we can write the phases as a slow and fast contribution $\phi_{1,2} = \phi_{1,2}^0 + \delta\phi_{1,2}(t)$. The signal become

$$2|E_0|^2 \cos\left(\Delta\phi_0 + \delta\phi(t)\right) \tag{2.48}$$

where $\Delta\phi_0 = \phi_1^0 - \phi_2^0$ and $\delta\phi(t) = \delta\phi_1(t) - \delta\phi_2(t)$. Considering that $\Delta\phi_0 \gg$

$\delta\phi(t)$, we can extend the previous equation

$$\sim 2|E_0|^2 \sin(\Delta\phi_0)\delta\phi(t). \tag{2.49}$$

The detect output signal goes as $V = A\sin(\Delta\phi_0)\delta\phi(t)$, where $A$ is the overall detection transfer function. The relative spectrum is

$$S_V = \frac{A^2}{2} S_{\delta\phi} \tag{2.50}$$

where $S_{\delta\phi} = S_{\delta\phi_1} + S_{\delta\phi_2}$, if the two signals are not correlated. The frequency noise is $S_\nu = (\ 2\pi\nu)^2 S_{\delta\phi}$. From the measurement of signal amplitude, $A$, we can calibrate the spectrum in terms of phase and frequency noise.

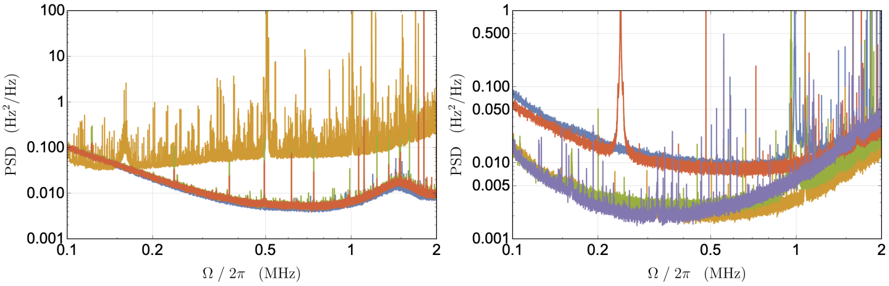

Figure 2.29: Left panel: Comparison of the spectra acquired with different FG, but identical PLL, driving the AOMs. Blue: AOMs driven by two Agilent (model 33210A) FG. Green: AOMs dived by two channels of the Zurich Lock-in Amplifier model FHF2LI. Red: like as the Blue spectrum with addition modulation at 4 kHz open (used for the Homodyne/Heterodyne phase look). Yellow: AOM1 driven by the Zurich and the AOM2 driven by Siglent FG (model SDG2122X) without passing by the PLL. Right panel: Comparison of the spectra acquired with all the possible AOM's PLL used in our apparatus. In all the configurations the PLL are driven by two Agilent FG (model 32210A). Each spectrum is acquired as is described in the text.

Operatively, we tested many different configuration of function generator, we used as FG two Agilent model 33210A, Zurich Amplifier model HF2LI Lock-in Amplifier and a Siglent model SDG2122X. Simultaneously we used four different PLL made by the Lens electronic workshop, they have different VCO models placed in their circuits. In that characterization the only FG that adds noise in the apparatus is the Siglent (yellow spectrum in Fig. 2.29, left panel), while the other two FGs add very low noise (blue and red spectra show in Fig. 2.29, left panel). The worst PLL gives the two spectra with higher level of frequency noise, red and blue in Fig. 2.29 right panel, we used two identical and phase-locked FG Agilent for both the PLLs used to drive the two AOMs. In our worst configuration the noise level is one order of magnitude below than 0.1 $\mathrm{Hz}^2/\mathrm{Hz}$ around the interesting frequencies from 200 kHz to 1 MHz. The noise introduced by the used function generators and PLLs is completely overwhelmed by the residual laser frequency noise of $\sim 0.1\ \mathrm{Hz}^2/\mathrm{Hz}$.

## 2.5 Balanced detection

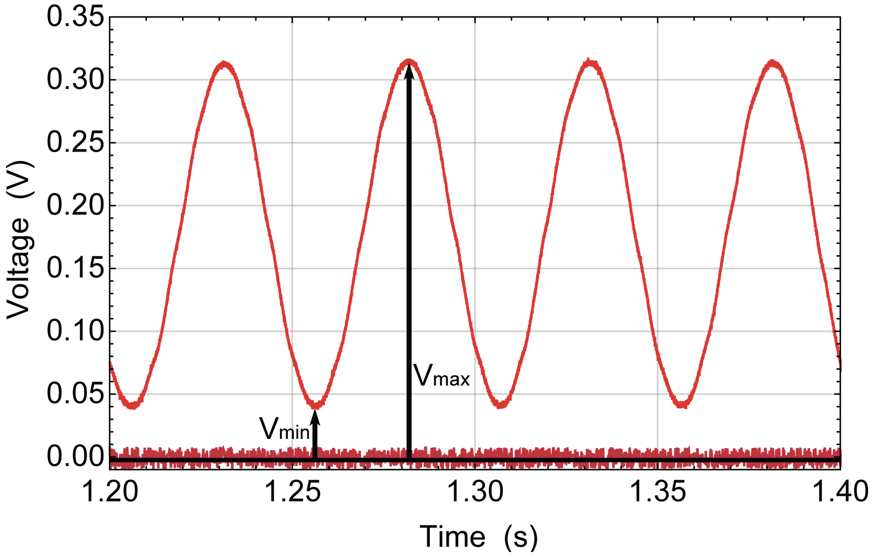

Figure 2.30: Heterodyne visibility, limited to $\sim$ 80% for visualization purposes. Light red line shows the interference signal, due to the difference frequency of the LO and signal beams, observed in one of the balanced hetero detection. The dark red points show the dark level of the detector, from where are measured $V_{max}$ and $V_{min}$, for the visibility measurement.

In our setup the mode matching of the signal and local oscillator can surpass 95%. The visibility is measured observing the DC signal in each heterodyne detector, where the two beam are injected on it with an identical power. Usually, the frequency shift between the LO and the probe beam is fixed at $\sim 20$ kHz. The visibility is measured using the equation:

$$\frac{V_{max} - V_{min}}{V_{max} + V_{min}} \tag{2.51}$$

where $V_{min}$ is the minimum voltage above the dark reference level, and $V_{max}$ is the maximum voltage value from the some level. An example of it is show in Fig. 2.30.

In the balanced detection the classical amplitude noise is strongly suppressed by the subtraction of the individual diode photocurrents. This is due to the noise correlation of the two outputs of the beam splitter. The rejection of the balanced heterodyne detection is measured using the laser relaxation peak at a frequency close to 800 kHz. At this purpose we exclude the laser noise eater, and we compare the sum (full classical laser noise) and difference (shot noise limited detection) of the two diode photocurrents. The suppression of the relaxation peak gives the rejection, a general value reached in our work is close to 44 dB, Fig. 2.31.

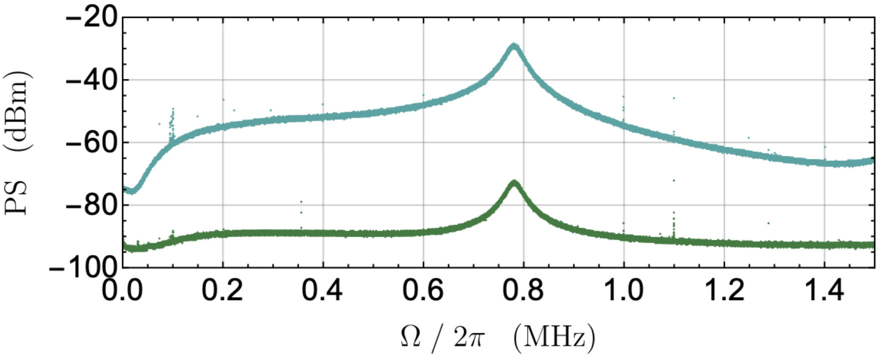

Figure 2.31: The cyan plot shows the sum photocurrent of the two detectors used in the heterodyne detection, while the dark green shows the photocurrent difference. The rejection is close to 44 dB. This is what we have in our detection apparatus.

### 2.5.1 Heterodyne detection

In this section we will discuss the heterodyne detection scheme following the reference [8]. The configuration used in our setup for the heterodyne and homodyne is shown in Fig. 2.32. The beam splitter has reflectivity and transmission coefficients equal to $|r|^2 = |t|^2 = 1/2$, $(r = it)$. The signal beam $\hat{a}_S$ (signal coming from the OMC) and the local oscillator $\hat{a}_{LO}$ are mixed in the beam splitter. We measure the current difference produced by the two fields $\hat{a}_1$ and $\hat{a}_2$ on the detectors, Fig. 2.32. We can suppose that the photocurrent produced in each detector is proportional to the incident flux $\hat{f}_{in} = \hat{a}^\dagger \hat{a}$:

$$\hat{i}(t) = C\hat{f}_{in} = C\hat{a}^\dagger \hat{a} \tag{2.52}$$

where $C$ is a constant. The subtraction of the two detectors current is:

$$\hat{i}_- = C(\hat{f}_1 - \hat{f}_2) = iC\left[\hat{a}^\dagger_{LO}(t)\hat{a}_S(t) - \hat{a}^\dagger_S(t)\hat{a}_{LO}(t)\right]. \tag{2.53}$$

The field fluctuations are related to the motion of the oscillator, in the power spectrum we can follow the oscillator evolution. In detail, we can write each

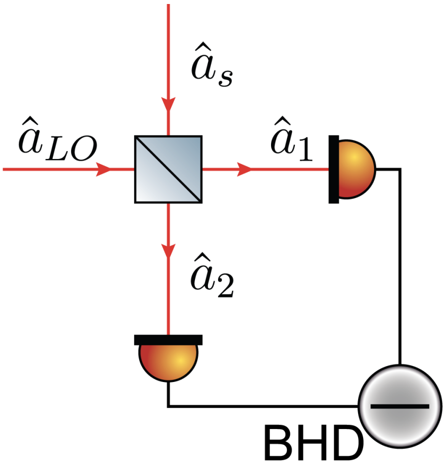

Figure 2.32: Heterodyne/Homodyne detection, the local oscillator $\hat{a}_{LO}$ bean is mixed with the signal beam $\hat{a}_S$ in a beam splitter. The Balance heterodyne/homodyne detection (BHD) is generated when on the diodes arrive an identical power on each one.

operator field in the rotating system respect to its central frequency:

$$\hat{a}_{LO}^{R}(t) = \hat{a}_{LO}(t)e^{i\omega_{LO}t} = \alpha_{LO} + \delta\hat{a}_{LO}(t), \tag{2.54}$$

$$\hat{a}_{S}^{R}(t) = \hat{a}_{S}(t)e^{i\omega_{S}t} = \alpha_{S} + \delta\hat{a}_{S}(t). \tag{2.55}$$

Where $\alpha_{LO} = |\alpha_{LO}|e^{i\theta_{LO}t}$ and $\alpha_S = |\alpha_S|e^{i\theta_S t}$ are respectively the mean value of the expectation value of the fields. The fluctuations around the rotating systems are $\delta\hat{a}_S(t)$ and $\delta\hat{a}_{LO}(t)$. From it the subtraction of the incident fluxes become:

$$\langle \hat{f}_1 - \hat{f}_2 \rangle = 2C|\alpha_{LO}^{*}\alpha_S| \cos\left(\theta + \frac{\pi}{2} + \Delta_{LO}t\right) \tag{2.56}$$

which $\theta = \theta_S - \theta_{LO}$ and $\Delta_{LO} = \omega_{LO} - \omega_S$. In the power spectrum the beating between the two signals is shown in the spectrum as a peak at the frequency $\Delta_{LO}$. We consider the local oscillator much more intense compared with the signal ($|\alpha_{LO}| \gg |\alpha_S|$). The equation of the current can be redefined by considering only the field first order fluctuations:

$$\hat{i}_{-} = C\delta(\hat{f}_1 - \hat{f}_2) = C|\alpha_{LO}|[\delta\hat{a}_S e^{i\phi} + \delta\hat{a}_S^{\dagger}e^{-i\phi}] \tag{2.57}$$

where $\phi = -\theta + \frac{\pi}{2} + \Delta_{LO}t$. The Power Spectrum Density (PSD) of the photocurrent is [13]:

$$S_{\hat{i}_-\hat{i}_-}^{het}(\omega) = \lim_{\tau\to\infty} \iint_{-\tau/2}^{\tau/2} dtdt' e^{i\omega(t-t')} \langle \hat{i}_-^{\dagger}(t)\hat{i}_-(t')\rangle. \tag{2.58}$$

Using the Eq. 2.57, where the current is a function of the detected fields, in the time domain the expectation value become:

$$\langle \hat{i}_-^{\dagger}(t)\hat{i}_-(t')\rangle = |\alpha_{LO}|^2 \Big[ \langle \delta a_S(t)^{\dagger}\delta a_S(t')\rangle e^{-i\Delta_{LO}(t-t')} + \langle \delta a_S(t)\delta a_S(t')^{\dagger}\rangle e^{i\Delta_{LO}(t-t')} \Big] \tag{2.59}$$

where we neglected the fast terms by using the rotating wave approximation. After the integration the Eq. 2.58 can be written in the follow way

$$S_{\hat{i}_-\hat{i}_-}^{het}(\omega) = |\alpha_{LO}|^2 \Big[ S_{\delta a_S \delta a_S}(\Delta_{LO} + \omega) + S_{\delta a_S^{\dagger}\delta a_S^{\dagger}}(\Delta_{LO} - \omega) \Big]. \tag{2.60}$$

The beating between the signal and the local oscillator fields allows to observe the frequency components $\Delta_{LO} \pm \omega$ into the power spectral density of the phonon number. Due to the non commutation between the annihilation and creation operators the power spectrum of the two operators are not symmetric $S^{het}_{\hat{i}_-\hat{i}_-}(\omega) \neq S^{het}_{\hat{i}_-\hat{i}_-}(-\omega)$. In the classical regime, on the contrary, the power spectrum for the operators become symmetric $S^{het}_{\hat{i}_-\hat{i}_-}(\omega) = S^{het}_{\hat{i}_-\hat{i}_-}(-\omega)$. The identical description can be used to describe the homodyne detection, we have just consider to resonant beams, $\Delta_{LO} = 0$. Like in the heterodyne detection, the information of the mechanical motion are in the phase fluctuations. In this detection the relative phase between the signal and the local oscillator field is fixed by using a phase lock scheme, at the propose to decrease all the additional fluctuations due to the apparatus.

## 2.6 Locking scheme

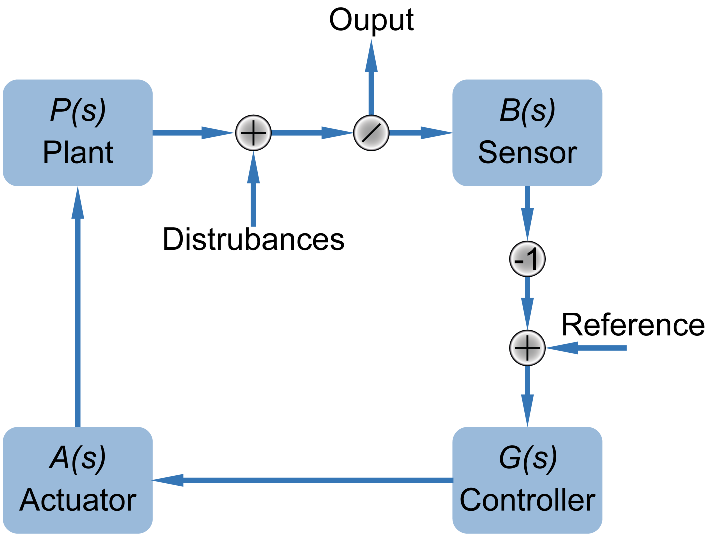

Figure 2.33: Basic scheme of the feedback control systems.

A crucial point of this thesis work is the stabilization of the laser frequency to an optical cavity resonance. On the cavity stability act many sources of noise such as thermal drifts, vibration of the ground floor, acoustic and more. For this reason is not trivial to have stable references. The that I will report description follow the books by Saulson [70] and Abramovici [2].

Here, I will describe a way to stabilize the system around its set point. We implemented this technique for all the cavities, filter and optomechanics. A general loop scheme is shown in Fig. 2.33. We used the some notations used in [2]. The first element is called plant $P(s)$. It is the system whose output parameter we want to control. With the loop open, the output is the sum of its free-running output and any disturbance (fluctuations, drifts). The second element is the sensor $B(s)$. This block is used to detect the plant's output (it gives some voltage signal). Usually, the signal produced by the sensor is linear with the plant output. The sensor signal is inverted and summed with a reference signal. This process produces, what is called error signal. The error signal is used to detect and correct the drifts from the reference. The next step in the loop is the controller $G(s)$, used to manipulate the error signal. For that are used proper filtering and amplification of the error signal. The last block is the actuator $A(s)$. It can effectively influence the plant output. When the sensor's signal is very close to the reference, the corrections of the error signal are very small, and the plant's signal is very close to the desired reference. However, if the output of the plant is far from the reference signal, due to the disturbance, an error signal proportional and inverted to the disturbance is produced to bring the output of plant close to the reference. Here, for simplicity we do not consider the additional noise sources and we do not consider the different unit of each component. The feedback control system is usually described by the Laplace transformations of the transfer functions of each loop component. Here we give only the final results of this description, following [2]. The transfer functions of each feedback component are $P(s)$, $B(s)$, $G(s)$, $A(s)$, where the complex Laplace coordinate $s = \sigma + i\omega$, while $\omega = 2\pi f$ is the angular frequency. The transfer functions provide an output signal, proportional to the input. For each frequency the open loop transfer function is:

$$L(s) = B(s)G(s)A(s)P(s). \tag{2.61}$$

This full response function amplifies the error signal within some bandwidth and low pass filter it to cut off the high frequency contribution, that can generate instability, by exciting the actuator resonances. The ratio between the sensor output voltage and the reference voltage gives what is called loop transfer function:

$$\frac{V_{sensor}(s)}{V_{reference}(s)} = \frac{L(s)}{1 + L(s)}. \tag{2.62}$$

If the open loop gain is $L(s) \gg 1$, the closed loop transfer function becomes unity. Indeed, when the controlled output of the plant follows the given reference, it is locked to a stable reference signal. Usually, in the optical experiments we are interested in controlling the length of a resonator or interferometer to match its frequency with respect to the input laser frequency, or vice versa. Following the lock scheme described before, the resonator or the interferometer are our plants. As sensor block we use a photodiode, that reads and converts the plant's signal into a voltage signal. The error signal is sent to a PID with proper gain and bandwidth, whose output signal is sent to the actuators. Usually we consider two different actuators: a slow actuator as the laser crystals temperature or cavity PZT (controlling the cavity length), to control the slow but large drift due to the temperature change in the laboratory, $BW < 5$ Hz. The fast actuator as the laser PZT (modifying the laser cavity length ,with a bandwidth close to 10 kHz) or a double pass AOM with a measured response function of 5.8 MHz/V. A very important element of the loop is the error signal. If we consider the cavity plant, the error signal is linear with the detuning between the laser and cavity resonance frequencies. It should have a characteristic sign flip to discriminate between lower or higher frequencies, while the dip signal of the cavity resonance does not give any information about the positive and negative detuning. The phase signal of the reflected beam from the cavity

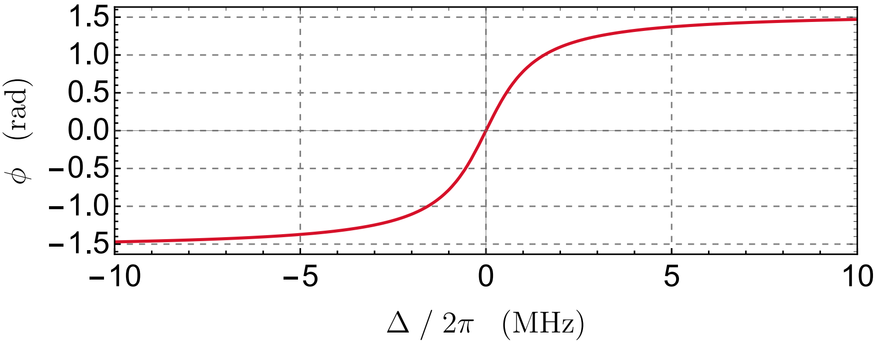

Figure 2.34: Phase response shape as a detuning $\Delta$ function, that signal is calculated follow the Eq. 2.63 where we using the OMC parameters. Where $\kappa_{ex}$ is calculated from the input mirror transitivity $T_1 = 315$ ppm and $\kappa/2\pi \approx 2$ MHz.

respects all these requests. It is given by the optical transfer function $\chi_{opt}$, Eq. 1.74:

$$\phi(\Delta) = arctan\left(\frac{\mathsf{Re}(\chi_{opt})}{\mathsf{Im}(\chi_{opt})}\right). \tag{2.63}$$

The phase signal is linear in the detuning $\Delta$ and, can it define a sign flip around the resonance $\Delta = 0$. Therefore, the measurement of the phase signal needs a stable reference and simultaneously, it is insensitive of the far modes, because at larger positive and negative detuning the phase signal is flat, approaching an arc-tangent.

In this work, the technique used for the filter and optomechanical cavity lock is the Pound-Drever-Hall (PDH). In the following section we will give the PDH theoretical description and, furthermore, its implementation in our setup. We used other locking techniques, such as the locking scheme for the laser at 980 nm used for the Q-factor measurement, or the phase locking scheme in the homodyne and heterodyne at low detection frequency.

## Pound-Drever-Hall Signal

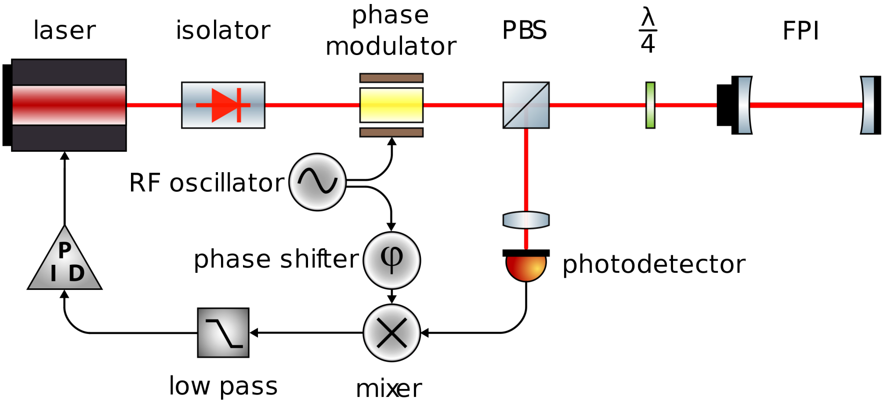

Figure 2.35: General optical e electronic Pound-Drever-Hall scheme

The Pound-Drever-Hall (PDH) technique [25,59] is a standard method to lock a laser frequency to the resonance of a Fabry-Pérot cavity, or vice versa. In order to control the difference between the laser wavelength and cavity resonance, a discriminating signal is required that changes as a function of the detuning, and that allows a linearly approximating dependency around the resonance. We can not use the intensity because it is an even function of the detuning. On the contrary the PDH techniques provides the design signal.

Now we consider a modulation on the electric field. We start from the incident field, $E_0 e^{i\omega_l t}$. The phase of the this field is modulated at the frequency $\Omega_s$ much smaller than the cavity $FSR$. In the frame rotating at angular frequency $\omega_l$ the input field is:

$$E_{in} = E_0 e^{i\omega_l t} e^{(i\beta \sin(\Omega_s t))} = E_0 e^{i\omega_l t} \sum_n J_n(\beta) e^{in\Omega_s t} \tag{2.64}$$

where $\beta$ is the modulation depth and we use the Jacobi-Anger expansion.

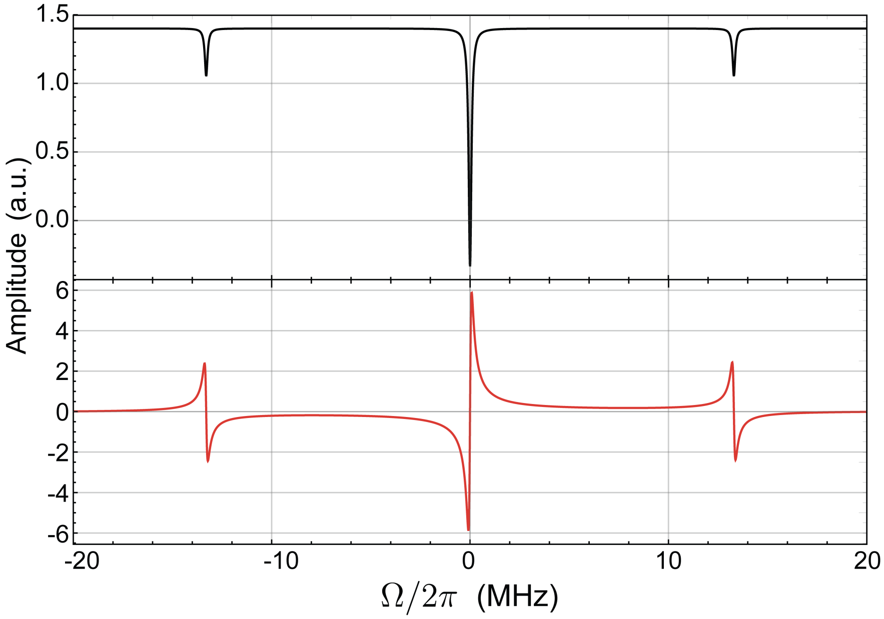

Figure 2.36: In the upper panel we show the calculated shape of $|H^r|^2$ with a modulation at 13.3 MHz, and in the lower panel we show the demodulated signal for $\beta \ll 1$.

The total field can be seen as composed of a carrier at angular frequency $\omega_l$, the series of sidebands at angular frequencies $\omega_l \pm n\Omega_s$. The power in the carrier is $P_c = J_0^2(\beta)P_0$, where $P_0$ is the total power. At the same time, the power in the sidebands is $P_s = J_n^2(\beta)P_0$. When the modulation depth is small ($\beta \ll 1$), most of the power is in the carrier and in the first order sidebands: $P_c + P_1 + P_{-1} \sim P_0$. The reflected field can be written as:

$$E_{ref} = E_0 \sum_n H_n J_n(\beta) e^{i(\omega_l + n\Omega_s)t} \tag{2.65}$$

where we have defined as $H_n := H^r(\Delta + n\Omega_s)$ the cavity field reflection function and $\Delta = \omega_l - \omega_{cav}$. The intensity impinging on the photodiode is given by the square modulus of the field, thus

$$I_{ref} \propto \sum_{n,m=-\infty}^{\infty} H_n H_m^* J_n(\beta) J_m(\beta) e^{i(n-m)\Omega_s t}. \tag{2.66}$$

This means that, in a detection at $\Omega_s$, we interested only in the terms for which $n = m \pm 1$. The signal at the low pass filter output depends on the phase difference between the photodiode response and the reference. If we write it as

$$V \propto \sum_n H_n J_n(\beta) [H_{n+1}^* J_{n+1}(\beta) e^{-i\Omega_s t} + H_{n-1}^* J_{n-1}(\beta) e^{i\Omega_s t}], \tag{2.67}$$

we can define

$$A = \sum_n H_n J_n(\beta) H_{n-1}^* J_{n-1}(\beta). \tag{2.68}$$

The voltage output becomes:

$$V \propto 2Re[A] \cos(\Omega_s t) + 2Im[A] \sin(\Omega_s t). \tag{2.69}$$

The photodiode signal enters the signal port in a mixer where a sinusoidal signal $\Omega_s$ is used as oscillator reference, with an appropriate phase. After the mixer, a low pass filter selects the component proportional to $\sin(\Omega_s t)$. The imaginary part of the voltage is called error function $\epsilon$. It is shown in Fig. 2.36, in the approximation $\beta \ll 1$. We now can rewrite the function A:

$$A = \sum_{n=0}^{\infty} J_n(\beta) J_{n+1}(\beta) (H_n^* H_{n+1} - H_{-(n+1)}^* H_{-n}). \tag{2.70}$$

We can now introduce the approximation $\Omega_s \gg \kappa$. In this case, the sidebands are totally reflected, $H^r(\Delta + n\Omega_s) \approx -1$. The Eq. 2.70 in this limits reduces to

$$A \approx J_0 J_1 (-2iIm[H_0(\Delta)] + H_0(\Delta - \Omega_s) - H_0^*(\Delta + \Omega_s)). \tag{2.71}$$

From this equation we can observe different regions. The first one is when $n = 0$ close to the resonance. The second one is at $\Delta = -\Omega_s$ and the third one at $\Delta = \Omega_s$. In our setup the modulation frequency is at 13.3 MHz, much larger than the cavity linewidth $\kappa \sim 2$ MHz. The modulation frequency is generated on the probe beam with a resonant EOM, Fig. 2.1. The modulation is also used to measure the cavity linewidth, the procedure is explained in Sec. 2.1.1.

The error function is the dispersive component of the cavity response. It has all the characteristics we were looking for: it is an odd function of the detuning and it also has a linear trend in the proximity by the resonance. This signal is used as an error signal for the cavity lock. Since the signal is quite linear, it is also used beyond the locking band, above the maximum correction frequency, in order to acquire the laser detuning fluctuations. The detuning is due to laser frequency fluctuation and to length variations of the cavity. We need, therefore, to consider the region close to the resonance, where the laser is locked. For $\Delta \ll 1$, we can write the reflection coefficient in terms of the small deviations is $\delta L$ the cavity length from resonance:

$$H^r(\delta L) \approx i\frac{4\mathcal{F}}{\lambda}\delta L \tag{2.72}$$

where $\mathcal{F}$ is the cavity finesse. The error function is:

$$\epsilon = -16\sqrt{P_c P_s}\frac{\mathcal{F}}{\lambda}\delta L. \tag{2.73}$$

We can write the error function as:

$$\epsilon \simeq -V_{pp}^{PDH}\frac{\Delta}{\kappa/2} \tag{2.74}$$

where $V_{pp}^{PDH}$ is the maximum peak-to-peak voltage measured while scanning the cavity length. In the setup we use this technique to lock the filter and the optomechanical cavity. The filter cavity lock uses the fast laser actuator, as the fast correction and a PZT on the input mirror for the slow correction of the thermal drift (Fig. 2.24a)). The lock to the OMC, exploits as fast actuator an AOM in double pass configuration with total gain $2 \times 5.8$ MHz/V. When we work with unfiltered light, during the laser noise characterization (see Sec. 2.4), the fast lock actuator is the laser fast control, the slow fluctuation are correct by a PZT glued on the OMC input mirror, as shown in Fig. 2.2.

Thanks to the correction signal, we can calibrate the spectra in $\mathrm{Hz}^2/\mathrm{Hz}$ or in $\mathrm{m}^2/\mathrm{Hz}$. As a reference we use a sinusoidal modulation at fixed frequency $f_{cal}$ sent to the fast control, placed inside the lock band. We typically acquire simultaneously the homodyne or heterodyne with the simultaneous error signal. From the ratio between the peaks at the calibration frequency in the two spectra, and from the laser response to fast control signal, we obtain the conversion factor from the voltage to the frequency, or length, displacement. From the frequency of the laser and the cavity length, we can finally obtain the spectral density of cavity. The calibrated power spectral density (PSD) of the cavity length is therefore:

$$S_{xx}(f) = \frac{S_{VV}^{err}(f_{cal})}{S_{VV}(f_{cal})} \left[ G_{fast} \frac{2\pi L_{cav}}{\omega_l} \right]^2 S_{VV}(f) \tag{2.75}$$

where $f_{cal}$ is the calibration frequency, $G_{fast}$ is the response to fast control, $L_{cav}$ is the length of the cavity, $\omega_l$ is the frequency of the laser, $S_{VV}(f)$ is the PSD of the PDH signal and $S_{VV}^{err}(f)$ is the PSD of the error signal, both in $\mathrm{V}^2/\mathrm{Hz}$, while $S_{xx}(f)$ is the PSD expressed in $\mathrm{m}^2/\mathrm{Hz}$.

## Homodyne/Heterodyne phase look

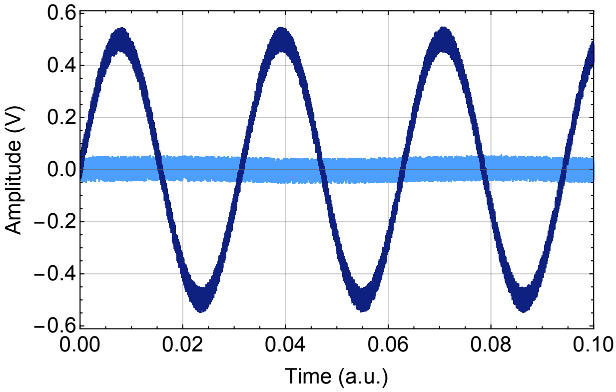

Figure 2.37: Homodyne stabilization example. Dark blue features the direct subtraction of the individual detectors and the light blue shows the phase homodyne stabilization, around the zero.

During the acquisitions a crucial point of the homodyne (heterodyne) detection is the phase stabilization. The used detectors split the slow DC output and the fast AC channel. The fringes due to the interference between probe and local oscillator beam are observed in the DC outputs of the two photodiodes (Fig. 2.37). In the homodyne detection the local oscillator is resonant with the probe beam. Meanwhile in the heterodyne detection the local oscillator is shifted by $\Delta_{LO} \ll \Omega_m$ from the cavity resonance. The lock scheme uses the AOM located on the local oscillator path (Fig. 2.1). At this propose we exploit the modulation function of the AOM's generator. As error signal we used the detectors DC difference signal, blue shape in Fig. 2.37, (for the heterodyne the DC signal is demodulated at $\Delta_{LO}/2\pi$). To lock in phase the homodyne and heterodyne detection, we select a proper depth of modulation in the generator. The lock bandwidth is given by the product between depth of modulation and the DC difference signal. The light blue shape in Fig. 2.37 shows an example of the error signal when the detection is locked.

# Chapter 3

# Investigation of the sidebands asymmetry

In this chapter we investigate the sideband asymmetry as an indicator of quantum behavior and how to control systematic effects, such as those due to a residual probe detuning. The optomechanical iteration generate spectral peaks at distances equal to the mechanical oscillator frequency $\Omega_m$ around the carrier frequency of the probe field. In the quantum theory, the sidebands amplitudes are different, as is explained in the Sec. 1.3. While such asymmetry can be explained in different ways [8, 41, 80], all interpretations recognize as a non-classical signature of oscillator motion [8]. A particularly clear explanation considered that the anti-Stokes (blue) sideband implies an energy transfer from the oscillator to the field (frequency up-conversion of photons), and vice versa for the Stokes (red) sideband. Since the quantum oscillator cannot yield energy when it is in the ground state, the anti-Stokes process is less favored (see also Sec. 1.3). The blue and red sideband strengths are proportional respectively to $\bar{n}$ and $\bar{n}+1$ [81], where $\bar{n}$ is the mean occupation number of the oscillator. Measurements of the asymmetry of sidebands in optical experiments have bean realized by alternatively placing the probe field at a detuning of $\pm\Omega_m$ around the cavity resonance [67] or in a single measurement from the spectral sidebands in the probe field [60, 73, 77]. The former technique is particularly useful in the regime of resolved sidebands ($\Omega_m \gg \kappa$, where $\kappa$ is the cavity linewidth), since for each position of the probe, the measured sideband is at the cavity resonance frequency and it is thus amplified. On the other hand the control of systematic effects can be an issue: the probe intensity and the detection efficiency must be equal for the two values of detuning, and the probe detuning itself must be very accurate, i.e. the system should remain stable between two separate measurement sessions. The latter technique, while extensively used in cavity optomechanics, requires an accurate control of the probe detuning, above all in the case of a narrow cavity resonance. The detuning is very important because the cavity works indeed as frequency filter for the output field, with an effect that differs between the two sidebands and can thus spoil the measurement of their ratio.

In the first Sec. 3.1, I will briefly recap some theoretical concept, following in Sec. 3.2, I will describe the specific apparatus parameters used in this work. Later (Sec. 3.3), I will describe the sidebands correction method, and in the last 3.4, I will describe the experimental results.

## 3.1 Theoretical background

The displacement spectrum of a mechanical oscillator is characterized by resonance peaks corresponding to the different normal modes. The area underlying each peak provides a measurement of the variance of the displacement to that mode and can be written as $\mathcal{A}_x = 2x^2_{ZPF}(\bar{n}+1/2)$, where $x_{ZPF} = \sqrt{\hbar/2m_{eff}\Omega_m}$ is the zero-point fluctuation (ZPF) amplitude and $m_{eff}$ is the mechanical mode effective mass. The mechanical oscillator is in equilibrium with a thermal bath at temperature $T_{bath}$; the mean thermal occupation number is $\bar{n}_{th} \backsimeq k_B T_{bath}/\hbar\Omega_m$, where $k_B$ is the Boltzmann constant. This expression is valid in the high temperature limit $\bar{n}_{th} \gg 1$. The mechanical peak linewidth is $\Gamma_m = \Omega_m/Q$, where $Q$ is the intrinsic mechanical quality factor. When placed in an optical cavity, the oscillator is thermalized toward the photon bath at negligible occupation number ("back-action cooling" [4,33]) by the optomechanical interaction, that changes the effective linewidth of the spectral peak by a factor $\Gamma_{opt}$ proportional to the intracavity optical power (optical spring). The effective linewidth is $\Gamma_{eff} = \Gamma_{opt} + \Gamma_m$, and the oscillator occupation number is thus reduced by a factor of $\Gamma_{eff}/\Gamma_m$. The back-action due to the optomechanical coupling introduce an additional fluctuating force, that can be seen as the effect of the quantum noise in the radiation pressure. Since such of quantum fluctuations are proportional to the laser power, and thus to $\Gamma_{opt}$, the originated displacement noise of the optically damped oscillator has negligible dependence on the cooling power, in the limit $\Gamma_{opt} \gg \Gamma_m$. In general, the quantum radiation pressure noise produced by an intracavity field at detuning $\Delta$ is proportional to $\bar{n}_{cav}^{max}\mathcal{L}(\Delta)[\mathcal{L}(\Delta+\Omega_m)+\mathcal{L}(\Delta-\Omega_m)]$ where $\bar{n}_{cav}^{max}$ is the average number of intracavity photons in case of resonant field, that is proportional to the input power. The readout of the oscillator motion is realized by an additional beam, called probe, resonant with the cavity. The reason for that is related to the strong shift from the cavity resonance of the cooling beam, to realize a efficient cooling ($\Delta_{cool}$). The drawback is its additional back-action, that increases the oscillator noise. The probe back-action force does not depend on the cooling power, and it has the same effect of an increased background temperature. The contribution of the back-action to the displacement spectra can be written in therms of an additional occupation number $\bar{n}_{BA}(\Delta)$ given by the sum of two contributions due to the cooling and probe beams $\bar{n}_{BA} = \bar{n}_{BA}^{cool} + \bar{n}_{BA}^{probe}$. The total effective occupation number is:

$$\bar{n} = \bar{n}_{th}\frac{\Gamma_m}{\Gamma_{eff}} + \bar{n}_{BA}^{cool} + \bar{n}_{BA}^{probe}. \tag{3.1}$$

A way to estimate the occupation number is the area×width product $\mathcal{A}\Gamma_{eff}$ of the spectral peak. In the classical limit, when the variance of the motion is still dominated by thermal noise, such product should remain constant as the cooling power is increased, given the value

$$\mathcal{A}_x \times \Gamma_{eff} \approx 2x_{ZPF}^2\bar{n}_{th}\Gamma_m = k_B T_{bath}/m_{eff}\Omega_m Q. \tag{3.2}$$

The quantum noise is instead at the origin of a linear increase of $\mathcal{A}\Gamma_{eff}$ versus $\Gamma_{eff}$. The peak area×width product in the frequency spectrum is:

$$\mathcal{A}\Gamma_{eff} = 2g_0^2\Gamma_m\left[\bar{n}_{th} + \left(\bar{n}_{BA}^{probe} + \bar{n}_{BA}^{cool} + \frac{1}{2}\right)\frac{\Gamma_{eff}}{\Gamma_m}\right] \tag{3.3}$$

where the vacuum optomechanical coupling strength is $g_0 = Gx_{ZPF}$. The therm into square brackets, is the ratio between the slope and the intercept in the $\mathcal{A}\Gamma_{eff}$ versus $\Gamma_{eff}$ line. It is linked to the properties of the oscillator quantum state. It is useful to verify the absence of unmodeled extra noise, evaluate $\bar{n}_{th}$, and the oscillator temperature $T_{bath}$. The heterodyne spectra of the field reflected by the cavity is a more accurate method to measure of the oscillator occupation number. It is possible to distinguish the two sidebands produced by the Stokes and anti-Stokes processes in the optomechanical interaction. If a resonant beam is used to readout, the sidebands peaks have areas proportional respectively to $\bar{n}$ (anti-Stokes) and $\bar{n}+1$ (Stokes), therefore $\bar{n}$ is directly calculated from the Stokes to anti-Stokes sideband areas ratio $R$ as $\bar{n} = 1/(R-1)$. This method does not require a calibration of the measured spectra in terms of oscillator displacement or frequency fluctuations, and also it is barely sensitive to spurious extra-noise. However, the residual probe detuning respect to the cavity resonance (in the studied system, the $\Omega_m < \kappa$, it is between the two regimes, resolved sidebands and bad cavity) is a potential problem. The two motional sidebands are indeed filtered by the cavity, $\mathcal{L}(\Delta_{probe} \pm \Omega_m)$, and such filter effect modifies $R$ as soon as $\Delta_{probe} \neq 0$, thus spoiling the validity of the measurement. In the following we describe a method to control the residual probe detuning and to correct the measured $R$.

## 3.2 Experimental Setup

The experimental setup is similar the one in Ch. 2. A circular SiN membrane with a thickness of 100 nm is placed in a Fabry-Perot cavity of length 4.38 mm at 2 mm from the cavity flat end mirror in a "membrane-in-the-middle" setup. The cavity finesse and linewidth are respectively 24500 and $\kappa/2\pi = 1.4$ MHz, measured at cryogenic temperatures ($\sim 7$ K). The physical reason of the finesse value, higher than the empty cavity finesse, is explained in the Sec. 2.1.1. As described in Sec. 2.1.1, the membrane has many resonance frequency, $f_{mn} = f_0\ \alpha_{mn}$. The cavity optical axis is displaced from the center of the membrane by $\sim 0.28$ mm, with an angle $\theta \simeq 0$. As a consequence, the optomechanical coupling and readout are much more efficient for one of the modes in each quasi-degenerate couple (with the shape $\propto \cos(m\theta)$), that we identify as "light twin", with respect to the other one ("heavy twin"). The mechanical mode $(1,1)$ at 370 kHz, having a quality factor of $8.5 \times 10^6$ at cryogenic temperature, which leads to an intrinsic width $\Gamma_m/2\pi = 40$ mHz. The optomechanical cavity is cooled down to 7 K in a helium flux cryostat. The optical path is composed of three beams, the frequencies of which are controlled by means of AOMs, (see Ch. 2). The Probe beam is kept resonant with the optomechanical cavity, its power is 20 $\mu$W. The cooling beam (Pump beam in the Ch. 2), orthogonally polarized with respect to the Probe, is also sent to the cavity and red detuned by roughly half linewidth ($\Delta_{cool}/2\pi = -700$ kHz). The detuning $\Delta_{cool}$ is fixed by the frequency difference of the

AOMs placed in the Probe and Pump paths. The cooling beam power is increased by steps up to 45 $\mu$W. The LO beam can be frequency shifted respect to the probe beam by $\Delta_{LO}/2\pi \sim 9$ kHz, allowing a low-frequency heterodyne detection or phase-locked to the probe for a homodyne detection of its phase quadrature. The power on each photodiode of the balanced detection is around 2 mW. The first scheme (heterodyne) is useful to separate the motional sidebands generated around the optical frequency of the Probe field, at frequency shifts corresponding to the mechanical modes frequencies. More in detail, the two motional sidebands appear around the mechanical frequencies shifted by the $\Delta_{LO}$: the Stokes at $\Omega_m + \Delta_{LO}$ and the anti-Stokes at $\Omega_m - \Delta_{LO}$, respectively, with $\Omega_m \gg \Delta_{LO}$, (see App. C). The spectra acquired with the homodyne scheme are calibrated in terms of cavity frequency fluctuations using a calibration tone in the Probe field, and they are used to measure the variance of the motion of the different membrane normal modes.

## 3.3 Calibration Method

As mentioned before the two motional sidebands are indeed filtered by the cavity according to

$$\frac{\kappa^2/4}{\kappa^2/4 + (\Omega + \Delta_{probe})^2} \tag{3.4}$$

where the $\Omega$ is the frequency, $\kappa$ is the cavity linewidth and $\Delta_{probe} = \omega_l - \omega_{cav}$. For a correct evaluation of $\bar{n}$ one must consider the filtering effect of the cavity, and in particular evaluate the residual probe detuning. This filtering effect indeed modifies the ratio between the two vibrational sidebands, $R = (\bar{n} + 1)/\bar{n}$, as soon as $\Delta_{probe} \neq 0$. In order to evaluate this effect we exploit the motional sidebands of the “heavy twin” modes that, being weakly coupled to the optical field, maintain a high occupation number so that their asymmetry can be completely attributed to the cavity filtering. Operatively, from the heterodyne measurement, we simultaneously measure the sideband ratio $R_{light}$ for both the ”light twin” mode, and the ”heavy twin” mode, $R_{heavy}$ (see App. B for details on the analysis). The ”light twin” mode is the $(1, 1)$ around 370 kHz. The measured asymmetry on the ”heavy twin” modes is fitted with the equation:

$$R_{hight} = \frac{\kappa^2/4 + (\Omega_m + \Delta_{probe})^2}{\kappa^2/4 + (\Omega_m - \Delta_{probe})^2}. \tag{3.5}$$

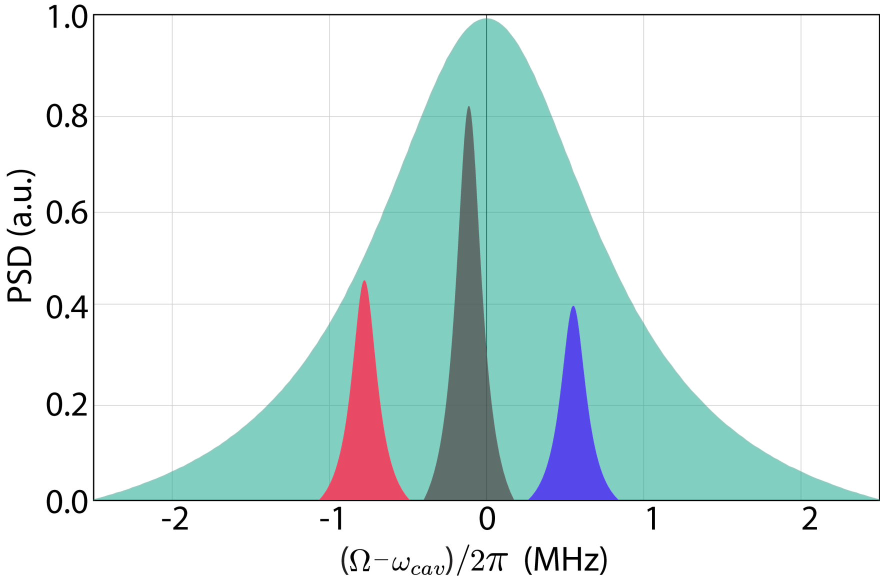

Figure 3.1: Cavity field distribution around the resonance (aquamarine). It shows how the field in the cavity is attenuated far from the cavity resonance. Where the gray Lorentzian shape shows the probe beam in the cavity detuned by $\Delta_{probe}$. The red and blue shapes show respectively, the Stokes and anti-Stokes sidebands in the cavity, around the probe beam at $\pm\Omega_m$.

From which we extract identify the probe detuning $\Delta_{probe}$ in each measurement. The cavity linewidth $\kappa$ and "heavy twin" mode frequency $\Omega_m$ are fixed. We then study how the asymmetry changes as a function of the optical power of the cooling beam. For each power 10 consecutive, 10 s long time intervals are acquired. From each interval the probe detuning is measured: its trend during the acquisition is showed in the inset of Fig. 3.2. The evolution the detuning (orange close circles in the inset) is fitted by a polynomial function to correct the asymmetry of the "light twin" mode. The sidebands ratio become: $R_0 = R_{light}/R_{heavy}$, from which the mean occupation number $\bar{n}$ is estimated. This procedure also allows us to monitor the stability of the detuning during the measurement, as shown in the inset of Fig. 3.2. Typical detuning values are $|\Delta_{probe}|/2\pi < 30$ kHz (corresponding to $0.02\kappa$) and the variations during a complete measurement are three times smaller. The consequent corrections to $R_{light}$ arrive to nearly 10%. A preliminary evaluation of the sideband ratio for the weakly coupled modes is indeed a good method to adjust the probe detuning at the beginning of the measurement. The corrections to $R_{light}$ obtained with this procedure are in good agreement with the method using directly the “heavy twin” mode. This correction method is used on all the data shown in this work.

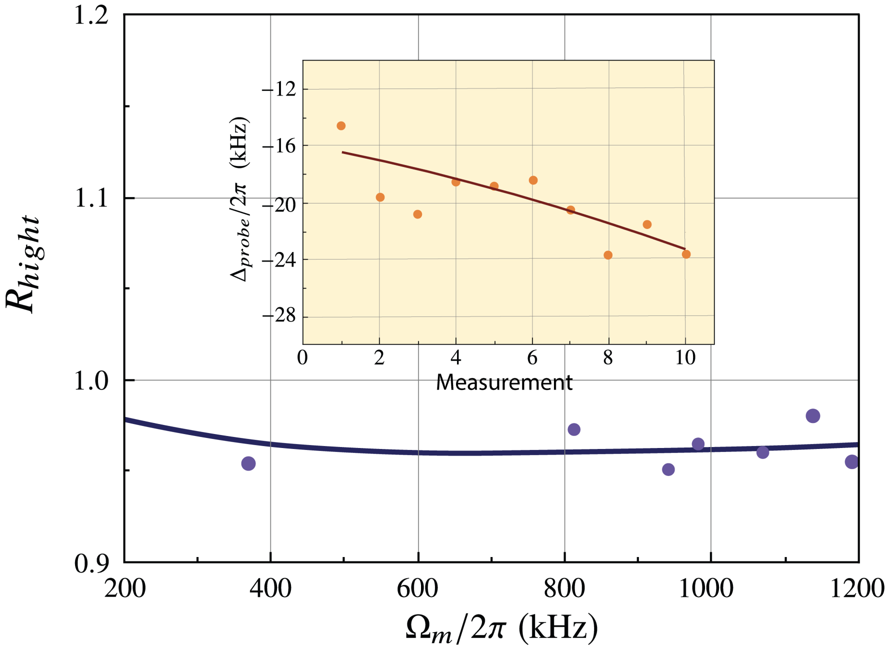

Figure 3.2: Method for correcting the sideband asymmetry due to the residual probe detuning. The measured sideband ratio for several weakly coupled modes is plotted as a function of the respective resonance frequencies $\Omega_m$ (blue dots), and fitted with the Eq. 3.5 to infer the probe detuning $\Delta_{probe}$ (solid line). This procedure is repeated for several consecutive, 10 s long time intervals. The evolution of the inferred values of the detuning (shown with orange close circles in the inset) is fitted with a first or second order polynomial function (solid line in the inset).

## 3.4 Homodyne and Heterodyne detection

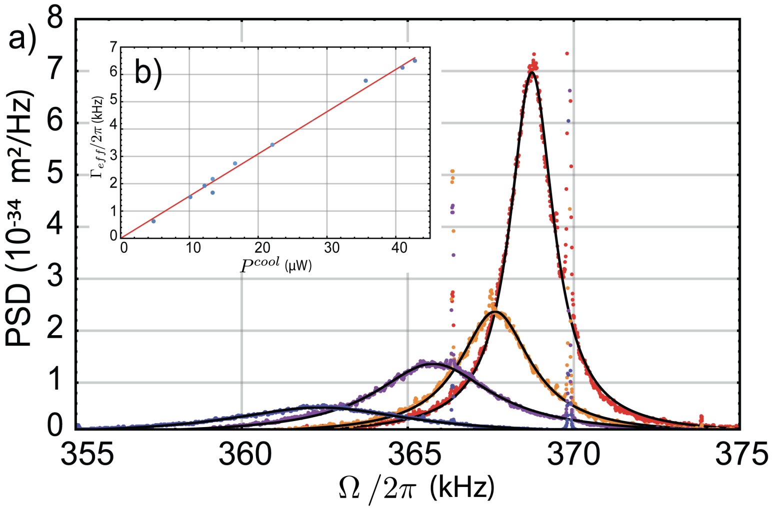

Figure 3.3: In the figure a), calibrated homodyne spectra around the frequency of the $(1,1)$ mechanical modes as the cooling power is increased up to $\sim 45$ $\mu$W, maintaining a detuning of $\Delta_{cool} \simeq \kappa/2$. A spurious electronic peak is shown with light gray symbols. The figure b) shows the measured peak width $\Gamma_{eff}/2\pi$ as a function of the cooling power, together with a linear fit.

In this section we will compare the results of the two different detection methods (heterodyne and homodyne). We focus on the membrane mode $(1,1)$ at 370 kHz. It is a quasi degenerate mode. The difference between the nearly degenerative "light twin" and the "heavy twin" adds lies in the position of the cavity waist compared to the membrane center more detail about it in the Sec. 2.1.1. The measurement are taken at different optical power of the cooling beam, keeping constant the probe power. The cooling effect is shown in the Fig. 3.3a). Due to so-called optical spring effect the mode is characterized by an increasing of $\Gamma_{eff}$ and a simultaneous red-shift of the mechanical resonance frequency with the power of the cooling beam. On the other hand, the "heavy twin" mode is weakly coupled to the radiation, since the optical spot is close to its nodal axis. Therefore the associated spectral peak at 370 kHz shows negligible optomechanical effects. An indicator of

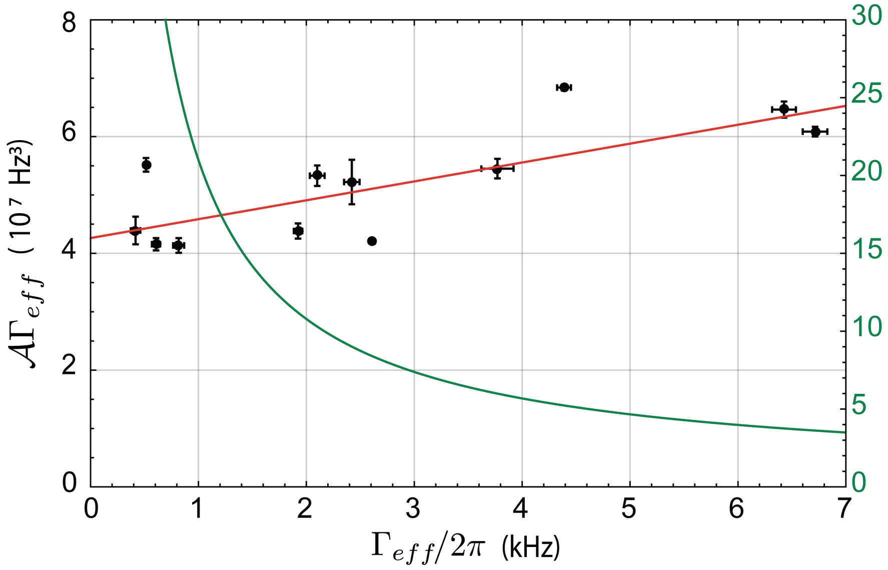

Figure 3.4: Increment of the measured area and width product for the strongly coupled $(1,1)$ mode, as a function of its width $\Gamma_{eff}/2\pi$. The red straight line reports the prediction of Eq. 3.3, where just an overall scaling factor is fitted to the data. A solid green line shows the mean occupation number $\bar{n}$ calculated according to Eq. 3.1.

the reduction of the phonon occupancy $\bar{n}$ in the "light twin" mode is the decreasing peak area. An independent measurement of the single photon optomechanical coupling $g_0$ could be done from a quantitative evaluation of $\bar{n}$ obtained from the area peak. On the other hand, the cooling factor $\Gamma_{eff}/\Gamma_m$ can be accurately measured. It provides a good estimate of the oscillator effective temperature and its occupation number $\bar{n} \approx \bar{n}_{th}\ \Gamma_m/\Gamma_{eff}$. It is valid in the classical limit, when the back-action contribution is negligible, and in absence of extra noise. The information of the area and the effective linewidth can be usefully put together in the area and width product ($\mathcal{A}\Gamma_{eff}$). The product is shown in the Fig. 3.4, as a function of $\Gamma_{eff}$. The reported value of $\mathcal{A}\Gamma_{eff}$ and $\Gamma_{eff}$ are obtained form fits of the spectral peaks with a Lorentzian function:

$$H(\omega) = \mathcal{A}\frac{\Gamma_{eff}/2}{(\Gamma_{eff}/2)^2 + (\omega - \Omega_m)^2} \tag{3.6}$$

where $\mathcal{A}$ is the peak area. From the theoretical prediction the $\mathcal{A}\Gamma_{eff}$ vs $\Gamma_{eff}$ should be linear where the slope-to-offset ratio is determined by the different contributions to $\bar{n}$. The three contributions are calculated from independent measurements, as follows. $\bar{n}_{th}$ is calculated from the bath temperature measured by a silicon diode sensor fixed on the cavity, and the oscillator frequency. The back-action occupancy, originating from the contributions of the Probe and Pump beam, can be written as

$$\bar{n}_{BA} = \frac{A^+}{A^- - A^+} \tag{3.7}$$

where [6]:

$$A^+ = g_0^2 n_{tot}\left(\tfrac{n_{probe}}{n_{tot}}\mathcal{L}(\Delta_{probe})\mathcal{L}(\Delta_{probe}-\Omega_m) + \tfrac{n_{cool}}{n_{tot}}\mathcal{L}(\Delta_{cool})\mathcal{L}(\Delta_{cool}-\Omega_m)\right), \tag{3.8}$$

$$A^- = g_0^2 n_{tot}\left(\tfrac{n_{probe}}{n_{tot}}\mathcal{L}(\Delta_{probe})\mathcal{L}(\Delta_{probe}+\Omega_m) + \tfrac{n_{cool}}{n_{tot}}\mathcal{L}(\Delta_{cool})\mathcal{L}(\Delta_{cool}+\Omega_m)\right). \tag{3.9}$$

$A^+$ is the upward transitions in the mechanical oscillator (Stokes process), and $A^-$ is the downward transitions in the mechanical oscillator (anti-Stokes process), where $n_{probe,cool} = P_{probe,cool}/\hbar\omega_l$ shows the photon number injected in the cavity for, respectively, probe and cool beam, while the total photon number is $n_{tot} = P_{tot}/\hbar\omega_l$, where $P_{tot} = P_{probe} + P_{cool}$, and the Lorentzian function is $\mathcal{L}(\omega) = 1/[(\kappa/2)^2 + (\omega)^2]$. The general back-action occupancy for a single beam is calculated from the Eq. 3.7 [6, 49]:

$$\bar{n}_{BA}^{cool} = \left[\frac{\mathcal{L}(\Delta+\Omega_m)}{\mathcal{L}(\Delta-\Omega_m)} - 1\right]^{-1}. \tag{3.10}$$

The back-action of the probe beam ($\bar{n}_{BA}^{probe}$) is calculated assuming a $\Delta_{probe} \simeq 0$. This assumption is confirmed by the linear dependence between $P^{cool}$ and $\Gamma_{eff}$ (see Fig. 3.3b)). $\Gamma_m$ is estimated from ring-down measurements as shown in Sec. 2.2. The experimental measurements well follow the predicted slope (solid line in Fig. 3.4), where just an overall vertical scaling factor is fitted to the data. The error bars refers to the standard deviation of measurements performed on 10 consecutive acquisitions. The scattering of data shows that long-therm fluctuations in the system parameter dominate over the statistical uncertainties, that are therefore not considered as meaningful in the following analysis. The solid green line in Fig. 3.4 shows the behavior of $\bar{n}$ calculated from Eq. 3.1. The agreement between the prediction of Eq. 3.3 and the experimental data suggest that the system is well modeled and in absence of additional noise. We achieve a minimum occupancy is $\bar{n} = 3.9$ at the maximum power of the cooling beam. According with the Eq. 3.3 the fit gives a value of the vacuum optomechanical coupling strength equal to $g_0/2\pi = 31 \pm 1$ Hz.

The qualitative agreement is not yet a safe guarantee of an accurate measurement. The membrane oscillator can be heated due to laser absorption yielding a linear increase of the $T_{bath}$ with $P_{cool}$, and thus a larger slope of $\mathcal{A}\Gamma_{eff}$ vs $\Gamma_{eff}$. In the fit of $\mathcal{A}\Gamma_{eff}$ vs $\Gamma_{eff}$ the slope and offset are free parameters. We observe for the ratio between the slope and offset the value of $(8.0 \pm 2.5) \times 10^{-5}$ Hz$^{-1}$. To be compared with the theoretical value calculated from Eq. 3.3 of $4.9 \times 10^{-5}$ Hz$^{-1}$. This suggests that the sample temperature could have increased by $1.8 \pm 1.5$ K at our maximum cooling power. Furthermore, additional amplitude or frequency noise in the laser field would instead provide a quadratic term in $\mathcal{A}\Gamma_{eff}$ vs $\Gamma_{eff}$. Indeed we added such term to the fit of the data, finding a maximum contribution of $13 \pm 10$ % to the measured $\mathcal{A}$. In both fitting procedures the uncertainty is due to the scattering of the experimental data, and the results are compatible with null effects of heating and extra laser noise. The analysis of the homodyne spectra gives a reliable estimate of $\bar{n}$ at increasing cooling power. However, the measurement accuracy is reduced due to an uncertainties in additional noise.

Therefore a better procedure to estimate the phonon occupancy is the motional sidebands ratio in the heterodyne spectra. Indeed, it gives directly access to the real average phonon occupation number for each value of cooling power, including implicitly extra heating and noise, without the necessity of further independent measurements of system parameters. Our apparatus can easily switch from homodyne to heterodyne detection, adding a frequency offset $\Delta_{LO}$ in the phase locking of the local oscillator. Two examples of the heterodyne detection are shown in the Fig. 3.5 at two different optical power of the cooling beam. Here $\Delta_{LO} \ll \Omega_m$ and the two sidebands are close to the mechanical resonance of the mode $(1,1)$. In the Fig. 3.5b), at low power of the cooling beam, the sidebands are almost equal. When the cooling beam power is higher (Fig.3.5a)), the asymmetry between the two sidebands is clear, with the left sideband (anti-Stokes), is much lower

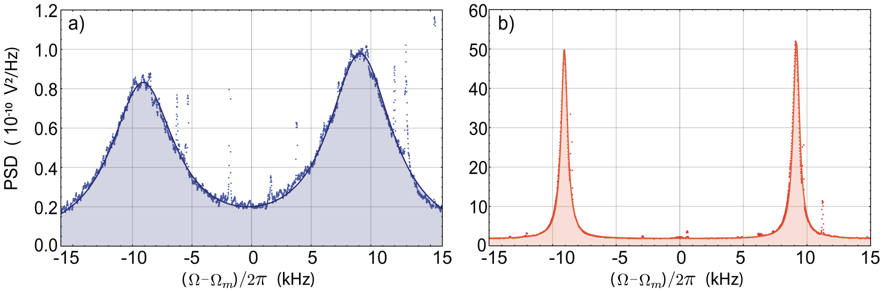

Figure 3.5: Observation of the Stokes (right) and anti-Stokes (left) spectral peaks of the $(1, 1)$ membrane mode for two different values of the cooling power: a) at larger cooling power, the mean phonon occupancy is $3.87 \pm 0.21$. b) at low cooling power, the mean phonon occupancy is $17.1 \pm 3.4$. Symbols show the experimental data, including the narrow peaks of the "heavy twin" mode and spurious electronic peaks shown in light gray. Solid lines are the fitting functions Eq. 3.11, the background is subtracted from the displayed data for the sake of clarity. The fitted mean resonance frequency is taken as origin of the displayed horizontal axis.

than the right one (Stokes). As described before, for a correct evaluation of $\bar{n}$ is crucial to estimation well the filtering effect of the cavity due to residual probe detuning. The data are analyzed with the following fitting function composed of two Lorentzian peaks of equal width and shifted by $2\Delta_{LO}/2\pi = 18$ kHz:

$$S(\omega) = \frac{2}{\pi}\left[\frac{\mathcal{A}_{AS}\,\Gamma_{eff}}{\Gamma_{eff}^2+4(\omega-\Omega_m-\Delta_{LO})^2} + \frac{\mathcal{A}_{S}\,\Gamma_{eff}}{\Gamma_{eff}^2+4(\omega-\Omega_m+\Delta_{LO})^2}\right] \tag{3.11}$$

where $\mathcal{A}_{AS}$ and $\mathcal{A}_S$ are respectively the area of the anti-Stokes and Stokes sidebands. The ratio between the "light twin" modes are calculated as $R_{light} = \mathcal{A}_S/\mathcal{A}_{AS}$. The corrected ratio value, $R_0 = R_{light}/R_{heavy}$, gives the correct value of $\bar{n}$. At low cooling power the spectral width $\Gamma_{eff}$ is still relatively small and the sideband asymmetry is just $R_0 \simeq 1.048$, yielding an inferred mean phonon occupancy of $17.1 \pm 3.4$, Fig. 3.5b). At larger cooling power, producing broader peaks, the asymmetry is more evident, with a measured value of $R_0 \simeq 1.24$ and a mean phonon occupancy of $3.87 \pm 0.21$ (Fig. 3.5a)). The error bars refer to the standard deviation relative to 10 consecutive 10 s-long acquisitions. Fig. 3.6 shows the occupation number $\bar{n}$ from the corrected sideband ratio as a function of $\Gamma_{eff}$, obtained at increasing values of cooling power. The filled curves reflect the expected $\bar{n}$ and its different contributions. They are calculated from Eqs. 3.7 and 3.1. The cooling back-action contribution is constant with the power, and equal to $\bar{n}_{BA}^{cool} \sim 0.58$ for the $(1,1)$ modes. It follows from Eq. 3.10, where we used its detuning $\Delta_{cool}$. The probe back-action occupancy is calculated from Eq. 3.7, where the contribution of cooling beam is not considered. We are here

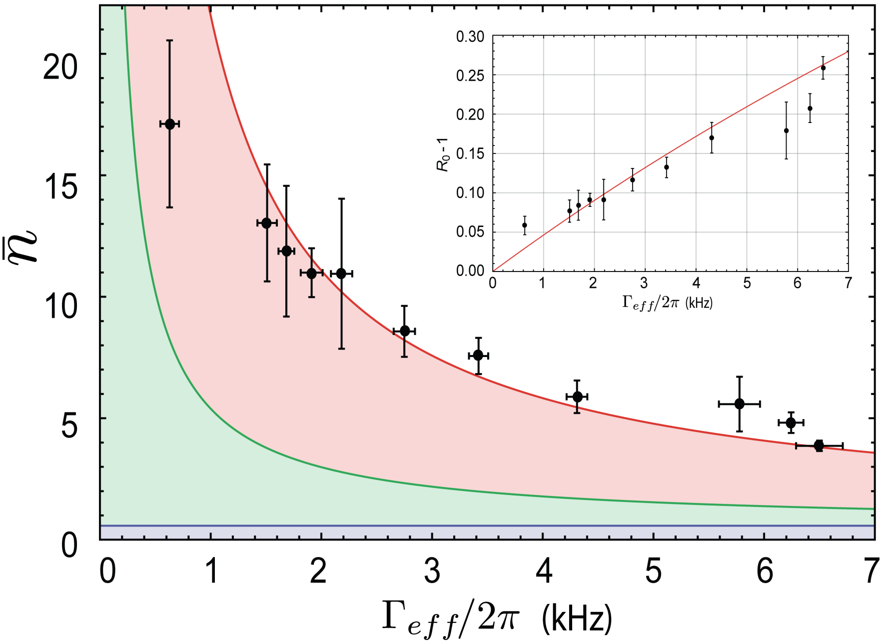

Figure 3.6: Close symbols report the occupation number $\bar{n}$ calculated from the corrected values $R$ of the sideband ratio for the "light twin" mode, according to $\bar{n} = 1/(R-1)$. The red solid curve represents the occupation number $\bar{n}$ calculated according to Eq. 3.1 using independently measured parameters. Red, green and blue areas represent respectively the contributions of the thermal noise, the probe beam back-action, and the cooling beam back-action.

in weakly resolved sidebands regime and back-action cooling can in principle bring these modes to an occupation number below unity, close to $\bar{n}_{BA}$ in the weak coupling regime. Here the theoretical curves have no free fitting parameters: all the contributions to $\bar{n}$ are calculated on the basis of independent measurements. The agreement between the theoretical description and the experimental data is excellent, considering the experimental statistical uncertainty, suggesting the absence of non-modeled extra noise. The data can be used to extract the bath temperature $T_{bath}$. Leaving $\bar{n}_{th}$ as a free parameter of the fit in Eq. 3.1. The extracted value is $6.7 \pm 0.6$ K, compatible with the 7.2 K measured by the sensor.

# Chapter 4

# Quantum Signature of a Squeezed Mechanical Oscillator

In this chapter we will discus experimental results concerning the propose of motional sidebands in the presence of parametric squeezing. We will see that the sidebands, measured in the heterodyne spectra, assume a peculiar shape, related to the modified system dynamics, with asymmetric features revealing and quantifying the quantum component of the squeezed oscillator motion.

The chapter is divided into three sections. In the first one (Sec. 4.1), I will introduce the theoretical model describing the system in the presence of parametric modulation drive. I will them briefly discuss the experimental setup for these measurements, Sec. 4.2 (more details can be found in Ch. 2). Finally (Sec. 4.3), the experimental results are discussed and compared with the theoretical model.

## 4.1 Theoretical Background

The physical system is composed by a Fabry-Perot cavity with $\kappa = \kappa_{in} + \kappa_{ex}$, where $\kappa_{in}$ is the input coupling rate, and $\kappa_{ex}$ includes the other losses, and a mechanical oscillator placed in its center. The input field is composed by

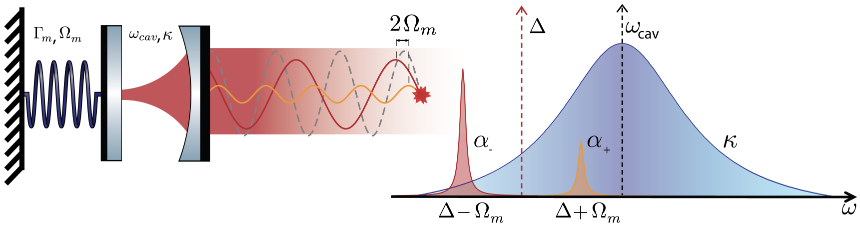

Figure 4.1: Conceptual scheme of the cavity of the field frequencies. Blue area shows the cavity spectral peak with a frequency equal to $\omega_{cav}$, and a linewidth $\kappa$. Left red area, around the red dash line at $\Delta$, shows the shape of the tone with the intensity $\alpha_-$, and in the right side the tone with intensity $\alpha_+$.

two tones, shifted by $\pm\Omega_m$ around the laser frequency $\omega_l$, where $\Omega_m$ is the effective mechanical resonance frequency, modified by the optomechanical interaction. The mean value of the input filed has the form:

$$\alpha_{in} = \alpha_-^{in} e^{-i(\omega_l - \Omega_m)t} + \alpha_+^{in} e^{-i(\omega_l + \Omega_m)t} \tag{4.1}$$

and the intracavity mean field can be written in the rotating frame as

$$\alpha = \alpha_- e^{i\Omega_m t} + \alpha_+ e^{-i\Omega_m t} \tag{4.2}$$

where

$$\alpha_\pm = \alpha_\pm^{in} \frac{\sqrt{\kappa_{in}}}{-i(\Delta \pm \Omega_m) + \kappa/2} \tag{4.3}$$

and $\Delta = \omega_l - \omega_{cav}$ is the detuning between the cavity resonance and the laser frequency. In this new configuration, the phonon annihilation and creation operator changes due to the optomechanical interactions. The general equations for $\widetilde{b}$ and $\widetilde{b}^\dagger$ are:

$$\widetilde{b}(\omega)\left(-i\omega + i\Omega_m^0 + \frac{\Gamma_m}{2}\right) = ig_0\left(\alpha\delta\widetilde{a}^\dagger(\omega) + \alpha^*\delta\widetilde{a}(\omega)\right) + \sqrt{\Gamma_m}\,\widetilde{b}_{th}(\omega), \tag{4.4}$$

$$\widetilde{b}^\dagger(\omega)\left(-i\omega - i\Omega_m^0 + \frac{\Gamma_m}{2}\right) = -ig_0\left(\alpha\delta\widetilde{a}^\dagger(\omega) + \alpha^*\delta\widetilde{a}(\omega)\right) + \sqrt{\Gamma_m}\,\widetilde{b}_{th}^\dagger(\omega). \tag{4.5}$$

see Sec. 1.3 for more details. The Fourier transform of $\alpha^*\delta a$ and $\alpha\delta a^\dagger$ become:

$$\mathcal{F}[\alpha^*\delta a] = \mathcal{F}[(\alpha_-^* e^{-i\Omega_m t} + \alpha_+^* e^{i\Omega_m t})\delta a] = \\ = \alpha_-^* \delta\widetilde{a}(\omega - \Omega_m) + \alpha_+^* \delta\widetilde{a}(\omega + \Omega_m) \quad (4.6)$$

and

$$\mathcal{F}[\alpha\delta a^\dagger] = \mathcal{F}[(\alpha_- e^{i\Omega_m t} + \alpha_+ e^{-i\Omega_m t})\delta a^\dagger] = \\ = \alpha_- \delta\widetilde{a}^\dagger(\omega + \Omega_m) + \alpha_+ \delta\widetilde{a}^\dagger(\omega - \Omega_m). \quad (4.7)$$

The photon creation and annihilation operators can be written in terms of the field $\alpha$ that interact with the mechanical oscillator. In the Fourier space the $\alpha(b^\dagger + b)$ can be written as:

$$\mathcal{F}[\alpha(b^\dagger + b)] = \mathcal{F}[(\alpha_- e^{i\Omega_m t} + \alpha_+ e^{-i\Omega_m t})(b^\dagger + b)] = \\ = \alpha_- X(\omega + \Omega_m) + \alpha_+ X(\omega - \Omega_m), \quad (4.8)$$

$$\mathcal{F}[\alpha^*(b^\dagger + b)] = \mathcal{F}[(\alpha_-^* e^{-i\Omega_m t} + \alpha_+^* e^{i\Omega_m t})(b^\dagger + b)] = \\ = \alpha_-^* X(\omega - \Omega_m) + \alpha_+^* X(\omega + \Omega_m), \quad (4.9)$$

where $X(\omega) = b(\omega) + b^\dagger(\omega)$. Using the equations of $\delta\widetilde{a}(\omega)$ and $\delta\widetilde{a}(\omega)^\dagger$, obtained in the Sec. 1.3, respectively Eq. 1.90 and 1.91, the fluctuations of the intractivity field in the Fourier space are

$$\delta\widetilde{a}(\omega) = \frac{1}{-i\omega - i\Delta + \kappa/2}\left\{ig_0\Big[\alpha_+ X(\omega-\Omega_m) + \alpha_- X(\omega+\Omega_m)\Big] + \sqrt{\kappa}\,\delta\widetilde{a}_{in}(\omega)\right\} \quad (4.10)$$

and

$$\delta\widetilde{a}^\dagger(\omega) = \frac{1}{-i\omega + i\Delta + \kappa/2}\left\{-ig_0\Big[\alpha_+^* X(\omega+\Omega_m) + \alpha_-^* X(\omega-\Omega_m)\Big] + \sqrt{\kappa}\,\delta\widetilde{a}_{in}^\dagger(\omega)\right\}. \quad (4.11)$$

Eqs. 4.6 and 4.7 thus become:

$$\mathcal{F}[\alpha^*\delta a] = ig_0\left\{\frac{1}{-i(\omega - \Omega_m) - i\Delta + \kappa/2}\Big[|\alpha_-|^2 X(\omega) + \alpha_-^*\alpha_+ X(\omega - 2\Omega_m)\Big] + \\ \frac{1}{-i(\omega + \Omega_m) - i\Delta + \kappa/2}\Big[|\alpha_+|^2 X(\omega) + \alpha_+^*\alpha_- X(\omega + 2\Omega_m)\Big]\right\} + \\ \sqrt{\kappa}\left[\alpha_-^* \frac{\delta\widetilde{a}_{in}(\omega - \Omega_m)}{-i(\omega - \Omega_m) - i\Delta + \kappa/2} + \alpha_+^* \frac{\delta\widetilde{a}_{in}(\omega + \Omega_m)}{-i(\omega + \Omega_m) - i\Delta + \kappa/2}\right] \quad (4.12)$$

and

$$\begin{aligned}\mathcal{F}[\alpha\delta a^\dagger] = -ig_0\Bigg\{ & \frac{1}{-i(\omega+\Omega_m)+i\Delta+\kappa/2}\Big[|\alpha_-|^2X(\omega)+\alpha_+^*\alpha_-X(\omega+2\Omega_m)\Big]+\\ & \frac{1}{-i(\omega-\Omega_m)+i\Delta+\kappa/2}\Big[|\alpha_+|^2X(\omega)+\alpha_-^*\alpha_+X(\omega-2\Omega_m)\Big]\Bigg\}+\\ & \sqrt{\kappa}\Bigg[\alpha_-\frac{\delta\widetilde{a}_{in}^\dagger(\omega+\Omega_m)}{-i(\omega+\Omega_m)+i\Delta+\kappa/2}+\alpha_+\frac{\delta\widetilde{a}_{in}^\dagger(\omega-\Omega_m)}{-i(\omega-\Omega_m)+i\Delta+\kappa/2}\Bigg]. \end{aligned} \tag{4.13}$$

When Eq. 4.10 and its Hermitian conjugate are replaced into Eq. 4.4 in the Fourier space, the mean-field factors $\alpha$ and $\alpha^*$ in the optomechanical coupling shift the $\delta\widetilde{a}$ and $\delta\widetilde{a}^\dagger$ operators by $\pm\Omega_m$, giving terms proportional to $\widetilde{b}(\omega)$, $\widetilde{b}(\omega\pm2\Omega_m)$, $\widetilde{b}^\dagger(\omega)$ and $\widetilde{b}^\dagger(\omega\pm2\Omega_m)$. Eq. 4.4 can thus be written as

$$\begin{aligned}\Big(-i\omega+i\Omega_m^0+\frac{\Gamma_m}{2}\Big)\widetilde{b}(\omega) = -g_0^2[C_1\widetilde{b}(\omega)+C_2\widetilde{b}(\omega-2\Omega_m)+C_3\widetilde{b}(\omega+2\Omega_m)+\\ +C_4\widetilde{b}^\dagger(\omega)+C_5\widetilde{b}^\dagger(\omega-2\Omega_m)+C_6\widetilde{b}^\dagger(\omega+2\Omega_m)]+\widetilde{b}_{in}(\omega)\end{aligned} \tag{4.14}$$

where $C_i$ are c-numbers and the source term is

$$\begin{aligned}\widetilde{b}_{in}(\omega) = {} & \sqrt{\Gamma_m}\,\widetilde{b}_{in}^{th}(\omega)+\\ & +ig_0\sqrt{\kappa}\Bigg[\alpha_-^*\frac{\delta\widetilde{a}_{in}(\omega-\Omega_m)}{-i\omega+i\Omega_m-i\Delta+\kappa/2}+\alpha_+^*\frac{\delta\widetilde{a}_{in}(\omega+\Omega_m)}{-i\omega-i\Omega_m-i\Delta+\kappa/2}+\\ & +\alpha_-\frac{\delta\widetilde{a}_{in}^\dagger(\omega+\Omega_m)}{-i\omega-i\Omega_m+i\Delta+\kappa/2}+\alpha_+\frac{\delta\widetilde{a}_{in}^\dagger(\omega-\Omega_m)}{-i\omega+i\Delta+i\Omega_m+\kappa/2}\Bigg].\end{aligned} \tag{4.15}$$

The total input noise source described by Eq. 4.15 includes thermal noise and back-action noise, the latter given by the terms into square brackets. The phonon creation and annihilation operators are centered in $\Omega_m$ and $-\Omega_m$, respectively. Therefore, the relevant terms in the optomechanical coupling, on the right-hand side of Eq. 4.14, are those proportional to $\widetilde{b}^\dagger(\omega-2\Omega_m)$

and $\widetilde{b}(\omega)$. Writing the explicit form of the $C$ coefficients, Eq. 4.14 becomes

$$\begin{aligned}
&\big(-i\omega + i\Omega_m^0 + \Gamma_m/2\big)\widetilde{b}(\omega) \simeq \widetilde{b}_{in}(\omega) + \\
&-g_0^2\Bigg[|\alpha_-|^2\,\widetilde{b}(\omega)\bigg(\frac{1}{-i\omega - i\Delta + i\Omega_m + \kappa/2} - \frac{1}{-i\omega + i\Delta - i\Omega_m + \kappa/2}\bigg) + \\
&\quad |\alpha_+|^2\,\widetilde{b}(\omega)\bigg(\frac{1}{-i\omega - i\Delta - i\Omega_m + \kappa/2} - \frac{1}{-i\omega + i\Delta + i\Omega_m + \kappa/2}\bigg) + \\
&\alpha_-^*\alpha_+\,\widetilde{b}^\dagger(\omega - 2\Omega_m)\bigg(\frac{1}{-i\omega - i\Delta + i\Omega_m + \kappa/2} - \frac{1}{-i\omega + i\Omega_m + i\Delta + \kappa/2}\bigg)\Bigg].
\end{aligned} \tag{4.16}$$

In the right hand side of Eq. 4.16, we notice the usual optomechanical effects of the two laser tones (first two terms inside square brackets), plus their coherent common interaction, proportional to the fields product $\alpha_-^*\alpha_+$, that originates the parametric squeezing. It can be directly calculated that this parametric effect is null for $\Delta = 0$, i.e. when the two tones are equally shifted with respect to the cavity resonance. The total input noise source described by Eq. 4.15 includes thermal noise and back-action noise, the latter given by the terms into square brackets. The standard optomechanical interaction is parameterized by the optical damping rate

$$\begin{aligned}
\Gamma_{opt} = 2g_0^2\,\mathbf{Re}\Bigg[&|\alpha_-|^2\left(\frac{1}{-i\omega - i\Delta + i\Omega_m + \kappa/2} - \frac{1}{-i\omega + i\Delta - i\Omega_m + \kappa/2}\right) + \\
&|\alpha_+|^2\left(\frac{1}{-i\omega - i\Delta - i\Omega_m + \kappa/2} - \frac{1}{-i\omega + i\Delta + i\Omega_m + \kappa/2}\right)\Bigg]
\end{aligned} \tag{4.17}$$

and by a frequency shift that determines the effective resonance frequency $\Omega_m$ according to the equation

$$\begin{aligned}
\Omega_m = \Omega_m^0 + g_0^2\,\mathbf{Im}\Bigg[&|\alpha_-|^2\left(\frac{1}{-i\omega - i\Delta + i\Omega_m + \kappa/2} - \frac{1}{-i\omega + i\Delta - i\Omega_m + \kappa/2}\right) + \\
&|\alpha_+|^2\left(\frac{1}{-i\omega - i\Delta - i\Omega_m + \kappa/2} - \frac{1}{-i\omega + i\Delta + i\Omega_m + \kappa/2}\right)\Bigg].
\end{aligned} \tag{4.18}$$

For an easier comparison with the experimental data, it is useful to define the total optomechanical coupling strength $g^2 = g_0^2\ (|\alpha_+|^2 + |\alpha_-|^2)$ and the ratio between intracavity powers $\epsilon_c = |\alpha_-|^2/(|\alpha_-|^2 + |\alpha_+|^2)$. Using the quasiresonant frequency condition $\omega \approx \Omega_m$ the total damping rate $\Gamma_{eff} =$

$\Gamma_m + \Gamma_{opt}$ can be written as

$$\Gamma_{eff} = \Gamma_m + g^2\kappa \left[\frac{\epsilon_c}{\Delta^2+(\kappa/2)^2} - \frac{\epsilon_c}{(\Delta-2\Omega_m)^2+(\kappa/2)^2} + \right. \\ \left. \frac{1-\epsilon_c}{(\Delta+2\Omega_m)^2+(\kappa/2)^2} - \frac{1-\epsilon_c}{\Delta^2+(\kappa/2)^2} + \right]. \quad (4.19)$$

With the same condition, Eq. 4.16 simplifies to

$$\big(-i\omega + i\Omega_m + \Gamma_{eff}/2\big)\widetilde{b}(\omega) = -\frac{\Gamma_{par}}{2}e^{i\phi}\,\widetilde{b}^\dagger(\omega-2\Omega_m) + \widetilde{b}_{in}(\omega) \quad (4.20)$$

where

$$\Gamma_{par} = \frac{4g_0^2|\alpha_+||\alpha_-|\Delta}{\Delta^2+\kappa^2/4} = \frac{4g^2\sqrt{\epsilon_c(1-\epsilon_c)}\Delta}{\Delta^2+\kappa^2/4} \quad (4.21)$$

and $\phi = \pi/2 + arg[\alpha_-^*\alpha_+]$. Moving to the frame rotating at $\Omega_m$, and defining the frequency with respect to the mechanical resonance $\Omega = \omega - \Omega_m$, Eq. 4.20 and its Hermitian conjugate can be written in the form of the system of coupled linear equations

$$\begin{pmatrix} -i\Omega + \frac{\Gamma_{eff}}{2} & \frac{\Gamma_{par}}{2}e^{i\phi} \\ \frac{\Gamma_{par}}{2}e^{-i\phi} & -i\Omega + \frac{\Gamma_{eff}}{2} \end{pmatrix} \begin{pmatrix} \widetilde{b}_R \\ \widetilde{b}_R^\dagger \end{pmatrix} = \begin{pmatrix} \widetilde{b}_{in} \\ \widetilde{b}_{in}^\dagger \end{pmatrix}. \quad (4.22)$$

The matrix determinant is:

$$\mathcal{D} = \Big(-i\Omega + \frac{\Gamma_+}{2}\Big)\Big(-i\Omega + \frac{\Gamma_-}{2}\Big) \quad (4.23)$$

where

$$\Gamma_\pm = \Gamma_{eff} \pm \Gamma_{par}. \quad (4.24)$$

The creation and annihilation operator in the rotating frame are:

$$\widetilde{b}_R = \frac{1}{\mathcal{D}}\Big[\Big(-i\Omega + \frac{\Gamma_{eff}}{2}\Big)\widetilde{b}_{in} - \frac{\Gamma_{par}}{2}e^{i\phi}\,\widetilde{b}_{in}^\dagger\Big], \quad (4.25)$$

$$\widetilde{b}_R^\dagger = \frac{1}{\mathcal{D}}\Big[\Big(-i\Omega + \frac{\Gamma_{eff}}{2}\Big)\widetilde{b}_{in}^\dagger - \frac{\Gamma_{par}}{2}e^{-i\phi}\,\widetilde{b}_{in}\Big]. \quad (4.26)$$

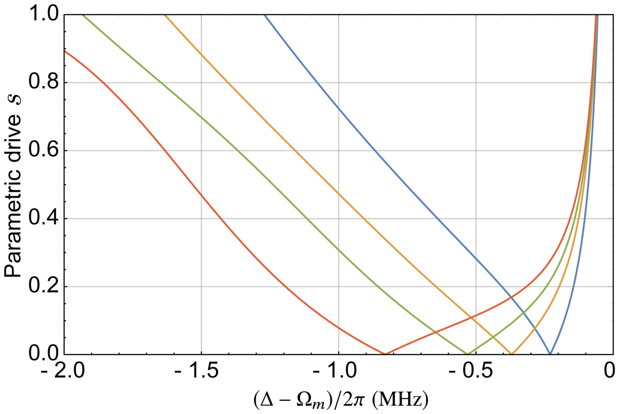

Figure 4.2: Parametric drive gain $s$ for different mechanical modes as a function of the detuning $\Delta$. Blue solid line, mechanical mode $(0, 1)$ at 230 kHz. Yellow solid line, mechanical mode $(1, 1)$ at 370 kHz. Green solid line, mechanical mode $(0, 2)$ at 530 kHz. Red solid line, mechanical mode $(0, 3)$ at 830 kHz.

The spectra of the Stokes and anti-Stokes sidebands $S_{\widetilde{b}_R\widetilde{b}_R}$ and $S_{\widetilde{b}^\dagger_R\widetilde{b}^\dagger_R}$ are

$$\begin{aligned}&2\pi S_{\widetilde{b}_R\widetilde{b}_R} = \left\langle \widetilde{b}_R(-\Omega)\widetilde{b}^\dagger_R(\Omega)\right\rangle = \\ &= \frac{1}{\mathcal{D}^2}\Bigg[\left(\Omega^2+\frac{\Gamma^2_{eff}}{4}\right)\left\langle \widetilde{b}_{in}(-\Omega)\widetilde{b}^\dagger_{in}(\Omega)\right\rangle - \frac{\Gamma_{par}}{2}e^{-i\phi}\left(i\Omega+\frac{\Gamma_{eff}}{2}\right)\left\langle \widetilde{b}_{in}(-\Omega)\widetilde{b}_{in}(\Omega)\right\rangle + \\ &\quad - \frac{\Gamma_{par}}{2}e^{i\phi}\left(-i\Omega+\frac{\Gamma_{eff}}{2}\right)\left\langle \widetilde{b}^\dagger_{in}(-\Omega)\widetilde{b}^\dagger_{in}(\Omega)\right\rangle + \frac{\Gamma^2_{par}}{4}\left\langle \widetilde{b}^\dagger_{in}(-\Omega)\widetilde{b}_{in}(\Omega)\right\rangle\Bigg]\end{aligned} \tag{4.27}$$

and

$$\begin{aligned}&2\pi S_{\widetilde{b}^\dagger_R\widetilde{b}^\dagger_R} = \left\langle \widetilde{b}^\dagger_R(-\Omega)\widetilde{b}_R(\Omega)\right\rangle = \\ &= \frac{1}{\mathcal{D}^2}\Bigg[\left(\Omega^2+\frac{\Gamma^2_{eff}}{4}\right)\left\langle \widetilde{b}^\dagger_{in}(-\Omega)\widetilde{b}_{in}(\Omega)\right\rangle - \frac{\Gamma_{par}}{2}e^{-i\phi}\left(-i\Omega+\frac{\Gamma_{eff}}{2}\right)\left\langle \widetilde{b}_{in}(-\Omega)\widetilde{b}_{in}(\Omega)\right\rangle + \\ &\quad - \frac{\Gamma_{par}}{2}e^{i\phi}\left(i\Omega+\frac{\Gamma_{eff}}{2}\right)\left\langle \widetilde{b}^\dagger_{in}(-\Omega)\widetilde{b}^\dagger_{in}(\Omega)\right\rangle + \frac{\Gamma^2_{par}}{4}\left\langle \widetilde{b}_{in}(-\Omega)\widetilde{b}^\dagger_{in}(\Omega)\right\rangle\Bigg].\end{aligned} \tag{4.28}$$

The correlation functions for the input noise source of Eq. 4.15 are obtained from Eqs. 1.86 -1.89 by considering that $\langle \hat{O}(t)\hat{O}^\dagger(t')\rangle = c\delta(t-t)$ implies $\langle \hat{O}(\Omega)\hat{O}^\dagger(\Omega')\rangle = c\delta(\Omega-\Omega')$. In the following subsections we will discuss the thermal and optical contributions.

## Thermal contribution

The thermal contributions to the sideband spectra are calculated from the correlation functions:

$$\frac{1}{2\pi}\left\langle \widetilde{b}_{in}(-\Omega)\widetilde{b}^\dagger_{in}(\Omega)\right\rangle_{th} = \frac{1}{2\pi}\left\langle \widetilde{b}_{th}(-\Omega)\widetilde{b}^\dagger_{th}(\Omega)\right\rangle = \Gamma_m(\bar{n}_{th}+1), \tag{4.29}$$

$$\frac{1}{2\pi}\left\langle \widetilde{b}^\dagger_{in}(-\Omega)\widetilde{b}_{in}(\Omega)\right\rangle_{th} = \frac{1}{2\pi}\left\langle \widetilde{b}^\dagger_{th}(-\Omega)\widetilde{b}_{th}(\Omega)\right\rangle = \Gamma_m \;\; \bar{n}_{th}. \tag{4.30}$$

The spectra are given by

$$S_{\widetilde{b}^\dagger_R\widetilde{b}^\dagger_R}\bigg|_{th} = \frac{\Gamma_m}{2}\left[\frac{n_{th}+1+s/2}{\Omega^2+(\Gamma_+/2)^2}+\frac{n_{th}+1-s/2}{\Omega^2+(\Gamma_-/2)^2}\right], \tag{4.31}$$

$$S_{\widetilde{b}_R\widetilde{b}_R}\bigg|_{th} = \frac{\Gamma_m}{2}\left[\frac{n_{th}+s/2}{\Omega^2+(\Gamma_+/2)^2}+\frac{n_{th}-s/2}{\Omega^2+(\Gamma_-/2)^2}\right], \tag{4.32}$$

where we have introduced the squeezing parameter $s = \Gamma_{par}/\Gamma_{eff}$. For a thermal state where $n_{th} \gg 1$ and $s$, the two spectra become equal:

$$S_{\widetilde{b}_R\widetilde{b}_R} \approx S_{\widetilde{b}^\dagger_R\widetilde{b}^\dagger_R} \approx \frac{n_{th}\Gamma_m}{2}\left[\frac{1}{\Omega^2+(\Gamma_+/2)^2}+\frac{1}{\Omega^2+(\Gamma_-/2)^2}\right]. \tag{4.33}$$

and therefore the asymmetry cannot be apprecieted at high occupation numbers ($\bar{n}_{th} \approx \bar{n}_{th}+1$).

## Optical Term

For the optical side, the contributions on the spectra consist of different terms given by the four possible combinations of the operators $\delta\widehat{a}_{in}$ and $\delta\widehat{a}^\dagger_{in}$ in the expectation value:

$$\frac{1}{2\pi}\left\langle \widetilde{b}_{in}(-\Omega)\widetilde{b}_{in}(\Omega)\right\rangle_{opt} = -g_0^2\kappa\frac{\alpha_-^*\alpha_+}{\Delta^2+\kappa^2/4}, \tag{4.34}$$

$$\tfrac{1}{2\pi}\left\langle \widetilde{b}^{\dagger}_{in}(-\Omega)\widetilde{b}^{\dagger}_{in}(\Omega)\right\rangle_{opt} = -g_0^2\kappa\tfrac{\alpha_-\alpha_+^*}{\Delta^2+\kappa^2/4} = \left(\tfrac{1}{2\pi}\left\langle \widehat{b}_{in}(-\Omega)\widehat{b}_{in}(\Omega)\right\rangle_{opt}\right)^*, \tag{4.35}$$

$$\tfrac{1}{2\pi}\left\langle \widetilde{b}^{\dagger}_{in}(-\Omega)\widetilde{b}_{in}(\Omega)\right\rangle_{opt} = g_0^2\kappa\left[\tfrac{|\alpha_-|^2}{(\Delta-2\Omega_m)^2+\kappa^2/4} + \tfrac{|\alpha_+|^2}{\Delta^2+\kappa^2/4}\right] = \mathcal{A}^+, \tag{4.36}$$

$$\tfrac{1}{2\pi}\left\langle \widetilde{b}_{in}(-\Omega)\widetilde{b}^{\dagger}_{in}(\Omega)\right\rangle_{opt} = g_0^2\kappa\left[\tfrac{|\alpha_-|^2}{\Delta^2+\kappa^2/4} + \tfrac{|\alpha_+|^2}{(\Delta+2\Omega_m)^2+\kappa^2/4}\right] = \mathcal{A}^-, \tag{4.37}$$

where $\mathcal{A}^+$ and $\mathcal{A}^-$ are respectively the Stokes and anti-Stokes rates [6]. From such rate we can define the optical spring as $\Gamma_{opt} = \mathcal{A}^- - \mathcal{A}^+$, and the optical contributions become:

$$S_{\widetilde{b}^{\dagger}_R\widetilde{b}^{\dagger}_R}\Big|_{opt} = \tfrac{1}{2\pi}\left\langle \widetilde{b}_R(-\Omega)\widetilde{b}^{\dagger}_R(\Omega)\right\rangle_{opt} = \tfrac{1}{2}\left[\tfrac{\mathcal{A}^- - \frac{s}{2}\Gamma_{opt}}{\Omega^2+\left(\frac{\Gamma_-}{2}\right)^2} + \tfrac{\mathcal{A}^- + \frac{s}{2}\Gamma_{opt}}{\Omega^2+\left(\frac{\Gamma_+}{2}\right)^2}\right] \tag{4.38}$$

and

$$S_{\widetilde{b}_R\widetilde{b}_R}\Big|_{opt} = \tfrac{1}{2\pi}\left\langle \widetilde{b}^{\dagger}_R(-\Omega)\widetilde{b}_R(\Omega)\right\rangle_{opt} = \tfrac{1}{2}\left[\tfrac{\mathcal{A}^+ + \frac{s}{2}\Gamma_{opt}}{\Omega^2+\left(\frac{\Gamma_-}{2}\right)^2} + \tfrac{\mathcal{A}^+ - \frac{s}{2}\Gamma_{opt}}{\Omega^2+\left(\frac{\Gamma_+}{2}\right)^2}\right]. \tag{4.39}$$

For the Stokes and anti-Stokes rates, it is possible to define the back-action occupation number (it defines a minimum occupation number achievable through the optical cooling):

$$n_{BA} = \frac{\mathcal{A}^+}{\mathcal{A}^- - \mathcal{A}^+} = \frac{\mathcal{A}^+}{\Gamma_{opt}}, \tag{4.40}$$

$$n_{BA} + 1 = \frac{\mathcal{A}^-}{\mathcal{A}^- - \mathcal{A}^+} = \frac{\mathcal{A}^-}{\Gamma_{opt}}. \tag{4.41}$$

From this two definitions, the optical contributions can be written as

$$S_{\widetilde{b}^{\dagger}_R\widetilde{b}^{\dagger}_R}\Big|_{opt} = \frac{\Gamma_{opt}}{2}\left[\frac{n_{BA}+1-\frac{s}{2}}{\Omega^2+\left(\frac{\Gamma_-}{2}\right)^2} + \frac{n_{BA}+1+\frac{s}{2}}{\Omega^2+\left(\frac{\Gamma_+}{2}\right)^2}\right], \tag{4.42}$$

$$S_{\widetilde{b}_R\widetilde{b}_R}\Big|_{opt} = \frac{\Gamma_{opt}}{2}\left[\frac{n_{BA}-\frac{s}{2}}{\Omega^2+\left(\frac{\Gamma_-}{2}\right)^2} + \frac{n_{BA}+\frac{s}{2}}{\Omega^2+\left(\frac{\Gamma_+}{2}\right)^2}\right]. \tag{4.43}$$

### Total spectra

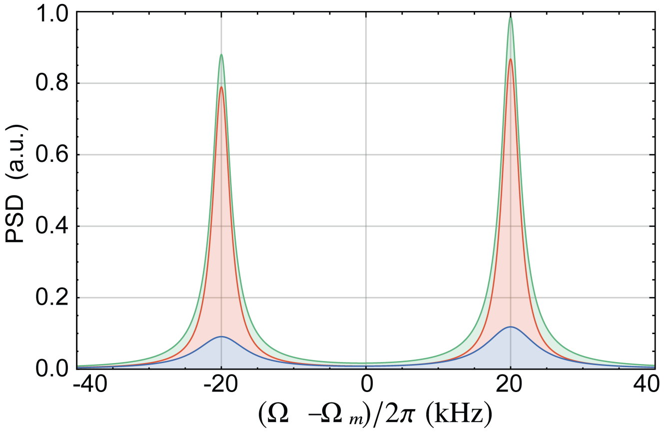

Figure 4.3: Heterodyne spectra simulation, around the mechanical frequency $\Omega_m$, showing the Stokes (left side) and the anti-Stokes (right side) vibrational bands. The parametric gain is around $s = 0.5$, the mean phonon occupancy is 5 and the mechanical linewidth of $\approx 5$ kHz. Red solid line: the Lorentzian shape with a sharp linewidth equal to $\Gamma_-$, Anti-Squeezing quadrature. Blue solid line: the Lorentzian shape with a broad linewidth equal to $\Gamma_+$, Squeezing quadrature. Green solid line: shows the full contribution on the spectrum, $S_{\tilde{b}_R\tilde{b}_R}(\Omega) + S_{\tilde{b}_R^\dagger\tilde{b}_R^\dagger}(\Omega)$.

The total spectra for the Stokes and the anti-Stoke sidebands are thus given by

$$S_{\tilde{b}_R^\dagger\tilde{b}_R^\dagger}(\Omega) = \frac{\Gamma_{eff}}{2}\left[\frac{\bar{n}+1+\frac{s}{2}}{\Omega^2+\left(\frac{\Gamma_-}{2}\right)^2} + \frac{\bar{n}+1-\frac{s}{2}}{\Omega^2+\left(\frac{\Gamma_+}{2}\right)^2}\right], \tag{4.44}$$

$$S_{\tilde{b}_R\tilde{b}_R}(\Omega) = \frac{\Gamma_{eff}}{2}\left[\frac{\bar{n}+\frac{s}{2}}{\Omega^2+\left(\frac{\Gamma_-}{2}\right)^2} + \frac{\bar{n}-\frac{s}{2}}{\Omega^2+\left(\frac{\Gamma_+}{2}\right)^2}\right], \tag{4.45}$$

where $\bar{n}$ is the oscillator effective phonon number in the absence of parametric effect

$$\bar{n} = \frac{\bar{n}_{th}\Gamma_m + n_{BA}\Gamma_{opt}}{\Gamma_{eff}}. \tag{4.46}$$

For $s > 0$ the spectral shape of each sideband is composed by the sum of two Lorentzian curves with the same center but different amplitudes and widths (two for the Stokes and two for the anti-Stokes sideband) $\Gamma_\pm$, related to the squeezing and anti-squeezing quadrature, respectively. The ratios between the areas of the broad and narrow Lorentzian components in the two sidebands are

$$R_+ = \frac{\bar{n}+1+s/2}{\bar{n}-s/2}, \tag{4.47}$$

$$R_- = \frac{\bar{n}+1-s/2}{\bar{n}+s/2}. \tag{4.48}$$

For $s = 0$ Eqs. 4.44 and 4.45 are Lorentzians corresponding to the Stokes and anti-Stokes sidebands. From the ration of their areas we can extract the occupation number

$$R_0 = \frac{\bar{n}+1}{\bar{n}}. \tag{4.49}$$

## Quadratures

A generic quadrature operator can be written as $X_\theta = (e^{i\theta}\,\hat{b}_R + e^{-i\theta}\,\hat{b}_R^\dagger)/2$. In the Fourier space the equations become:

$$\begin{aligned}\widetilde{X}_\theta = \frac{1}{2\,\mathcal{D}}\Bigg[&e^{i\theta}\,\widetilde{b}_{in}\left(-i\Omega + \frac{\Gamma_{eff}}{2} - \frac{\Gamma_{par}}{2}e^{-i(2\theta+\phi)}\right)+ \\ &+ e^{-i\theta}\,\widetilde{b}_{in}^\dagger\left(-i\Omega + \frac{\Gamma_{eff}}{2} - \frac{\Gamma_{par}}{2}e^{i(2\theta+\phi)}\right)\Bigg]\end{aligned} \tag{4.50}$$

where we used Eq. 4.25 and 4.26. The minimum and maximum fluctuations characterize the quadratures defined respectively by $2\theta + \phi = \pi$ and $2\theta + \phi = 0$. These quadratures are defined in the following as $Y \equiv X_{-\phi/2}$ and $X \equiv X_{-\phi/2+\pi/2}$, and given by

$$Y = \frac{e^{i\phi}\,\widetilde{b}_{in} + e^{-i\phi}\,\widetilde{b}_{in}^\dagger}{-i\Omega + \frac{\Gamma_+}{2}}, \tag{4.51}$$

$$X = i\;\frac{e^{i\phi}\,\widetilde{b}_{in} + e^{-i\phi}\,\widetilde{b}_{in}^\dagger}{-i\Omega + \frac{\Gamma_-}{2}}. \tag{4.52}$$

and the associated spectra are

$$S_{YY} = \frac{\Gamma_{eff}(2\bar{n}+1)}{4\left(\Omega^2 + \frac{\Gamma_+^2}{4}\right)}, \tag{4.53}$$

$$S_{XX} = \frac{\Gamma_{eff}(2\bar{n}+1)}{4\left(\Omega^2 + \frac{\Gamma_-^2}{4}\right)}. \tag{4.54}$$

The two quadrature spectra scale in a different way with the parametric drive, s. For the $X$-quadrature the linewidth decreases as the parametric drive increase, and vicevesa for the $Y$-quadrature. The integrals of the spectra on $\Omega$ give the variances ($\sigma_X = \int_{-\infty}^{\infty} S_{XX} \frac{d\Omega}{2\pi}$):

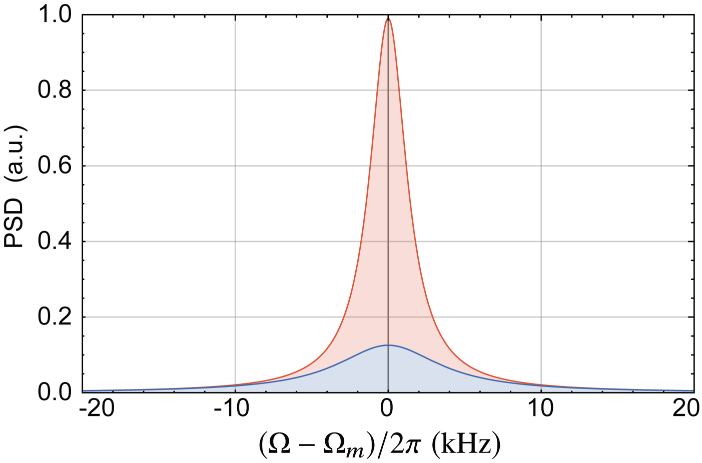

Figure 4.4: Quadrature spectra simulation, around the mechanical frequency $\Omega_m$. The parametric gain is just $s = 0.5$ and mean phonon occupancy of 5, mechanical linewidth of $\approx 5$ kHz. Red solid line: Anti-squeezing quadrature ($S_{XX}$). Blue solid line: squeezing quadrature ($S_{YY}$).

$$\sigma_Y^2 = \frac{\sigma_0^2}{1+s}, \tag{4.55}$$

$$\sigma_X^2 = \frac{\sigma_0^2}{1-s}, \tag{4.56}$$

where $\sigma_0^2 = (2\bar{n}+1)/4$ is the variance when the parametric gain is zero. The quadrature variances normalize to the variance at $s = 0$ as a function of the tones intensity ratio $1 - \epsilon_c$, are shown in the Fig. 4.5. To summarize, in a classical description the motion of the oscillator is described by commuting variables, and the spectra corresponding to the two motional sidebands must be identical. On the other hand, in a quantum-mechanical description, even if the oscillator is dominated by thermal noise (i.e., $\bar{n} \gg 1$), the sideband asymmetry is always present ($R_0 > 1$), being originated by the noncommutativity between its ladder operators. Of course, the effect is actually measurable only for moderately low occupation numbers $\bar{n}$. In the presence of parametric modulation, when the system is in a squeezed state, the sideband ratios $R_+$ and $R_-$ differ not only from unity, but also from the ratio $R_0$ measured in a thermal state. Namely, the ratio is higher for the broadened Lorentzian component, while for the narrowed component it approaches unity as $s \to 1$ (i.e., close to the parametric instability threshold). Therefore, the quantum features of the oscillator motion can be brought out even for a state having a variance exceeding that of the ground state in any quadrature and, besides thermal noise, even for states that are not of minimal uncer-

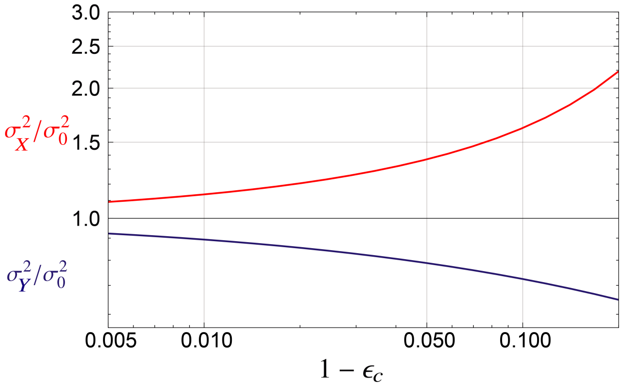

Figure 4.5: Variances simulation normalize at the variance at parametric modulation null, $s = 0$, both are plotted as a function of the ratio between the intensity of the parametric modulation drive and the total power $(1-\epsilon_c)$. That trend is calculated at mean phonon occupancy of 5. Red solid line: normalized variance of anti-squeezing quadrature $(\sigma_X^2/\sigma_0^2)$. Blue solid line: normalized variance of squeezing quadrature $(\sigma_Y^2/\sigma_0^2)$.

tainty (i.e., with $\langle X^2\rangle\langle Y^2\rangle > 1/16$) as those created by parametric squeezing.

In the following, we describe an experimental study of this effect and provide evidence of the realization of a nonclassical state of the macroscopic mechanical oscillator.

## 4.2 Experimental Apparatus

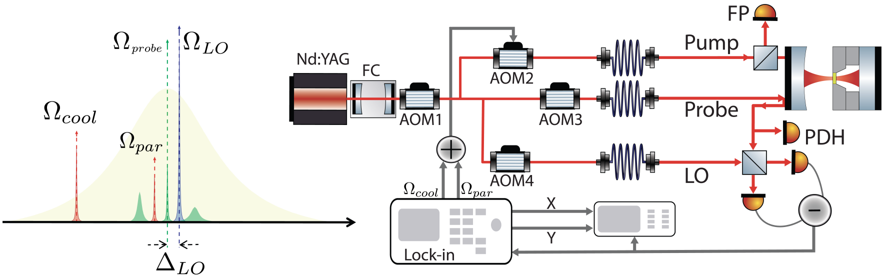

Figure 4.6: Experimental apparatus outline and the frequencies beam sketch, it is described in the text.

A simplified scheme of the experimental setup and of the field frequencies used in the experiment is sketched in Fig. 4.6 (further details can be found in Ch. 2). The laser light (Nd:YAG) is filtered by a Fabry-Perot cavity with a linewidth of 30 kHz. The transmitted beam is split into three different beams, the frequencies of which are controlled by three different AOM and sent to the optomechanical cavity (OMC) by optical fibers. The probe beam is kept resonant with the OMC using the PDH technique with a servo loop (AOM1 corrects the fast fluctuation, PZT for the long-term drifts of the cavity length). The input probe power is 40 $\mu$W, where only 20 $\mu$W are injected in the cavity as half power is in the two sidebands at 13.3 MHz from the carrier, used for the locking scheme. About $\sim 2$ $\mu$W of the reflected probe are used in the PDH detection and $\sim 10$ $\mu$W are combined with a local oscillator beam (LO) $\sim 2$ mW and sent to a heterodyne balanced detection. The losses in the reflected beam are $\sim 8$ $\mu$W. The local oscillator frequency, $\Omega_{LO}$ is blue-shifted with respect to the probe by $\Delta_{LO}/2\pi = 11$ kHz. The detection method is a heterodyne at low frequency [58]. The heterodyne balance signal is acquired and sent into a lock-in amplifier and demodulated at $\Omega_m$.

The two quadrature outputs of the lock-in are simultaneously acquired and off-line processed. The third beam (pump beam), is sent to the cavity and it is orthogonally polarized with respect to the probe. The beam is controlled by the AOM2, it is driving by the sum of two radiofrequency signals. The main radiofrequency is at $\Omega_{cool}$, red-detuned from the cavity resonance, to cool down the oscillator motion. A second frequency at $\Omega_{par}$, blue-shifted from the main one by $\Omega_{par} - \Omega_{cool} = 2\Omega_m$, realizes the parametric modulation. All the radiofrequency sinusoidal signals used in the experiment, for driving the AOMs and as reference in the lock-in amplifier, are kept phase coherent (all the frequency generator have only one clock as reference). This is very important to realize a phase-sensitive heterodyne detection. We focus on the mechanical mode $(0, 2)$ at frequency 530 kHz. As described in Ch. 2, the sample is placed in a Fabry-Perot cavity, 2 mm far from the flat end mirror. The total cavity length, $L = 3.92$ mm. The optomechanical cavity is placed in a helium flux cryostat, where is cooled down to a bath temperature of $\sim 7$ K, corresponding to a thermal occupation number of $2.6 \times 10^5$ for the mechanical mode $(0, 2)$. At cryogenic temperatures the measured cavity finesse and linewidth are $\mathcal{F} = 20000$ and $\kappa/2\pi = 1.9$ MHz, respectively. The single photon coupling rate for the considered mechanical mode is $g_0/2\pi \backsimeq 30$ Hz. All this parameters are measured independently. The finesse is measured from the reflected beam, where the two sidebands at 13.3 MHz are used to calibrate the linewidth (more details are given in Sec. 2.1.1). The vacuum optomechanical coupling $g_0$ is measured from different heterodyne acquisition at different power of the cooling beam, without any parametric tone. More details about the evaluation of $g_0$ are reported in Ch. 3. Part of the pump beam is detected with a fast photodiode (FP) with a bandwidth of 200 MHz. A spectrum is acquired to measure the tones intensity at their respective frequency (the two radio-frequencies are around of 110 MHz, shifted by $2\Omega_m$). In order to change the parametric gain $s$, we act on the ration between two tones without change the cooling tone.

## 4.3 Experimental Results

We now analyze the oscillator motion in a mechanical squeezing state; realized by parametric modulation of the oscillator spring constant. In particular, we focus on the sidebands spectra obtained in a balanced heterodyne detection searching of quantum signatures of the squeezing motion certified by direct measurements on the quadratures spectra. The heterodyne and quadratures time-traces are acquired simultaneously, while the frequency between the two tones in the pump beam, is periodically switched from resonance, $\Omega_{cool} - \Omega_{par}$, to out of it by $\Delta_{shift} = 12$ kHz every 5 s. The frequency shift is quality larger than the mechanical width (in this work it is small than 6 kHz), but it is much smaller than the cavity linewidth ($\sim 2$ MHz) in this way the coherent effect on the two tones is negligible, while maintaining the cooling effect of the modulation tone almost constant. The heterodyne time series are 10 seconds long. The two segments are used to calculate the two different spectra with a frequency resolution of 0.2 Hz. They are averaged over 10 consecutive time series for the subsequent analysis. The most straightforward method to show squeezing is the direct measurement of the variance in different quadratures that are usually chosen by tuning the local oscillator phase in a homodyne detection. On the other hand, in a standard heterodyne setup, the rapidly rotating phase difference between signal and local oscillator prevents the access to selected quadratures. This drawback can be overcome by controlling such phase difference [58]. In our setup, all the oscillators are indeed phase locked, including the time base of a lock-in amplifier that demodulated the heterodyne signal at $\Omega_m$. The spectrum of the lock-in output signal is a quadrature spectrum, centered at $\Delta_{LO}$. The demodulation phase is chosen in order to maximize the squeezed effect on the quadratures. The quadratures spectra are acquired and analyzed independently from the heterodyne signals, and the analyses agrees for both the Lorentzian widths and the squeezing factor. We can accurately compare the spectra with and without parametric modulation even in the presence of slow variations in the system parameters. In order to avoid the effects of possible long-term drifts during the measurements, all the radio-frequency signals used to drive the AOMs are phase locked. A typical example of the heterodyne spectra and corresponding quadratures are shown in the Fig. 4.7.

In the quadratures spectra (Fig. 4.7a) and 4.7b)), the mechanical peak is visible at the frequency $\Omega = \Delta_{LO}$. The peak is originated by the superposition of the two motional sidebands. The two orthogonal quadrature peaks are fitted by the sum of two equal Lorentzian shapes centered at $\pm\Delta_{LO}$:

$$S(\omega) = \sigma_0^2 \left[ \frac{\Gamma/2}{(\Gamma/2)^2 + (\omega - \Delta_{LO})^2} + \frac{\Gamma/2}{(\Gamma/2)^2 + (\omega + \Delta_{LO})^2} \right]. \qquad (4.57)$$

When the parametric modulation is out of resonance (Fig. 4.7a)), the Lorentzian curves fitting the two orthogonal quadratures coincide within the statistical uncertainty and their widths match $\Gamma_{eff}$ extracted from the corresponding heterodyne spectra. When the parametric modulation is on (Fig. 4.7b)), the spectra of one quadrature becomes narrower (anti-squeezed) and simultaneously the orthogonal one becomes broader (squeezed), we use the same fitting function 4.57, but with different areas ($\sigma^2_{X,Y}$) and different widths ($\Gamma_{X,Y}$) for the two quadratures. The ratio between the variances and widths with and without the parametric modulation gives the parametric gain $s$:

$$\frac{\sigma^2_{Y,X}}{\sigma^2_0} = \frac{1}{1 \pm s}, \tag{4.58}$$

and

$$\frac{\Gamma_{Y,X}}{\Gamma_{eff}} = 1 \pm s. \tag{4.59}$$

The heterodyne spectrum consist of two motional sidebands, separated by $2\Delta_{LO}$. The signal shapes are fitted by two Lorentzian curves having the identical width, $\Gamma_{eff}$, and two different areas ($\mathcal{A}_{AS}$ and $\mathcal{A}_S$), proportional to $\bar{n}$ (anti-Stokes) and $\bar{n}+1$ (Stokes):

$$H(\omega)|_{s=0} = \left[\frac{\mathcal{A}_{AS}\,\Gamma_{eff}/2}{\Gamma^2_{eff}/4 + (\omega - \Omega_m - \Delta_{LO})^2} + \frac{\mathcal{A}_S\,\Gamma_{eff}/2}{\Gamma^2_{eff}/4 + (\omega - \Omega_m + \Delta_{LO})^2}\right]. \tag{4.60}$$

The ratio $R_0$ between the areas of the two curves is corrected for the residual probe detuning as described in Ch. 3 and Ref. [20]. Such ratio gives the oscillator occupation number $\bar{n}$ according to Eq. 4.49. The theoretical spectra of the Stokes and anti-Stokes sidebands with the parametric modulation, are proportional, respectively, to Eq. 4.44 and 4.45 and thus define four Lorentzian contributions with linewidths $\Gamma_\pm = \Gamma_{eff} \pm \Gamma_{par} = \Gamma_{eff}(1 \pm s)$, where $\Gamma_\pm$ corresponds to those obtained from the quadratures spectra, $\Gamma_{Y,X}$. The parametric gain is $s = \Gamma_{par}/\Gamma_{eff}$, where the parametric width is described in the Eq. 4.21. An example of the heterodyne spectra in the presence of modulation is shown in Fig. 4.7d). The spectral peaks are fitted using the function

$$H(\omega)|_{s\neq 0} = \left[\frac{A^b_S\;\Gamma_+/2}{(\Gamma_+/2)^2 + (\omega - \Omega_m + \Delta_{LO})^2} + \frac{A^b_{AS}\;\Gamma_+/2}{(\Gamma_+/2)^2 + (\omega - \Omega_m - \Delta_{LO})^2}\right] + \\ + \left[\frac{A^n_S\;\Gamma_-/2}{(\Gamma_-/2)^2 + (\omega - \Omega_m + \Delta_{LO})^2} + \frac{A^n_{AS}\;\Gamma_-/2}{(\Gamma_-/2)^2 + (\omega - \Omega_m - \Delta_{LO})^2}\right] \tag{4.61}$$

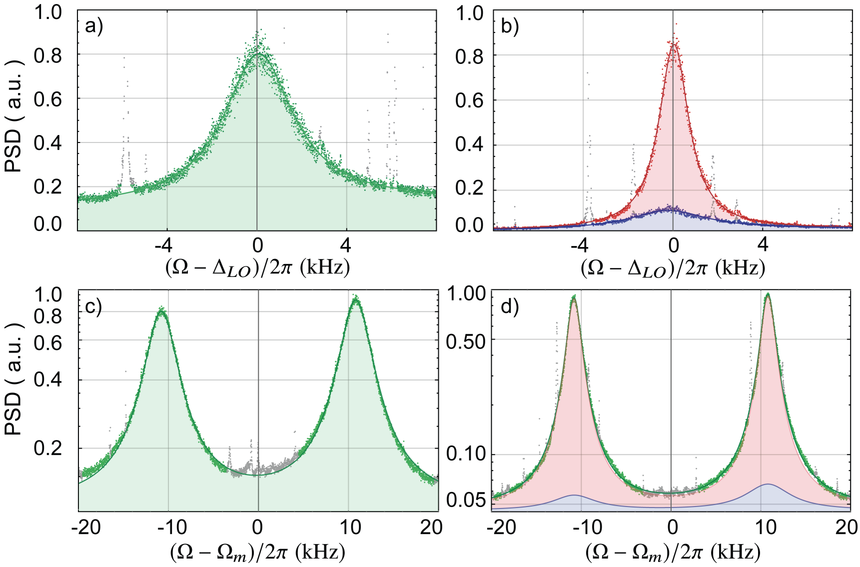

Figure 4.7: a), b): Spectra of the fluctuations in two quadratures, obtained by phase-sensitive demodulation of the heterodyne signal at $\Omega_{par}/2$, a) without parametric drive and b) with parametric drive. In a) the two spectra (dark and light green symbols) are not distinguishable, and one single Lorentzian fit is shown (solid line). In b) the two spectra (red and blue symbols) are fitted with different Lorentzian curves (red and blue solid lines). c), d): Heterodyne spectra (without demodulation) around the (0,2) membrane mode at $\Omega_m/2\pi \approx 530$ kHz, c) without parametric drive and d) with parametric drive (shown in log scale). In c) the spectrum is fitted by Lorentzian curves (solid line). In d) the fitting function (dark green line) is the superposition of a broad and a narrow Lorentzian shape, whose contributions are shown with blue and red lines.

where the apex $n$ identifies the narrow Lorentzian and $b$ the broader one. In 4.61 $\Gamma_{eff}$ is fixed to the value derived from the corresponding spectra at $s = 0$ while the parametric gain $s$ is left as a free fitting parameter. The heterodyne and quadrature parametric gain $s$ will be compared. The Lorentzian area ratios, broad and narrow, will give the asymmetry $R_{\pm}$. The system is studied varying different parameters: $\epsilon_c$, $P_{pump}$ and $\Delta_{pump}$.

## Asymmetry vs Parametric gain

We now consider the behavior of sidebands asymmetry as a function of the parametric gain $s$, keeping constant the total pump power injected in the cavity. The gain is varied by controlling the intensify of the parametric tone $P_{par}$. We acquire data for two different pump power values, respectively, 70 $\mu$W and 45 $\mu$W. For both powers the cooling detuning is fixed at $\Delta_{cool} = -1.2$ MHz, where the pump detuning is $\Delta_{pump} = \Delta_{cool} + \Omega_m$. As mentioned before for each value of $P_{par}$ we acquire 5 spectra with and without modulation, the results distribution gives the mean value and standard deviation. The data are shown in Fig. 4.8. Green dots and solid line, show respectively the experimental results and the theoretical prediction of the asymmetry when the parametric modulation is out of resonance. The asymmetry for the modulation out of resonance is a function of the intensity of the parametric drive, normalized to the total intensity, $1 - \epsilon_c$. When the parametric tone is not resonant (i.e., the parametric effect is off), the ratio $R_0$ (green symbols) remains almost constant for both occupation numbers, although we observe a clear decreasing trend as the parametric tone is increased. Such behavior is well reproduced by theoretical curves (see Eq. 4.19) calculated by using independently measured parameters, and it is due to a change in the relative strength of the two pump tones, which results in a slightly reduced cooling power. We note that the parametric tone is injected into the cavity through the pump beam and the parametric effect is turned off by shifting the driving frequency from $2\Omega_m$ to $2\Omega_m + \Delta_{shift}$. Although this procedure allows us to reduce to a minimum the changes in the cooling efficiency (as explained before), a residual effect is still present.

Fig. 4.8 also shows the sideband asymmetry for the Lorentzian components related to the broad quadrature $R_+$ (blue symbols) and narrow quadrature $R_-$ (red symbols), with resonant parametric effect. The parametric gain $s$ used to calibrate the horizontal axis in the figure is deduced from the width of the Lorentzian curves, as above described. The corresponding theoreti-

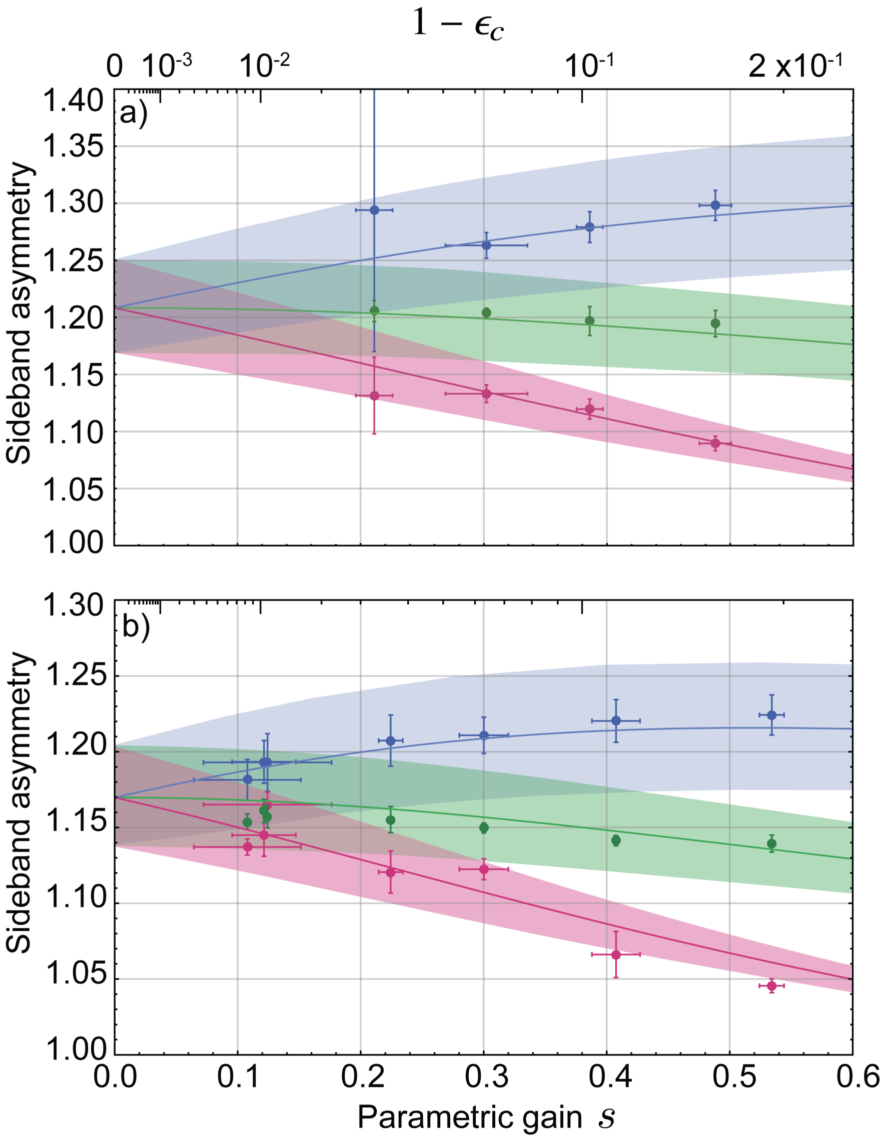

Figure 4.8: Green symbols: sideband asymmetry $R_0$ with no parametric drive (i.e., with detuned modulation tone), for increasing power in the modulation tone. Sideband ratios $R_+$ (blue circles) and $R_-$ (red circles) with coherent parametric drive. The values of $s$ in the abscissa are extracted from the fitted widths $\Gamma_+ = \Gamma_{eff}(1+s)$ and $\Gamma_- = \Gamma_{eff}(1-s)$. Solid lines show the corresponding theoretical behavior, with shadowed areas given by the uncertainty in the system parameters (in particular, 5% in the cavity width and 0.5 K in the temperature).

cal ratios can be calculated from the theoretical spectra $S_{\widetilde{b}^\dagger\widetilde{b}^\dagger}$ and $S_{\widetilde{b}\widetilde{b}}$ (Eqs. 4.44 and 4.45) and are given by Eqs. 4.47 and 4.48. Such theoretical curves are also plotted in Fig. 4.8 without free fitting parameters, showing a good quantitative agreement with the experimental data. The shadowed areas, around the solid line, given by the uncertainty in the system parameters (in particular, 5% in the cavity width and ±0.5 K in the temperature measurement).

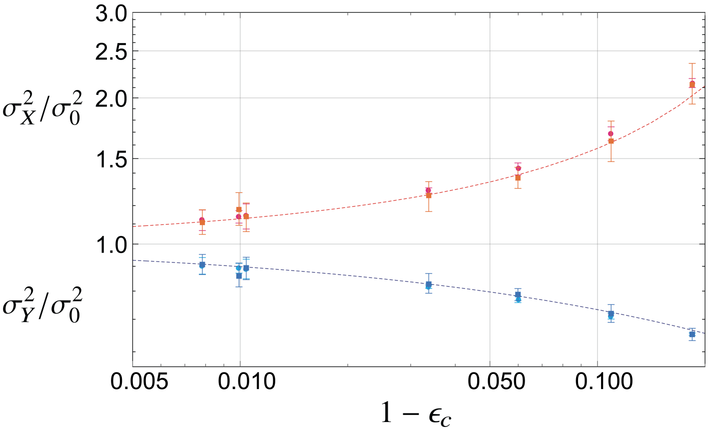

Figure 4.9: Variance in the $X$ (orange square) and $Y$ (cyan square) quadratures, normalized to $\sigma_0^2$, as a function of the ratio between modulation and cooling tones, for constant total pump power. Dashed lines show the theoretical behavior. Red and blue circles are the correspondent expected values, calculated respectively as $1/(1-s)$ and $1/(1+s)$.

The gain measured in the heterodyne and quadrature detection are compared for both pump powers. The parametric gain $s$ obtained from the fitted Lorentzian widths is in agreement with its estimate extracted from the variances of the two quadratures. This is shown in Fig. 4.9, where the circle points correspond to the values $1/(1-s)$ and $1/(1+s)$ obtained from the widths of heterodyne spectra (red and blue circles). These data agree with the measurements of the variance in the anti-squeezed (orange circle) and squeezed (cyan circle) quadratures and with the theoretical predictions (dashed lines).

For a pump power of 70 $\mu$W, and without any parametric modulation, the sideband ration is $\sim 1.21$, that corresponds to a phonon occupancy of $\sim 4.8$. The variance in each quadrature is still $\sim 10$ times larger with respect to the ground state value $\langle x \rangle^2 = x_{xzp}^2(2\bar{n}+1)$. The maximum displayed squeezing occurs for a parametric gain $s = 0.49 \pm 0.01$, where $\sigma_Y^2$ is reduced to the level of $0.67\ \sigma_0^2$. We notice that $\sigma_0^2$ is steel 6 times higher than the $x_{ZPF}^2$. At the pump power of 45 $\mu$W, the mechanical occupation at $s = 0$ is 5.8 phonons, it means $\sim 12$ times far from the variance of the quantum ground state. In this setup configuration, the maximum value of the parametric gain obtained is $0.53 \pm 0.01$, the maximum reduction of the squeezed quadrature is $0.65\ \sigma_0^2$.

## Asymmetry vs pump power

We now analyze the sideband asymmetry as a function of the pump power injected in the optomechanical cavity. The pump detuning is fixed at $-1.2$ MHz and we also fix the ratio between the two tones (cooling and parametric drive) in order to keep the gain $s$ constant as the power is varied. The effective mechanical width, $\Gamma_{eff}$ increase linearly with the pump power injected in the optomechanical cavity, if no extra noise is present. This linear trend was verified during the analysis procedure (see Fig. 4.10a). The red solid line displays the result of linear fit, and the blue dots the experimental data correspondent to the pump power measured in front of the optomechanical cavity. For each power the mechanical width is extracted from the spectra without the parametric modulation. At zero pump power the effective

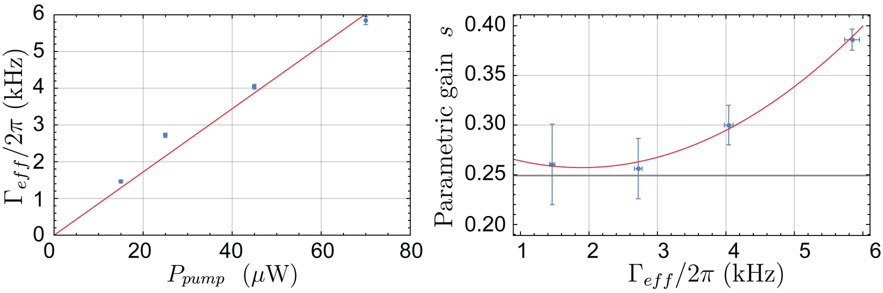

Figure 4.10: a) blue dots: measured width as a function of the measured pump power. Red lines: linear fit. b) phenomenologically dependence of $s$ on $\Gamma_{eff}$, the experimental data (blue dots) are fitted with a polynomial function (red line). The $\chi^2$ of the fit is around 0.1.

linewidth converges to the mechanical linewidth, $\Gamma_m \approx 80$ mHz. When the probe detuning is not exactly zero, it adds a contribution on the optical spring, that could explain the not perfect overlap between the fit and the experimental points. The asymmetry as a function of the effective linewidth, $\Gamma_{eff}$ is displayed in Fig. 4.11, where we use the model in Fig. 4.11a) assuming a constant parametric gain $s$, evaluated from independent measurements as explained in the Sec. 4.2. The value used in the model is $s \sim 0.29$. Circles are the experimental data with and without the parametric modulation. Green symbols refer to the sideband asymmetry $R_0$ (no parametric drive), while the blue and red symbols show the rations $R_+$ and $R_-$ for the broad and narrow Lorentzian contributions. The solid lines display the theoretical prediction and shadowed areas represent uncertainties in the system parameters. All the error bars are as described in the previous subsections. The data of $R_+$ and $R_-$ depart from the theoretical predictions, in particular at high pump power. During the measurements, the parametric gain is maintained roughly constant by adjusting the strength of the parametric tone each time the pump power is varied. However, we observe a variation of $s$ as shown in Fig. 4.10b). We remind that the parametric gain is described from the equation: $s = \Gamma_{par}/\Gamma_{eff}$, have a consequence we do not expect in

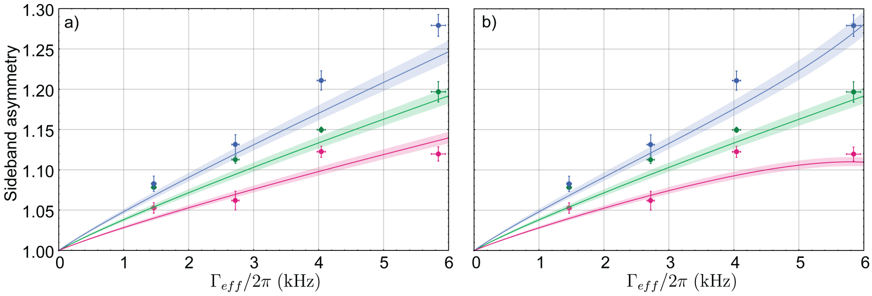

Figure 4.11: Green symbols: sideband asymmetry $R_0$ with no parametric drive (i.e., with detuned modulation tone), for increasing power in the modulation tone. Sideband ratios $R_+$, (blue circles) and $R_-$, (red circles) with coherent parametric drive. Solid lines in panel a) show the corresponding theoretical behavior at $s$ constant, while in panel b) they take into account the changes of $s$ with $\Gamma_{eff}$ obtained from the fit in Fig. 4.10b). The shadowed areas given by the uncertainty in the system parameters. More details in the text.

principle a dependence of $s$ on the pump power. These data are fitted with a polynomial function. We attribute such deviations to small changes of the locking point as the pump power increases, which induce changes in $\Delta_{pump}$ and hence of the parametric effect. In the Fig. 4.11b) phenomenological dependence of $s$ on $\Gamma_{eff}$ is included. The new theoretical lines for $R_-$ and $R_+$ show a better agreement at high pump powers.

The maximum measured asymmetry (at the maximum optical pump power 75 $\mu$W) is $1.20 \pm 0.01$ the corresponding occupation is $\sim$ 5 phonons. At this occupation, the attenuation in the squeezed quadrature $\sigma_Y^2$ is $\sim 0.72$ ($s = 0.39 \pm 0.01$). The variance is $\sim 8$ times higher then the variance at the ground state.

## Asymmetry vs pump detuning

We now study the dependence of the parametric gain as a function of the detuning of the pump beam. For this measurement, the total power injected in the cavity (pump 45 $\mu$W and probe 20 $\mu$W) and the intensity ratio between the two tones in the pump power are fixed. The parametric gain $s$ as a function of the pump detuning is shown in the Fig. 4.12a), and the sidebands asymmetry is shown in the Fig. 4.12b). The detuning values used in the figure take into account the cavity birefringence that is about 200 kHz. In Fig. 4.12a) the green symbols show the gain $s$ measured from the variance of two quadratures, through 4.58. The red symbols are the experimental values obtained from the widths of the broad and narrow linewidth of the heterodyne spectra, Eq. 4.59. The agreement between the two different measurement and the theoretical model (dashed black line) is very good. The variation of the detuning has the further effect of affecting the cooling efficiency. This is shown in Fig. 4.12b) where we plot the variation of the sideband asymmetry without parametric modulation (green points). The theoretical curve (green solid line) has a maximum close $\Delta_{pump} = 0$, where the cooling beam is red-detuned by a mechanical frequency, i.e. very close to the value where optimal cooling is expected. Accordingly, as the null pump detuning is approached ($\Delta_{pump} = 0$), the parametric gain is instead zero (see Eq. 4.21), and therefore the asymmetry of the blue ($R_+$) and red ($R_-$) Lorentzian curves converge to $R_0$ (see Fig. 4.12b)).

In this configuration, the detuning at which the maximum asymmetry occurs

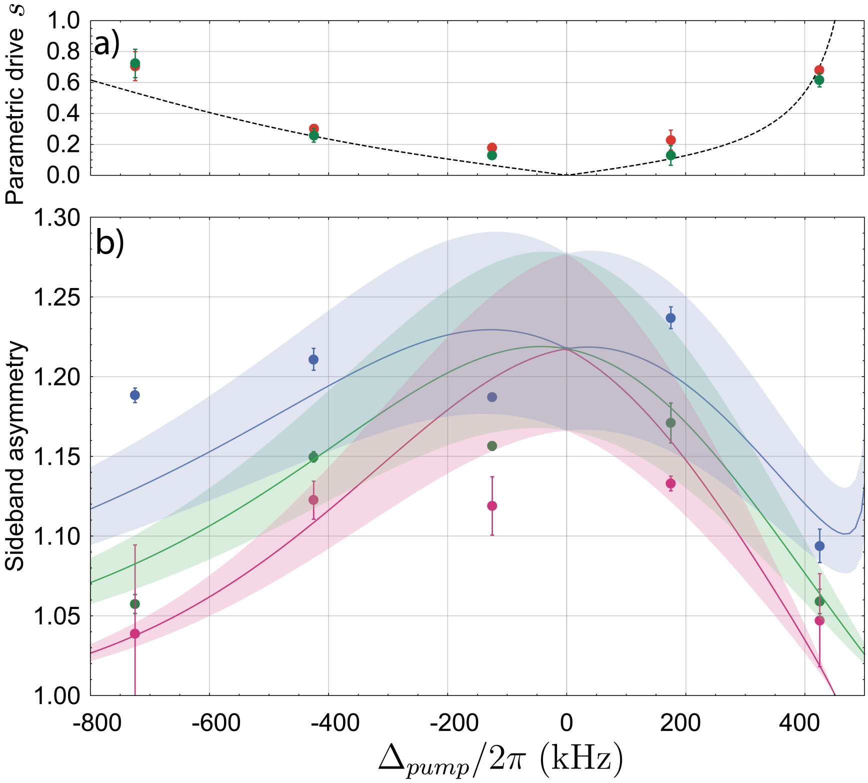

Figure 4.12: Panel (a): parametric gain $s$ as a function of the mean detuning of the pump tones: green symbols are measured from the variance of two quadratures, red symbols are the experimental values obtained from the widths of the broad and narrow linewidth. Panel (b): Green symbols: sideband asymmetry $R_0$ with no parametric drive (i.e., with detuned modulation tone), for increasing power in the modulation tone. Sideband ratios $R_+$, (blue circles) and $R_-$, (red circles) with coherent parametric drive. Dashed lines show the corresponding theoretical behavior, with shadowed areas given by the uncertainty in the system parameters. More details in the text.

is not the same at which the maximum squeezing gain. In the first case, the ratio between the two sidebands is $1.17 \pm 0.01$, the mechanical occupation is $\sim 6$ phonons, the parametric gain is $0.23 \pm 0.06$. The variance is $\sim 12\ x_{ZPF}^2$, with the parametric modulation on the variance is 10 times on the $ZPF$ variance. In the second case, $s = 0.71 \pm 0.09$, the asymmetry here is only $1.057 \pm 0.006$, the phonon occupation is $\sim 20$. The squeezed quadrature variance is $> 20\ x_{ZPF}^2$. In both cases the variance is well above the variance at the ground state.

## Fit considerations

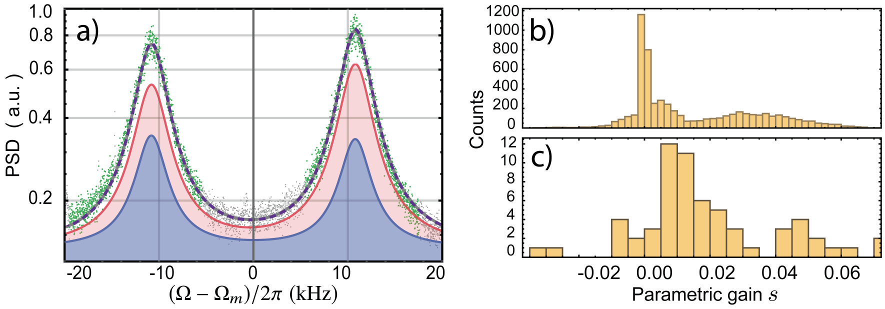

Figure 4.13: a) Heterodyne spectra (parametric modulation is out of resonance) around the $(0, 2)$ mechanical resonance at $\Omega_m/2\pi \approx 530$ showing the two motional sidebands separated by $\Delta_{LO}/2\pi = 11$ kHz. Gray symbols are used for data points excluded from the fitted regions. This spectrum is fitted with one couple of Lorentzian curves (gray solid line) with equal width $\Gamma_{eff}$ and different amplitudes (Eq. 4.60). For the same data we also show the fit obtained using two couples of Lorentzian curves (violet dashed line) according to the Eq. 4.61. The shaded (pink and light blue) regions show the two Lorentzian contributions. Panel b) shows the statistical distribution of s obtained with the same procedure on 6000 artificial, numerically generated spectra. Panel c) shows in this case the statistical distribution for the parametric gain $s$, on 60 independent measurements.

In this last section, we verify that the fitting procedure used on the heterodyne spectra, at modulation on, is not biased. We apply two couples of Lorentzian functions to a set of 60 independent spectra acquired in the absence of parametric drive, out of resonance, for different values of pump detuning, pump power and $\epsilon_c$. In Fig. 4.13a) is shown an example of the fitted Lorentzian components (shaded pink and blue regions). The fit procedure is the same as described before. The statistical distribution of $s$, shown in Fig. 4.13c), has a mean value of 0.038 with a standard deviation of 0.046, thus compatible with $s = 0$, as expected. The standard deviation on $s$ in the presence of parametric drive is similar. As a further check, we have generated 6000 artificial spectra with $s = 0$ and the same parameters and signal-to-noise ratio of the experiment and repeated the analysis. The statistical distribution of $s$ is shown in the Fig. 4.13b), from which we extract a mean value of 0.014 and a standard deviation of 0.019. That results are similar to the experimental ones. It can be noticed that both the experimental and the artificial distributions are slightly asymmetric, with comparable skewness, respectively 1.12 and 0.7. This structure could thus be related to the fitting procedure. Nevertheless our analysis seems to be reliable at the level of a few hundredths on $s$. In addition the $s$ values obtained from the heterodyne spectra, in the presence of parametric modulation as compared with to those obtained from the quadrature ones, are in good agreement within the statistical error. The physical evidence of the parametric gain in the quadrature gives a real good reason to use our model, using four Lorentzian, to fit the two sidebands at the modulation on. In conclusion that checks prove the validity of our fit procedure.

## Future perspectives

As we have seen, the sidebands spectra provide a powerful quantum indicator of a squeezed state: the narrow and broad Lorentzian components of each motional sideband give a signature of the imbalance between the fluctuations in the two quadratures, while the sidebands asymmetry quantifies their non-classical nature. Similarly to thermal states, even for the squeezed state the transition between classical and quantum behavior is smooth and some level of quantum squeezing is present even in macroscopic oscillators dominated by thermal noise. We remark indeed that the sideband asymmetry is in itself a fully quantum feature. On the other hand, it is interesting to examine the case in which the residual fluctuations in the squeezed quadrature are reduced below the zero-point level. It occurs when $(2\bar{n}+1)/(1+s) < 1$, i.e. for $s > 2\bar{n}$. In this case Eq. 4.45 the broad Lorentzian of the anti-Stokes sideband becomes negative, as although the overall spectral density remains

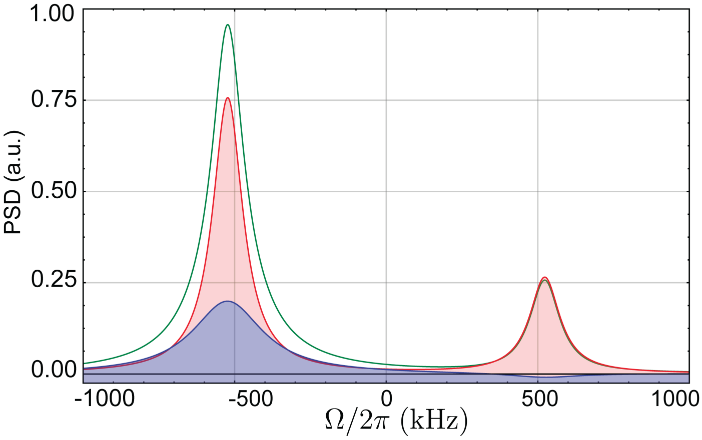

Figure 4.14: Green line: theoretical spectra of the anti-Stokes and Stokes sidebands from the Eq. 4.45 and 4.44. Calculated for $\bar{n} = 0.12$ and $s = 0.4$. The blue and red lines show respectively the broad and narrow Lorentzian components.

always positive due to the compensation of the narrow component, this is shown in Fig. 4.14. The negativity of the broad component provides a clear indication of a *bona fide* quantum squeezing without the necessity of absolute calibrations. In order to be observable in the stable regime of parametric modulation ($s < 1$), the condition $s > 2\bar{n}$ would require an initial occupation number $\bar{n} < 0.5$. This level has been reached even in optomechanical setups based on SiN membranes [31, 54].

# Conclusion and Remarks

In this thesis I show how it is possible to confine and control a macroscopic oscillator in a quantum state. I also show the manipulation of the oscillator quantum state, and in particular the generation of a squeezing state. These results are described in the last two chapters.

In Ch. 2, I have described in detail the used experimental apparatus. I have described our optomechanical system, including cavity and membrane, and I have shown the quality factor measurement realized for different mechanical modes at room and cryogenic temperature. In addition, I have described the laser frequency noise characterization and the filter cavity implemented in the apparatus.

In Ch. 3, I have compared two indicators of the oscillator occupation number, namely the peak area×width product of the spectrum acquired in a homodyne setup, and the motional sideband asymmetry, measured by heterodyne detection. Neither case requires additional calibrations, even if the actual oscillator base temperature can be an issue for the homodyne method. Both indicators are particularly sensitive at low occupation numbers (i.e., in the transition from classical to quantum regime). In optomechanical systems where the quantum back-action can be increase until it strongly dominates the thermal noise, the evaluation of $\bar{n}$ from homodyne spectra is facilitated by accessing the region where $\bar{n} \simeq n_{BA}^{cool}$ [65]. In the shown case the two kinds of estimate are in agreement, showing that a minimal occupation number of 3.9 is achieved in our experiment. However, the heterodyne indicator is superior because it is less sensitive to additional technical noise, and it gives a result with a single measurement while the former procedure requires a set of measurements as a function of, e.g., the cooling power. To reliably exploit the latter indicator one should keep in mind that a crucial requirement for an accurate measurement of the sidebands ratio is the control of the probe detuning. I have shown a method to perform it, based on the observation of the spectral features of weakly coupled mechanical modes. The calibration of the detuning is thus performed using phase signals generated inside the optomechanical cavity. This method is more trustworthy than exploiting frequency modulation of the probe field since a commonly occurring simultaneous phase and amplitude modulation, as well as spurious reflections along the path of the probe beam, generates asymmetric sidebands that spoils accurate measurements of the cavity detuning.

In Ch. 4, I have described a cavity optomechanics experiment where a macroscopic mechanical oscillator is parametrically driven by a suitable combination of optical fields [20]. We have shown that the generated mechanical squeezed state exhibits a quantum dynamics that is evidenced by the shape of the motional sidebands. In the Sec. 4.1, I have described the theoretical model behind this phenomenon and presented a detailed characterization of the experimental achievements, in good agreement with the model. I suggest that the analysis of the motional sidebands can provide a clear signature of the noise reduction below the zero-point fluctuations that occurs in one quadrature, without requiring any absolute calibration of the displacement spectra or even a direct measurement of the quadrature fluctuations. These results widen the range of macroscopic nonclassical states that can be explored in optomechanical experiments. For instance, interesting developments can involve nonstationary squeezed states and multimode squeezing [46, 53, 57].

A widespread use of reliable quantum optomechanical indicators, toward which this work is contributing, is expected to play in important role in the study of basic physics phenomena and in the development of quantum technologies [3].

# Appendix A

# Rotating Frame

Many times along the theoretical description we changed the reference system in a rotating one. This new description is useful to delete the free evolution from the expectation value of the used operators. In our work the common frequencies are $\Omega_m$ or $\omega_l$. Here, we report an example of this rotation around the laser frequency $\omega_l$. The creation and annihilation operators and the Hamiltonian operator are moved in the new system by using a unitary operator $\hat{U}(t)$, defined as:

$$\hat{U}(t) = e^{i\omega_l t \; \hat{a}^\dagger \hat{a}}. \tag{A.1}$$

It is possible demonstrate that the annihilation and creation operators in the new system are respectively:

$$\hat{a}_R(t) = \hat{a}(t) e^{i\omega_l t}, \tag{A.2}$$

$$\hat{a}_R^\dagger(t) = \hat{a}^\dagger(t) e^{-i\omega_l t}. \tag{A.3}$$

The new Hamiltonian in the rotating system is obtained following the evolution obtained by using a unitary transformation [6]:

$$\hat{H} \longrightarrow \hat{U}\hat{H}\hat{U}^\dagger - i\hbar\hat{U}\frac{\partial \hat{U}^\dagger}{\partial t}. \tag{A.4}$$

The optomechanical Hamiltonian is described in the Eq. 1.77, where in the rotating frame it become:

$$\hat{H} \longrightarrow \hat{H}_R - \hbar\omega_l \hat{a}_R^\dagger \hat{a}_R \tag{A.5}$$

where

$$\hat{H}_R = \hbar\omega_{cav}\hat{a}_R^{\dagger}\hat{a}_R + \hbar\Omega_m\hat{b}^{\dagger}\hat{b} - \hbar g_0\hat{a}_R^{\dagger}\hat{a}_R(\hat{b}^{\dagger} + \hat{b}). \tag{A.6}$$

From this equation we obtain the Eq. 1.79 the operator in the rotating frame are rewritten without the notation $R$ for simplicity. The rotating frame can be applied also at the Langevin equations, where the system rotates around the mechanical frequency $\Omega_m$.

# Appendix B

# Heavy modes area

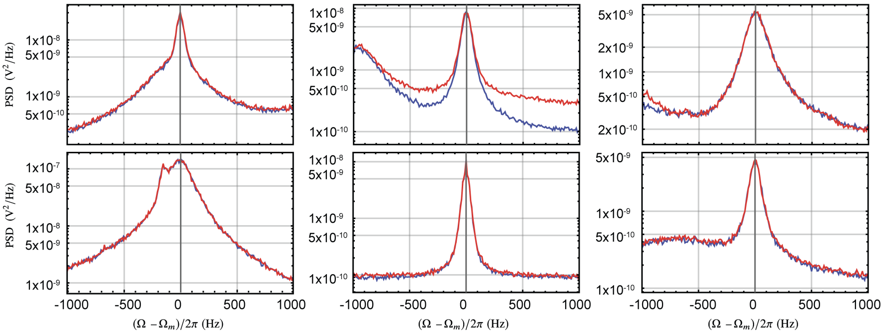

Figure B.1: In these six panels are displayed the two sidebands for six heavy "twin" mechanical modes used in our study. Starting from the upper left panel we have the modes: $(1,1)$, $(2,3)$, $(2,4)$, $(4,1)$, $(4,3)$, $(4,2)$.

In this short section we describe the method used to measure the area of the "heavy twin" mechanical mode with a high effective mass. These mechanical modes are studied to investigate the effective detuning of the probe beam, to correct the asymmetry due to the cavity cut-off, in Ch. 3. The membrane modes interested to this characterization are only those with very low coupling to the cavity field (due to the overlap between the modes and the cavity field). For this reason these mechanical modes are not affected by the optomechanical effects due to the detuned cooling beam. Indeed, the only sideband asymmetry is generated by the cavity cut-off. Some examples

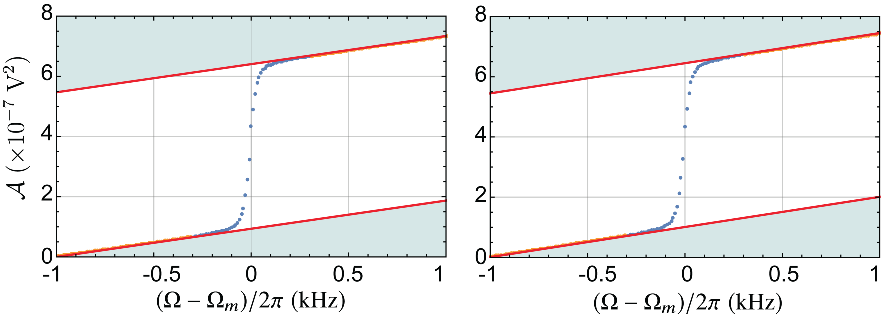

Figure B.2: Areas for the two sidebands, Stokes and anti-Stokes, for a "heavy twin" mode.

of heavy modes are shown in Fig. B.1, where the two bands, Stokes and anti-Stokes, are shown with red and blue colour. The areas are measured by using the follow procedure: first, we integrate the spectrum around the two sidebands ($\Omega_m \pm \Delta_{LO}$), furthermore we fit the initial and the last integrated sectors with a linear shape. The two linear fits are performed simultaneously, using for both a single slope and two distinct constant terms. The difference between two constant terms gives the area under the mechanical modes. With this technique we delete directly the contribution of the back-ground. An example of it can be observed in the Fig. B.2, where in the left and right panel is shown respectively the area of the anti-Stokes and Stokes bands. From the areas ratio we can measure the asymmetry between the two bands. These areas are used to characterize the detuning of the probe beam as is described in Ch. 3.

# Appendix C

# Heterodyne

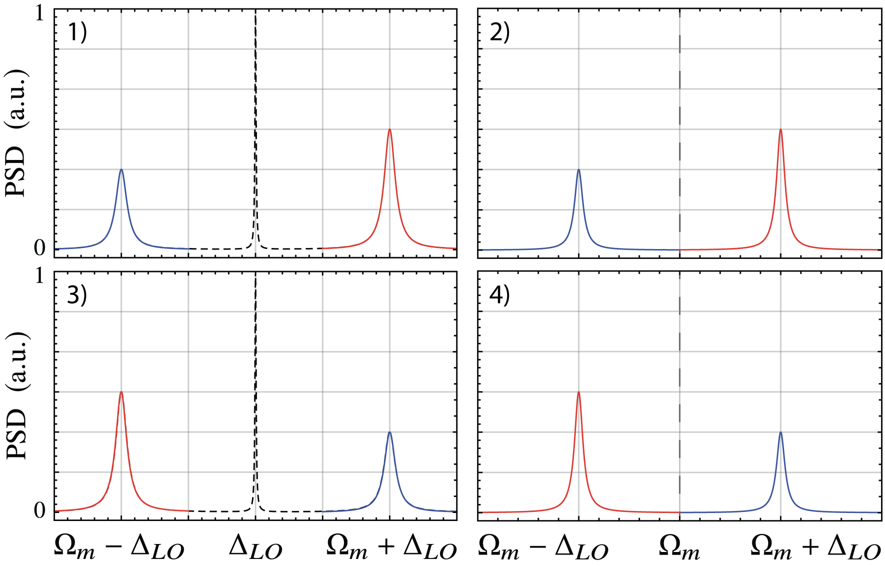

Figure C.1: Four different cases, following the previews enumerations. Blu Lorentzian: anti-Stokes vibrational bands. Red Lorentzian: Stokes vibrational bands.

In this section we will describe the heterodyne detection in a classical view. We can consider two electromagnetic fields. The first one is called local oscillator (LO), it is the reference beam at the frequency $\omega_{LO}$. The second beam is called signal, it is in resonance to the cavity at the frequency $\omega_{cav}$. The beams are overlapped on a beam splitter, then the interference beam is detected on a photodiode. The photocurrent is proportional to the intensity of the field that impinges on the detector. The fields are:

$$E_{LO} = E_{LO}^0 \, e^{i(\omega_{LO}t+\phi_{LO})} \tag{C.1}$$

$$E_S = E_S^0 \, e^{i(\omega_S t+\phi_p)} \tag{C.2}$$

where $E_S^0$ and $E_{LO}^0$ are the fields amplitudes, $\omega_S = \omega_{cav} \pm \Omega_m$ is the frequency of the signal beam, $\phi_{LO}$ and $\phi_S$ are the additional two phases of the respective electromagnetic fields. The frequency of the signal beam has the information about the Stokes ($-\Omega_m$) and the anti-Stokes ($\Omega_m$) bands. The intensity of the interference between the two beams is:

$$\begin{aligned} |E_{LO}+E_S|^2 = |E_{LO}|^2 + |E_S|^2 + \\ E_{LO}E_S\big(e^{i(\omega_S-\omega_{LO})t+i(\phi_S-\phi_{LO})} + e^{i(\omega_{LO}-\omega_S)t+i(\phi_{LO}-\phi_S)}\big). \end{aligned} \tag{C.3}$$

The interference term is the last one. All the information on the two vibrational bands are on it. The frequency shift between the to fields is defined as $\Delta_{LO} = \omega_{LO} - \omega_{cav}$, where we can consider a negligible phases shift during the measure $\phi_{LO} \approx \phi_S$. The total fields become:

$$|E_{LO}+E_S|^2 \propto e^{i(\pm\Omega_m-\Delta_{LO})t} + e^{i(\Delta_{LO}-(\pm\Omega_m))t} \tag{C.4}$$

we can identify four different cases:

1. $\Delta_{LO} > 0$ and $\Omega_m < \Delta_{LO}$:
   (a) anti-Stokes ($\Omega_m$): $\Omega_m - \Delta_{LO} < 0$ and $\Delta_{LO} - \Omega_m > 0$;
   (b) Stokes ($-\Omega_m$): $-\Omega_m - \Delta_{LO} < 0$ and $\Delta_{LO} + \Omega_m > 0$.
2. $\Delta_{LO} > 0$ and $\Omega_m \gg \Delta_{LO}$;
   (a) anti-Stokes ($\Omega_m$): $\Omega_m - \Delta_{LO} > 0$ and $\Delta_{LO} - \Omega_m < 0$;
   (b) Stokes ($-\Omega_m$): $-\Omega_m - \Delta_{LO} < 0$ and $\Delta_{LO} + \Omega_m > 0$.
3. $\Delta_{LO} < 0$ and $\Omega_m < \Delta_{LO}$:
   (a) anti-Stokes ($\Omega_m$): $\Omega_m - \Delta_{LO} > 0$ and $\Delta_{LO} - \Omega_m < 0$;

   (b) Stokes ($-\Omega_m$): $-\Omega_m - \Delta_{LO} > 0$ and $\Delta_{LO} + \Omega_m < 0$.

4. $\Delta_{LO} < 0$ and $\Omega_m \gg \Delta_{LO}$:
   (a) anti-Stokes ($\Omega_m$): $\Omega_m - \Delta_{LO} > 0$ and $\Delta_{LO} - \Omega_m < 0$;
   (b) Stokes ($-\Omega_m$): $-\Omega_m - \Delta_{LO} < 0$ and $\Delta_{LO} + \Omega_m > 0$.

In the spectra we can observe only the positive frequency, indeed only the positive terms are observable in the detection, as is shown in Fig. C.1.

In this work we use the heterodyne detection in the configuration two, where $\Delta_{LO} > 0$ and $\Omega_m \gg \Delta_{LO}$. The usual shift between the probe and the reference beam ($\Delta_{LO}$) is around $\sim$ 10 kHz and the mechanical frequency is higher than 300 kHz. In this configuration the Stokes sideband will be on the right side of the spectra and the anti-Stokes will be in the left side.

In the homodyne detection the shift in frequency between the two beams ($\Delta_{LO}$) is zero. In it we have a single Lorentzian for each mechanical resonance. It is an average between the two physics process, Stokes and Anti-stokes. In this configuration the probe beam is phase locked with the reference one. Indeed the only phase fluctuations are due to the interaction of the probe beam and the mechanical oscillator in the cavity.

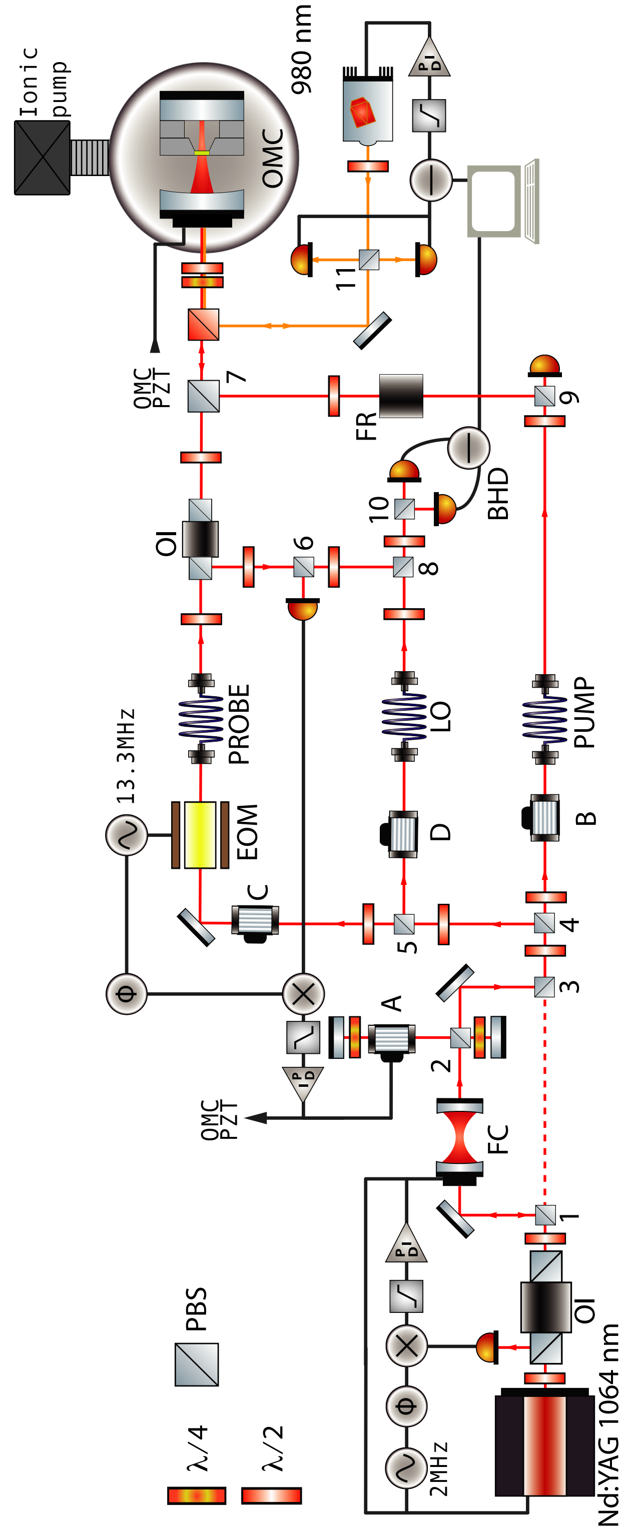
Ionic pump
980 nm
OMC
OMC PZT
7
11
FR
9
BHD
10
8
6
OI
PROBE
LO
PUMP
13.3MHz
EOM
C
D
B
5
4
3
A
2
FC
1
OI
OMC PZT
PID
PID
Φ
Φ
2MHz
Nd:YAG 1064 nm
PBS
λ/4
λ/2

# List of Figures

# Bibliography

[1] J Abadie, Benjamin P Abbott, R Abbott, Thomas D Abbott, M Abernathy, Carl Adams, R Adhikari, Christoph Affeldt, B Allen, GS Allen, et al. A gravitational wave observatory operating beyond the quantum shot-noise limit. *Nature Physics*, 7(12):962, 2011.

[2] Alex Abramovici and Jake Chapsky. *Feedback control systems: A fast-track guide for scientists and engineers.* Springer Science & Business Media, 2012.

[3] Antonio Acín, Immanuel Bloch, Harry Buhrman, Tommaso Calarco, Christopher Eichler, Jens Eisert, Daniel Esteve, Nicolas Gisin, Steffen J Glaser, Fedor Jelezko, Stefan Kuhr, Maciej Lewenstein, Max F Riedel, Piet O Schmidt, Rob Thew, Andreas Wallraff, Ian Walmsley, and Frank K Wilhelm. The quantum technologies roadmap: a european community view. *New Journal of Physics*, 20(8):080201, aug 2018.

[4] Olivier Arcizet, P-F Cohadon, Tristan Briant, Michel Pinard, and Antoine Heidmann. Radiation-pressure cooling and optomechanical instability of a micromirror. *Nature*, 444(7115):71–74, 2006.

[5] M. Aspelmeyer, T.J. Kippenberg, and F. Marquardt. *Cavity Optomechanics: Nano- and Micromechanical Resonators Interacting with Light.* Quantum Science and Technology. Springer Berlin Heidelberg, 2014.

[6] Markus Aspelmeyer, Tobias J. Kippenberg, and Florian Marquardt. Cavity optomechanics. *Rev. Mod. Phys.*, 86:1391–1452, Dec 2014.

[7] Minhang Bao, Heng Yang, Hao Yin, and Yuancheng Sun. Energy transfer model for squeeze-film air damping in low vacuum. *Journal of Micromechanics and Microengineering*, 12(3):341, 2002.

[8] Kjetil Børkje. Heterodyne photodetection measurements on cavity optomechanical systems: Interpretation of sideband asymmetry and limits to a classical explanation. *Physical Review A*, 94(4):043816, 2016.

[9] Max Born and Emil Wolf. *Principles of optics: electromagnetic theory of propagation, interference and diffraction of light.* Elsevier, 1965.

[10] A Borrielli, L Marconi, F Marin, F Marino, B Morana, G Pandraud, A Pontin, GA Prodi, PM Sarro, E Serra, et al. Control of recoil losses in nanomechanical sin membrane resonators. *Physical Review B*, 94(12):121403, 2016.

[11] A Borrielli, A Pontin, FS Cataliotti, L Marconi, F Marin, F Marino, G Pandraud, GA Prodi, E Serra, and M Bonaldi. Low-loss optomechanical oscillator for quantum-optics experiments. *Physical Review Applied*, 3(5):054009, 2015.

[12] S Bose, K Jacobs, and PL Knight. Preparation of nonclassical states in cavities with a moving mirror. *Physical Review A*, 56(5):4175, 1997.

[13] Warwick P Bowen and Gerard J Milburn. *Quantum optomechanics.* CRC press, 2015.

[14] VB Braginski and AB Manukin. Ponderomotive effects of electromagnetic radiation. *Sov. Phys. JETP*, 25(4):653–655, 1967.

[15] Daniel WC Brooks, Thierry Botter, Sydney Schreppler, Thomas P Purdy, Nathan Brahms, and Dan M Stamper-Kurn. Non-classical light generated by quantum-noise-driven cavity optomechanics. *Nature*, 488(7412):476–480, 2012.

[16] Herbert B Callen and Richard F Greene. On a theorem of irreversible thermodynamics. *Physical Review*, 86(5):702, 1952.

[17] Herbert B Callen and Theodore A Welton. Irreversibility and generalized noise. *Physical Review*, 83(1):34, 1951.

[18] S Chakram, YS Patil, L Chang, and M Vengalattore. Dissipation in ultrahigh quality factor sin membrane resonators. *Physical review letters*, 112(12):127201, 2014.

[19] Jasper Chan, TP Mayer Alegre, Amir H Safavi-Naeini, Jeff T Hill, Alex Krause, Simon Gröblacher, Markus Aspelmeyer, and Oskar Painter. Laser cooling of a nanomechanical oscillator into its quantum ground state. *Nature*, 478(7367):89–92, 2011.

[20] A Chowdhury, P Vezio, M Bonaldi, A Borrielli, F Marino, Bruno Morana, GA Prodi, PM Sarro, Enrico Serra, and F Marin. Quantum signature of a squeezed mechanical oscillator. *Physical Review Letters*, 124(2):023601, 2020.

[21] RG Christian. The theory of oscillating-vane vacuum gauges. *Vacuum*, 16(4):175–178, 1966.

[22] Jeremy B Clark, Florent Lecocq, Raymond W Simmonds, José Aumentado, and John D Teufel. Observation of strong radiation pressure forces from squeezed light on a mechanical oscillator. *Nature Physics*, 12(7):683–687, 2016.

[23] Aashish A Clerk, Michel H Devoret, Steven M Girvin, Florian Marquardt, and Robert J Schoelkopf. Introduction to quantum noise, measurement, and amplification. *Reviews of Modern Physics*, 82(2):1155, 2010.

[24] L.L. D and L.E. M. *Theory of Elasticity*. Course of theoretical physics. Pergamon Press, 1989.

[25] RWP Drever, John L Hall, FV Kowalski, J_ Hough, GM Ford, AJ Munley, and H Ward. Laser phase and frequency stabilization using an optical resonator. *Applied Physics B*, 31(2):97–105, 1983.

[26] Matt Eichenfield, Ryan Camacho, Jasper Chan, Kerry J Vahala, and Oskar Painter. A picogram-and nanometre-scale photonic-crystal optomechanical cavity. *nature*, 459(7246):550–555, 2009.

[27] Albert Einstein. Entwicklung unserer anschauungen über das wesen und die konstitution der strahlung. *Physikalische Zeitschrift 10*, 1909.

[28] J El Qars, M Daoud, and Ahl Laamara. Entanglement versus gaussian quantum discord in a double-cavity opto-mechanical system. *International Journal of Quantum Information*, 13(06):1550041, 2015.

[29] Claude Fabre, Michel Pinard, Sophie Bourzeix, Antoine Heidmann, Elisabeth Giacobino, and Serge Reynaud. Quantum-noise reduction using a cavity with a movable mirror. *Physical Review A*, 49(2):1337, 1994.

[30] George W Ford, John T Lewis, and RF O'connell. Quantum langevin equation. *Physical Review A*, 37(11):4419, 1988.

[31] I. Galinskiy, Y. Tsaturyan, M. Parniak, and E. S. Polzik. Phonon counting thermometry of an ultracoherent membrane resonator near its motional ground state. *Optica*, 7(6):718–725, Jun 2020.

[32] Khashayar Babaei Gavan, Joost Van Der Heijden, Emile WJM Van Der Drift, and Herre SJ Van Der Zant. Effect of pressure on the q factor and the resonance frequency of sin microcantilevers. In *2009 4th IEEE International Conference on Nano/Micro Engineered and Molecular Systems*, pages 380–384. IEEE, 2009.

[33] Schwab Gigan, HR Böhm, Mauro Paternostro, Florian Blaser, G Langer, JB Hertzberg, Keith C Schwab, Dieter Bäuerle, Markus Aspelmeyer, and Anton Zeilinger. Self-cooling of a micromirror by radiation pressure. *Nature*, 444(7115):67–70, 2006.

[34] Vittorio Giovannetti and David Vitali. Phase-noise measurement in a cavity with a movable mirror undergoing quantum brownian motion. *Physical Review A*, 63(2):023812, 2001.

[35] Stefan Goßler. *The suspension systems of the interferometric gravitational-wave detector GEO600*. PhD thesis, Universität Hannover Hannover, 2004.

[36] Andri M Gretarsson, Gregory M Harry, Steven D Penn, Peter R Saulson, William J Startin, Sheila Rowan, Gianpietro Cagnoli, and Jim Hough. Pendulum mode thermal noise in advanced interferometers: a comparison of fused silica fibers and ribbons in the presence of surface loss. *Physics Letters A*, 270(3-4):108–114, 2000.

[37] Simon Gröblacher, Klemens Hammerer, Michael R Vanner, and Markus Aspelmeyer. Observation of strong coupling between a micromechanical resonator and an optical cavity field. *Nature*, 460(7256):724–727, 2009.

[38] https://www.coherent.com/. *Coherent, Inc.*

[39] A M Jayich, J C Sankey, K Børkje, D Lee, C Yang, M Underwood, L Childress, A Petrenko, S M Girvin, and J G E Harris. Cryogenic optomechanics with a si3n4membrane and classical laser noise. *New Journal of Physics*, 14(11):115018, nov 2012.

[40] AM Jayich, JC Sankey, BM Zwickl, C Yang, JD Thompson, SM Girvin, AA Clerk, F Marquardt, and JGE Harris. Dispersive optomechanics: a membrane inside a cavity. *New Journal of Physics*, 10(9):095008, 2008.

[41] Farid Ya Khalili, Haixing Miao, Huan Yang, Amir H Safavi-Naeini, Oskar Painter, and Yanbei Chen. Quantum back-action in measurements of zero-point mechanical oscillations. *Physical Review A*, 86(3):033840, 2012.

[42] Herwig Kogelnik and Tingye Li. Laser beams and resonators. *Applied optics*, 5(10):1550–1567, 1966.

[43] Rep Kubo. The fluctuation-dissipation theorem. *Reports on progress in physics*, 29(1):255, 1966.

[44] AG Kuhn, J Teissier, L Neuhaus, S Zerkani, E Van Brackel, S Deléglise, T Briant, P-F Cohadon, A Heidmann, C Michel, et al. Free-space cavity optomechanics in a cryogenic environment. *Applied Physics Letters*, 104(4):044102, 2014.

[45] Xiao Liu, JF Vignola, HJ Simpson, BR Lemon, BH Houston, and DM Photiadis. A loss mechanism study of a very high q silicon micromechanical oscillator. *Journal of Applied Physics*, 97(2):023524, 2005.

[46] I. Mahboob, H. Okamoto, K. Onomitsu, and H. Yamaguchi. Two-mode thermal-noise squeezing in an electromechanical resonator. *Phys. Rev. Lett.*, 113:167203, Oct 2014.

[47] S Mancini, VI Man'ko, and P Tombesi. Ponderomotive control of quantum macroscopic coherence. *Physical Review A*, 55(4):3042, 1997.

[48] Stefano Mancini and Paolo Tombesi. Quantum noise reduction by radiation pressure. *Physical Review A*, 49(5):4055, 1994.

[49] Florian Marquardt, Joe P Chen, Aashish A Clerk, and SM Girvin. Quantum theory of cavity-assisted sideband cooling of mechanical motion. *Physical review letters*, 99(9):093902, 2007.

[50] Florian Marquardt, AA Clerk, and SM Girvin. Quantum theory of optomechanical cooling. *Journal of Modern Optics*, 55(19-20):3329–3338, 2008.

[51] Ernest Fox Nichols and Gordon Ferrie Hull. A preliminary communication on the pressure of heat and light radiation. *Physical Review (Series I)*, 13(5):307, 1901.

[52] TA Palomaki, JW Harlow, JD Teufel, RW Simmonds, and Konrad W Lehnert. Coherent state transfer between itinerant microwave fields and a mechanical oscillator. *Nature*, 495(7440):210–214, 2013.

[53] Y. S. Patil, S. Chakram, L. Chang, and M. Vengalattore. Thermomechanical two-mode squeezing in an ultrahigh-$q$ membrane resonator. *Phys. Rev. Lett.*, 115:017202, Jun 2015.

[54] R. W. Peterson, T. P. Purdy, N. S. Kampel, R. W. Andrews, P.-L. Yu, K. W. Lehnert, and C. A. Regal. Laser cooling of a micromechanical membrane to the quantum backaction limit. *Phys. Rev. Lett.*, 116:063601, Feb 2016.

[55] M Pinard, C Fabre, and A Heidmann. Quantum-nondemolition measurement of light by a piezoelectric crystal. *Physical Review A*, 51(3):2443, 1995.

[56] A. Pontin, C. Biancofiore, E. Serra, A. Borrielli, F. S. Cataliotti, F. Marino, G. A. Prodi, M. Bonaldi, F. Marin, and D. Vitali. Frequency-noise cancellation in optomechanical systems for ponderomotive squeezing. *Phys. Rev. A*, 89:033810, Mar 2014.

[57] A Pontin, Michele Bonaldi, A Borrielli, L Marconi, F Marino, G Pandraud, GA Prodi, PM Sarro, Enrico Serra, and F Marin. Dynamical two-mode squeezing of thermal fluctuations in a cavity optomechanical system. *Physical review letters*, 116(10):103601, 2016.

[58] A Pontin, JE Lang, A Chowdhury, P Vezio, F Marino, B Morana, E Serra, F Marin, and TS Monteiro. Imaging correlations in heterodyne spectra for quantum displacement sensing. *Physical review letters*, 120(2):020503, 2018.

[59] Robert V Pound. Electronic frequency stabilization of microwave oscillators. *Review of Scientific Instruments*, 17(11):490–505, 1946.

[60] T. P. Purdy, P.-L. Yu, N. S. Kampel, R. W. Peterson, K. Cicak, R. W. Simmonds, and C. A. Regal. Optomechanical raman-ratio thermometry. *Phys. Rev. A*, 92:031802, Sep 2015.

[61] Thomas P Purdy, P-L Yu, RW Peterson, NS Kampel, and CA Regal. Strong optomechanical squeezing of light. *Physical Review X*, 3(3):031012, 2013.

[62] Liu Qiu, Itay Shomroni, Marie A. Ioannou, Nicolas Piro, Daniel Malz, Andreas Nunnenkamp, and Tobias J. Kippenberg. Floquet dynamics in the quantum measurement of mechanical motion. *Phys. Rev. A*, 100:053852, Nov 2019.

[63] Liu Qiu, Itay Shomroni, Paul Seidler, and Tobias J Kippenberg. Laser cooling of a nanomechanical oscillator to the zero-point energy. *arXiv preprint arXiv:1903.10242*, 2019.

[64] P. Rabl, C. Genes, K. Hammerer, and M. Aspelmeyer. Phase-noise induced limitations on cooling and coherent evolution in optomechanical systems. *Phys. Rev. A*, 80:063819, Dec 2009.

[65] Massimiliano Rossi, David Mason, Junxin Chen, Yeghishe Tsaturyan, and Albert Schliesser. Measurement-based quantum control of mechanical motion. *Nature*, 563(7729):53–58, 2018.

[66] Amir H. Safavi-Naeini, Jasper Chan, Jeff T. Hill, Thiago P. Mayer Alegre, Alex Krause, and Oskar Painter. Observation of quantum motion of a nanomechanical resonator. *Phys. Rev. Lett.*, 108:033602, Jan 2012.

[67] Amir H Safavi-Naeini, Jasper Chan, Jeff T Hill, Thiago P Mayer Alegre, Alex Krause, and Oskar Painter. Observation of quantum motion of a nanomechanical resonator. *Physical Review Letters*, 108(3):033602, 2012.

[68] Amir H Safavi-Naeini, Jasper Chan, Jeff T Hill, Simon Gröblacher, Haixing Miao, Yanbei Chen, Markus Aspelmeyer, and Oskar Painter. Laser noise in cavity-optomechanical cooling and thermometry. *New Journal of Physics*, 15(3):035007, mar 2013.

[69] Amir H Safavi-Naeini, Simon Gröblacher, Jeff T Hill, Jasper Chan, Markus Aspelmeyer, and Oskar Painter. Squeezed light from a silicon micromechanical resonator. *Nature*, 500(7461):185–189, 2013.

[70] Peter R Saulson. *Fundamentals of interferometric gravitational wave detectors.* World Scientific, 1994.

[71] Albert Schliesser, Rémi Rivière, Georg Anetsberger, Olivier Arcizet, and Tobias J Kippenberg. Resolved-sideband cooling of a micromechanical oscillator. *Nature Physics*, 4(5):415–419, 2008.

[72] Enrico Serra, M Bawaj, Antonio Borrielli, G Di Giuseppe, S Forte, Nenad Kralj, N Malossi, L Marconi, F Marin, F Marino, et al. Microfabrication of large-area circular high-stress silicon nitride membranes for optomechanical applications. *AIP Advances*, 6(6):065004, 2016.

[73] V. Sudhir, D. J. Wilson, R. Schilling, H. Schütz, S. A. Fedorov, A. H. Ghadimi, A. Nunnenkamp, and T. J. Kippenberg. Appearance and disappearance of quantum correlations in measurement-based feedback control of a mechanical oscillator. *Phys. Rev. X*, 7:011001, Jan 2017.

[74] Orazio Svelto and David C Hanna. *Principles of lasers*, volume 1. Springer, 2010.

[75] John D Teufel, Tobias Donner, Dale Li, Jennifer W Harlow, MS Allman, Katarina Cicak, Adam J Sirois, Jed D Whittaker, Konrad W Lehnert, and Raymond W Simmonds. Sideband cooling of micromechanical motion to the quantum ground state. *Nature*, 475(7356):359–363, 2011.

[76] JD Thompson, BM Zwickl, AM Jayich, Florian Marquardt, SM Girvin, and JGE Harris. Strong dispersive coupling of a high-finesse cavity to a micromechanical membrane. *Nature*, 452(7183):72–75, 2008.

[77] M. Underwood, D. Mason, D. Lee, H. Xu, L. Jiang, A. B. Shkarin, K. Børkje, S. M. Girvin, and J. G. E. Harris. Measurement of the motional sidebands of a nanogram-scale oscillator in the quantum regime. *Phys. Rev. A*, 92:061801, Dec 2015.

[78] Henning Vahlbruch. *Squeezed light for gravitational wave astronomy.* PhD thesis, Gottfried Wilhelm Leibniz Universität Hannover Hannover, Germany, 2008.

[79] D.F. Walls and G.J. Milburn. *Quantum Optics.* Springer Berlin Heidelberg, 2008.

[80] AJ Weinstein, CU Lei, EE Wollman, J Suh, A Metelmann, AA Clerk, and KC Schwab. Observation and interpretation of motional sideband asymmetry in a quantum electromechanical device. *Physical Review X*, 4(4):041003, 2014.

[81] DJ Wineland, Wayne M Itano, JC Bergquist, and Randall G Hulet. Laser-cooling limits and single-ion spectroscopy. *Physical Review A*, 36(5):2220, 1987.

[82] Emma Edwina Wollman, CU Lei, AJ Weinstein, J Suh, A Kronwald, F Marquardt, Aashish A Clerk, and KC Schwab. Quantum squeezing of motion in a mechanical resonator. *Science*, 349(6251):952–955, 2015.

[83] Jean Pierre Zendri, M Bignotto, Michele Bonaldi, M Cerdonio, L Conti, Lorenza Ferrario, N Liguori, A Maraner, Enrico Serra, and L Taffarello. Loss budget of a setup for measuring mechanical dissipations of silicon wafers between 300 and 4 k. *Review of Scientific Instruments*, 79(3):033901, 2008.

[84] Clarence Zener. Internal friction in solids ii. general theory of thermoelastic internal friction. *Physical review*, 53(1):90, 1938.